University of Groningen

Charge transport modelling of perovskite solar cells and organic thermoelectrics

Koopmans, Marten

DOI:
10.33612/diss.258880974

IMPORTANT NOTE: You are advised to consult the publisher's version (publisher's PDF) if you wish to cite from it. Please check the document version below.

Document Version
Publisher's PDF, also known as Version of record

Publication date:
2022

Link to publication in University of Groningen/UMCG research database

Citation for published version (APA):
Koopmans, M. (2022). *Charge transport modelling of perovskite solar cells and organic thermoelectrics*. [Thesis fully internal (DIV), University of Groningen]. University of Groningen. https://doi.org/10.33612/diss.258880974

Copyright
Other than for strictly personal use, it is not permitted to download or to forward/distribute the text or part of it without the consent of the author(s) and/or copyright holder(s), unless the work is under an open content license (like Creative Commons).

The publication may also be distributed here under the terms of Article 25fa of the Dutch Copyright Act, indicated by the “Taverne” license. More information can be found on the University of Groningen website: https://www.rug.nl/library/open-access/self-archiving-pure/taverne-amendment.

Take-down policy
If you believe that this document breaches copyright please contact us providing details, and we will remove access to the work immediately and investigate your claim.

Downloaded from the University of Groningen/UMCG research database (Pure): http://www.rug.nl/research/portal. For technical reasons the number of authors shown on this cover page is limited to 10 maximum.

Download date: 14-02-2023

Charge Transport Modelling for Perovskite Solar Cells and Organic Thermoelectrics

Marten Koopmans

Marten Koopmans
PhD thesis
Rijksuniversiteit Groningen

Zernike institute PhD thesis series 2022-23
ISSN 1570-1530

This thesis is part of the research program of the Foundation for Fundamental Research on Matter (FOM), which is part of the Netherlands Organization for Scientific Research (NWO). This is a publication by the FOM Focus Group "Next Generation Organic Photovoltaics," participating in the Dutch Institute for Fundamental Energy Research (DIFFER). I would like to thank the Center for Information Technology of the University of Groningen for their support and for providing access to the Peregrine high performance computing cluster.

Cover design: interaction of dopants and electrons on a simulation grid used in kinetic Monte Carlo simulations (front) and Shockley-Read-Hall recombination (back), designed by Marten Koopmans.

Printed by: Gildeprint

university of
groningen

Charge Transport Modelling of Perovskite Solar Cells and Organic Thermoelectrics

PhD thesis

to obtain the degree of PhD at the
University of Groningen
on the authority of the
Rector Magnificus Prof. C. Wijmenga
and in accordance with
the decision by the College of Deans.

This thesis will be defended in public on

Tuesday 20 December 2022 at 12:45 hours

by

Marten Koopmans
born on 28 September 1992
in Groningen

Supervisors
Prof. L.J.A. Koster
Prof. J.C. Hummelen

Assessment committee
Prof. R.A.J. Janssen
Prof. H. Sirringhaus
Prof. B. Ehrler

Contents

CHAPTER 1

Introduction

Rarely is a material discovered with properties so interesting, that an entire field of research forms around it. However, in 1977, Shirakawa et al. measured a conductivity increase of seven orders of magnitude by doping polyacetylene with halide vapour.[1] This meant that suddenly plastics could be considered for making semiconductor devices, such as light-emitting diodes (LEDs) and solar cells. For this discovery, they were awarded the Nobel Prize for chemistry in the year 2000.

Since then, a whole zoo of organic semiconductors has been synthesized, ranging from small molecules to polymers.[2] These materials have been used to create an impressive range of devices, such as solar cells,[3] light-emitting diodes,[4] thermoelectric generators,[5] and field-effect transistors.[6] These devices have performed very well in both research and commercial settings. The certified record for single junction organic solar cells sits at 18.2 % power conversion efficiency.[7] Also, The organic-LED market was 38 billion dollars in 2021 and is projected to grow to 73 billion in 2026.[8]

Charge transport in these organic materials was found to behave differently from inorganic materials. New models were needed to correctly describe the physics of charge transport in these devices. One of the most successful models, the Gaussian disorder model (GDM) was introduced by Bässler in 1984, which will be discussed in section 1.2.2.[9] Because of limited computing power at the time, research was restricted to analytical solutions, or numerical solutions in the low density regime.[10–12] Computers have grown exponentially in power since then, however, allowing us to venture into the high carrier density regime in chapter 4 and 5.

A material class that led to similar disruption of research fields is that of metal halide perovskites. Perovskite is a crystal structure for which the general formula ABX_3 is used, where A and B are cations and X are anions.[13] Many elemental compositions are possible, but in general perovskite materials yield very favourable physical properties, such as high absorption coefficient,[14] low exciton binding energy,[15,16] and high dielectric constant.[17,18] The real breakthrough for these materials came when they were first used as a light-absorbing material in a solar cell in 2009.[19]

Also perovskites have seen use in a wide variety of devices since then, like solar cells,[19] field effect transistors,[20] light-emitting diodes,[21] and gas sensors.[22] In this thesis, we will discuss perovskite solar cells in more detail. Their most likely application seems to be in a tandem configuration with silicon solar cells. If stability issues can be overcome, single junction perovskite solar cells could even outperform silicon cells with similar lab-tested power conversion efficiency in hot and humid climates.[23]

Complete solar cell stacks are often simulated through drift-diffusion simulations. These simulations use the basic semiconductor equations to calculate charged particle densities and currents, and the resulting electrostatic potential. The flexibility of these equations allows for the incorporation of effects typical for perovskite solar cells stacks, such as mobile ions and interfacial recombination. This results in accurate electrical modelling of perovskite solar cells, which is the focus of chapters 2 and 3.

The rest of this chapter is divided in a few distinct sections. First, in section 1.1, I will introduce basic concepts used in this thesis to describe the physics of solar cells and thermoelectrics. Then, in section 1.2 the used physical model for doped organic semiconductors and the numerical method used to obtain results are introduced. Similarly, in section 1.3 the physical model and simulation method for perovskite solar cells are elaborated upon. Finally, in section 1.4, I will outline the rest of this thesis.

1.1 The Physics of Semiconductors

Before we dive into the physics of semiconductor devices, we need to establish what defines a semiconductor. In individual atoms of any species, electrons are organized in atomic orbitals. When two atoms are brought together, these

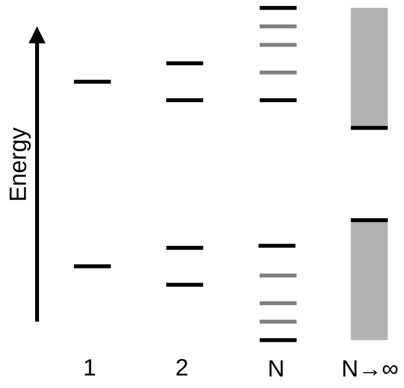

Figure 1.1: The energy levels of orbitals versus number of atoms. For 1 atom, these are the atomic orbitals. When adding atoms, energy levels are added, at different energies because of interaction between the atomic orbitals. When the number of levels is sufficiently large, the levels together effectively form a band.

orbitals split in two, with one lower than the initial energy and one higher than the initial energy. As more atoms are added to the cluster, the orbitals split into more and more levels, effectively forming a band for large clusters, like a piece of semiconductor material.

The positioning of the outermost (partially) filled band—the *valence band*—with respect to the first unfilled band—the *conduction band*—determines the most important conductivity characteristics of a material. When these bands overlap or the valence band is partially filled, the material is a metal and conduction is good. If these bands are separated by an intermediate bandgap (E_g) of up to 2-3 eV, the material is considered a semiconductor and conduction is intermediate, but is very sensitive to for example temperature. If E_g between these bands is larger, the material is an insulator and intrinsic conductivity is poor.[24]

While one aspect of conductivity is the presence of charge carriers to conduct, these carriers should be mobile to contribute to conductivity. To describe the mobility of charge carriers, one should look at the energetic landscape of the semiconductor. The crystal structure of a semiconductor can be considered an infinite periodic lattice. Because the lattice is periodic, the electron distribution must also be periodic, leading to a special kind of wavefunction called a Bloch wavefunction. This wavefunction is periodic and delocalized through the lattice, meaning electrons are not fixed to one specific atom.[25]

To get to the textbook semiconductor band picture, we need to apply two approximations. First, we neglect the spatial variation in the wavefunction, leaving us with the plane wave part of the Bloch wavefunction. This is called the *effective mass approximation*. For conduction, the top of the valence band and bottom of the conduction band are of primary importance. This is because most charge carriers that have unoccupied states to move into at similar energy levels reside here. Since we are only interested in the top of the valence band and the bottom of the conduction band, we can use an expansion of the wavefunction to locally approximate it at this position. This is often done using the second order of a power expansion, resulting in the *parabolic band approximation*, where the density of states is locally approximated as a parabola.[25]

1.1.1 Organic Semiconductors

Just like in the classical inorganic semiconductor case discussed before, atoms brought together in organic molecules split their energy levels when brought together. Differently from the classical case, however, atoms form molecules in organic semiconductors, not crystal latices. This means that the splitting of energy levels stops at the scale of molecules, and no bands will form.[1]

In organic semiconductors, double bonds of carbon atoms allow the formation of molecular π-orbitals over which electrons can delocalize within the molecule. These neighbouring π-orbitals can allow electrons to delocalize over many carbon atoms, such is the case in polyacetylene, for which the Nobel Prize was awarded.[1] Charge transport is often well characterized without including delocalization over large regions in space, however.[9] Because the clusters atoms that form molecules are smaller, and not crystalline, bands such as the valence and conduction band do not form in molecules. Instead, discrete molecular orbitals form. Similar to the case for the CB and VB, the *lowest unoccupied molecular orbital* (LUMO) and the *highest occupied molecular orbital* (HOMO) are most relevant for the molecules' conductive properties.

The gap between the LUMO and HOMO is generally small enough that it can be optically excited, making these materials semiconductors.[2] Since molecules

---

[1] This is not strictly speaking always true. Counter examples are: organic crystals, which do show band transport; and energy levels shared between multiple molecules in the formation of charge transfer complexes, discussed in section 1.1.4. For material systems where states are extended over large regions, hopping transport is likely not a good description of charge transport. Therefore, in this thesis this will be neglected.

[2] The gap between the HOMO and LUMO level is often also called a bandgap, even though

are typically not arranged in a crystal, but disordered, the local environment is different for every molecule. This results in a distribution of LUMO's and HOMO's that is well described by a Gaussian.[27] It should be emphasized, however, that this is a Gaussian distribution of localized states, instead of the parabolic distribution of delocalized states for the classical case.

When delocalization of charge carriers is restricted to molecules or molecular segments we will call sites, the way charge carriers move between these sites, is the bottleneck in charge transport. The most popular model to describe charge transport in these kinds of systems, is that of phonon assisted hopping. This is a tunnelling process, where the hopping rate depends, amongst other things, on the distance and energy difference between the initial and final site.[10,28] For the hopping rates, different expressions exist,[28,29] but in this thesis we will use Miller-Abrahams rates.[28] These rates have been shown to describe the physics reasonably accurately using quantum chemical calculations and have the added benefit of having few parameters.[30]

1.1.2 State Occupation in Thermal Equilibrium

Having discussed the energetic structure of semiconductors, we can explore what makes them so relevant for technology; their tunable mobile charge carrier density. There are different ways to affect the mobile carrier density like doping, temperature modulation, or interaction with light. First, we will focus on the effect of temperature on mobile carrier density.

At a temperature of zero Kelvin in the dark, a semiconductor will have a filled valence band and empty conduction band. More specifically, all states up to the Fermi energy E_F are filled, and all states above E_F are empty. At non-zero temperatures, electrons can be thermally excited from below E_F to above E_F. Under thermal equilibrium, the filled fraction of states can be described using Fermi-Dirac (FD) statistics. This means that the fraction of states filled f at a certain energy E is determined by the temperature T and E_F as

$$f(E, E_F, T) = \frac{1}{\exp\left(\frac{E-E_F}{k_B T}\right) + 1}, \tag{1.1}$$

where k_B is the Boltzmann constant. This function is shown for different temperatures in figure 1.2a When $E - E_F/k_B T \gg 1$, or far away from E_F, can be approximated by a Boltzmann factor, which is called the *Boltzmann approximation*.[24,25]

---

bands are often not present.[26] This gap does fulfil a similar role as the band gap in classical semiconductors, however.

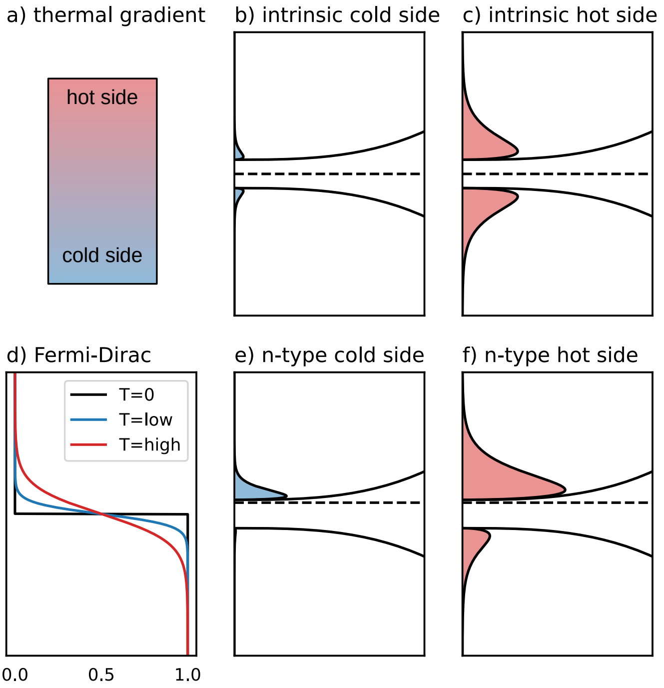

Figure 1.2: a) A piece of semiconductor with a thermal gradient between a hot and cold side. For intrinsic materials, the Fermi-level (dashed line) sits in the middle of the bandgap, resulting in symmetrical electron and hole occupation at both b) the cold side and c) the hot side. d) The used FD-function is shown for zero temperature, the cold and the hot side. For an n-doped semiconductor, both e) the cold side and f) the hot side are nonsymmetric in the Fermi-level. The shaded area in subfigures b, c, e, and f represent the integral of the product between the FD-function and the DOS, which equals the electron (CB) and hole (VB) densities.

The occupation of states under thermal equilibrium conditions in a semiconductor can now be determined by the product of the Fermi-Dirac function and the previously discussed density of states. This means that at a non-zero temperature, electrons will be thermally excited from valence to conduction band, resulting in mobile charge carriers that contribute to conductivity. For parabolic bands, this leads to electron and hole densities

$$n = N_C \exp\left(\frac{E_F - E_C}{k_B T}\right) \tag{1.2}$$

$$p = N_V \exp\left(\frac{E_V - E_F}{k_B T}\right), \tag{1.3}$$

where $N_{C/V}$ are the conduction band and valence band effective density of states, and $E_{C/V}$ are the conduction band and valence band energies. In intrinsic semiconductors, the Fermi level sits close to the middle between the conduction and valence band. From equations 1.2 and 1.3 it is clear that this positioning of E_F—far away from both bands—leads to relatively low electron and hole densities.[24]

1.1.3 Generation and Recombination

Under operating conditions, semiconductor devices such as solar cells are often not in thermal equilibrium. When the active layer in a solar cell absorbs light, for example, the absorbed photons excite electrons from the valence to the conduction band. This creates excess electrons in the conduction band and excess holes in the valence band. These can be exploited to do work as is done in solar cells. There are multiple recombination processes however that allow electrons and holes to recombine, mostly losing their potential energy in the process.

Direct recombination means that an electron falls back directly from the conduction band to the valence band. This is accompanied by the emission of a photon and is effectively the inverse of the light absorption process, as indicated in Fig 1.3b. This can be considered good, in a light-emitting diode for example, where light output is desired. In a solar cell, however, this is a loss mechanism as it reduces the electron and hole densities.[3] The direct recombination rate is

$$R_d = \gamma(np - n_i^2), \tag{1.4}$$

where γ is the direct recombination constant, n and p are the electron and hole densities and n_i is the intrinsic density of electrons and holes.[31] For perovskite

---

[3] The photons generated this way can be reabsorbed by the active layer in the solar cell, so they are only lost if the photon exits the solar cell before getting reabsorbed.

solar cells, which are discussed in this thesis, direct recombination is typically very low.[32]

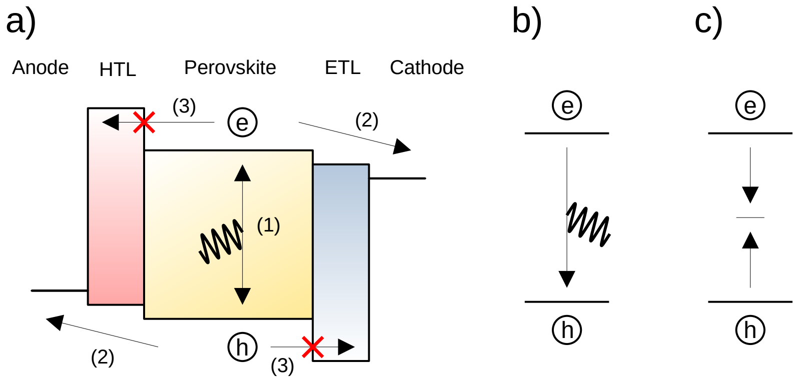

Figure 1.3: a) Schematic representation of a perovskite solar cell. (1) First, electron-hole pairs are generated through the absorption of photons. Charges can get extracted and contribute to useful current (2) or recombine radiatively b) or non-radiatively c). The electron transport layer (ETL) and hole transport layer (HTL) block opposite sign charge carriers from entering (3). b) Direct recombination through emission of a photon. c) Trap-assisted or Shockley-Read-Hall recombination.

In perovskite solar cells, trap-assisted recombination, or Shockley-Read-Hall (SRH) recombination is often the performance limiting recombination process and its rate is described by

$$R_{\mathrm{SRH}} = \frac{C_n C_p N_t}{C_n(n+n_1) + C_p(p+p_1)}(np - n_i^2). \tag{1.5}$$

Here $C_{n/p}$ are the electron and hole capture coefficients, N_t is the number of traps, and n_1/p_1 are the thermally excited electron and hole densities if the Fermi level would be at the trap energy.[33] SRH recombination is a two-step process in which a state within the bandgap takes part, as indicated in figure 1.3c. An electron from the conduction band falls back to the trap state, then the electron can either excite back to the conduction band, or fall back to the valence band. If it falls back to the valence band, the electron and hole have recombined non-radiatively and the excitation energy is lost.

In perovskite solar cells, SRH recombination takes place mainly at the perovskite/TL interface.[34–38] Therefore, the electron and hole density at either side of the interface should ideally enter into the expression, as there are large discontinuities at the interface. This extension to the SRH framework will be elaborated on in chapter 2. Other recombination processes, such as surface recombination at the electrode interface or Auger recombination, are out of scope for this thesis, as they are of small importance in perovskite solar cells.[39,40]

1.1.4 Doping

To increase charge carrier density, which is often required for applications, *doping* is used. Doping is a process by which E_F can be manipulated by inserting states between the valence and conduction bands. These states can be thermally excited to yield additional electrons in the valence band or holes in the conduction band. The way this is physically accomplished differs between the inorganic semiconductors we will discuss here and the organic semiconductors we will elaborate on afterwards.

In inorganic semiconductors, doping is achieved though the addition of heteroatoms, atoms which have either one more (donors) or one fewer (acceptors) valence electrons than the host semiconductor. As for silicon, phosphorous can be used as a donor for example, as it has one extra valence electron. This electron is loosely bound in silicon doped with phosphorous, meaning thermal activation is sufficient to excite the vast majority of these electrons to the conduction band. This results in roughly one electron per donor atom at ambient temperatures for inorganic semiconductors.[24]

For organic semiconductors, there are different mechanisms that can lead to doping. Most molecular systems transfer electrons from a dopant to a host without a chemical reaction.[41] This can occur via the formation of either ion-pairs, or charge-transfer complexes. In *ion-pair formation*, electron transfer takes place directly from the host to the dopant (p-type doping) or from the dopant to the host (n-type doping). For this to be viable, the LUMO of the dopant should be lower than or equal to the HOMO of the host for p-type doping. For n-type doping the opposite process occurs, so the host's LUMO should be lower in energy than the HOMO of the dopant.[41–44]

Another established mechanism through which doping can take place is the formation of *charge-transfer complexes* (CTCs). In this mechanism, the frontier molecular orbitals of the host and dopant hybridize to form a HOMO_{CTC} and LUMO_{CTC}. This allows relaxation of the criteria for the HOMO and LUMO levels of the host and dopant that govern ion-pair creation. The activation energy of these charge transfer complexes is typically relatively high, however, so not all CTCs yield free carriers. This, together with miscibility problems, causes the number of free charge carriers to often be different from the number of dopant molecules. Therefore, the carrier density has to be experimentally determined.[41–44]

1.2 Thermoelectrics

One of the applications of doped organic semiconductors is thermoelectric devices, which are used to harvest electrical energy from waste heat. Their working can be qualitatively understood from thermodynamics. Thermodynamics teaches us that gradients in intensive properties drive currents of their related energy carriers. A gradient in electrical potential drives a charge current, a gradient in pressure drives a change of volume, and a gradient in temperature drives an entropy current.[45]

In thermoelectrics, it is important to note that the carrier of both charge and entropy is physically the same thing, namely the electron. This means that if a temperature gradient drives a current of entropy carriers, these carriers also carry charge. There is therefore also an electric current that can result in a potential difference. This effect can work either way; an electric potential difference leading to a temperature difference is called the *Peltier effect*, while a temperature difference leading to a difference in electric potential is called the *Seebeck effect*.[46] In this thesis, we will limit ourselves to the Seebeck effect, as this is relevant for energy harvesting.

For a more detailed description of the Seebeck coefficient, we should realize what a change of temperature means physically. As discussed before, state occupation under thermal equilibrium follows the Fermi-Dirac distribution from equation 1.1. This distribution widens for increasing T and narrows for decreasing T as can be seen in figure 1.2a. The result is that at high temperature, there are relatively more high-energy states occupied and fewer low-energy sites occupied, as is shown in figure 1.2c. Diffusion of high-energy carriers to the cold side and diffusion of low-energy carriers to the hot side follows. Both of the processes increase entropy, but they work against each other in terms of charge transport.

1.2.1 Thermoelectric Generator

To use the Seebeck effect for power generation, a thermoelectric generator is used. In a thermoelectric generator, as depicted in figure 1.4 a hot and cold side

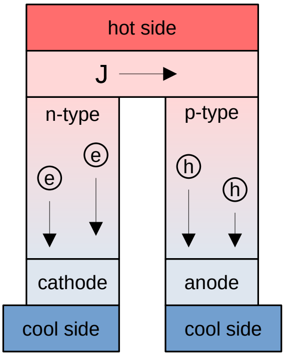

Figure 1.4: Schematic representation of a thermoelectric generator. Heat is supplied at the hot side, making electrons move to the cathode in the n-type leg and holes to the anode in the p-type leg. The cool side is kept at a lower temperature to maintain the temperature gradient.

are connected by two semiconducting legs, one n-type and one p-type. In the n-type leg, the Fermi-level sits closer to the conduction band or LUMO level. Therefore, the diffusion of high-energy carriers from the hot to the cold side is stronger than the reverse diffusion of low-energy carriers. In the p-type leg, diffusion of low-energy carriers from the cold to the hot side dominates, as a wider Fermi-Dirac distribution on the hot side leaves more low-energy states empty.

The efficiency of a thermoelectric generator can be described using[47]

$$\eta = \frac{\Delta T}{T_h} \frac{\sqrt{1+ZT}-1}{\sqrt{1+ZT}+T_c/T_h}, \tag{1.6}$$

where $T_{c/h}$ is the temperature on the hot and the cold side respectively, and ZT is the thermoelectric figure of merit. Since the temperatures are often given by the application, only part of equation 1.6 can be optimized by material engineering. Equation 1.6 shows that a larger ZT leads to a higher efficiency.[47] The figure of merit can be expanded to

$$ZT = \frac{S^2 \sigma T}{\kappa}, \tag{1.7}$$

where σ is the electrical conductivity, and κ is the thermal conductivity.[47] A value for ZT of around 1 is often seen as the lower limit for technological viability.[48] In organic semiconductors, κ is often so low that it is not considered for optimization,[49] leaving S and σ for optimization.

The electrical conductivity is given by

$$\sigma = qn\mu, \tag{1.8}$$

where q is the unit charge and μ is the carrier mobility. Since μ typically increases with increasing n in organic semiconductors, doping is an often used method to increase σ as it increases both μ and n.[12,50–54] The optimization of S is less obvious. S is defined through the Peltier coefficient (Π) via the Thomson relations as[55]

$$S = \frac{\Pi}{T}. \tag{1.9}$$

Here,

$$\Pi = -\frac{1}{e}\int (E - E_F)\frac{\sigma(E)}{\sigma}dE, \tag{1.10}$$

which equals the heat per unit charge carried by a charge current.[55] It can be seen that indeed all that contributes is conduction that does not occur at the Fermi energy. The Peltier coefficient Π also captures the balance between low-energy and high-energy carriers. If these opposite contributions cancel, the Peltier coefficient will be zero. The expression for Π is almost general, as any energy transported enters into the Peltier coefficient, however, here we chose to neglect non-electrical contributions to heat transport.

The expression for S defined previously is very useful in semiconductor simulations as it is widely applicable and the energy and conductivity function are known. Also, it makes it possible to calculate S without introducing temperature gradients that would break cyclic boundary conditions, making simulations much less demanding.[56,57] Experimentally, the conductivity function is inaccessible, however, but S also determines the ratio of the potential difference between a hot and cold side of a material the applied temperature difference is small as

$$S = -\frac{\Delta\phi}{\Delta T}. \tag{1.11}$$

By measuring the potential difference between upon application of a temperature gradient, this relation can be used to experimentally determine the Seebeck coefficient.[58–61]

1.2.2 Physical Modelling of Doped Organic Semiconductors

In this thesis, physical simulations of doped organic semiconductors are performed to investigate charge transport and thermoelectric properties. In this section, the physical model and its assumptions will be highlighted. In doped organic semiconductors, there are three components that are included in the description: the host material, the ionized dopants, and the mobile electrons.

First, one should realize that because of doping, the Fermi level shifts towards the LUMO (n-type) or HOMO (p-type). This results in charge transport that is dominated by the band to which the Fermi level is close. For this reason, it is sufficient to simulate either the LUMO (n-type) or HOMO (p-type). Because of delocalization of charge arcos a molecule or molecular segment, charge hopping from site to site, limits transport. Charge transport can therefore be approximated as charges hopping from one point-like site to point-like site.[10] A cubic grid of sites is used in practice, as this is numerically advantageous and has been shown to be sufficiently accurate.[10,50] As these sites represent LUMO or HOMO levels of the host material, they should be disordered. This is done by assigning every site an energy drawn randomly from a Gaussian distribution where the with is the degree of disorder σ, which is accessible experimentally.[27]

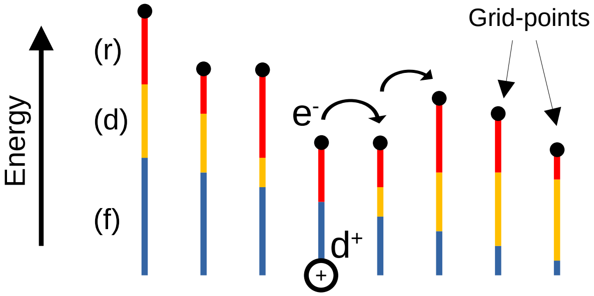

Figure 1.5: 1-dimensional representation of the energetic landscape of hopping sites in an organic semiconductor. Contributions to hopping site potential energy from random Gaussian disorder (r), dopant Coulomb potentials (d), and the electric field (f) are indicated. The grid points represent hopping sites.

Ionized dopants can be added by adding their Coulomb potential to the site energies, where these potentials will overlap significantly at higher dopant loading. To investigate transport properties, such as charge mobility, an electric field should be applied. The resulting electrostatic potential too can be added to the site energies, resulting in a static energetic landscape formed by intrinsic disorder of the organic molecules, the electric field, and Coulomb potentials of the dopants.

Mobile charge carriers can then be added in equal number to the ionized dopants, as would be the case in a doped organic semiconductor. Transport properties, such as conductivity, mobility, and the Seebeck coefficient can be extracted by simulating hopping of charge carriers from site to site as we will discuss next.

1.2.3 Kinetic Monte Carlo Simulations

To simulate hopping transport numerically, kinetic Monte Carlo (KMC) simulations are often used.[10,56,57,62] A KMC simulation can be performed if there are a discrete number of states and rates for changing between configurations can be calculated. In organic semiconductors, the distribution of mobile charge carriers over the hopping sites can be considered a state, while a Miller-Abrahams hopping rates can be used to calculate transition between those states.[28]

First, the system is initialized in a state with a certain configuration of mobile charge carriers. The initial state is not critical for the simulations in this thesis, as results are only recorded after entering a steady-state. For all possible hops, Miller-Abrahams hopping rates ω_{ij} from initial site i to final site j, are calculated. If the initial site is lower in energy than the target site, the rates are[28]

$$\omega_{ij} = \omega_0 \exp\left(-\alpha r_{ij}\right) \exp\left(-\frac{\Delta E_{ij}}{kT}\right), \tag{1.12}$$

where ω_0 is the attempt to jump frequency, α is the inverse localization length, r_{ij} is the distance between site i and j, E_{ij} is the energy difference between site i and j. If the target site is lower in energy, Boltzmann term becomes 1 and only ω_0, α, and r_{ij} affect the hopping rate.

For a typical localization length of 0.1 nm, hops to non-nearest neighbours are rare, so only rates to the first few nearest neighbours are calculated for every charge carrier.[50,62] A random hop is then performed, where each hop k is picked with a probability of

$$p_k = \frac{\omega_{ij}}{\Omega}, \tag{1.13}$$

where Ω is the sum of all individual rates ω_{ij}. Because two consecutive hops are independent, the hopping process can be regarded as a Poisson process.[63] This means that the lifetime of a state can be determined by an exponentially distributed random number and the total rate Ω as

$$\tau_{\text{state}} = \frac{\log r}{\Omega} \tag{1.14}$$

After performing a hop, the hopping rates should be updated to account for the change in Coulomb potential and site occupation because of the new position of one of the charge carriers. Typically, only rates for charge carriers close to the carrier that hopped are calculated to restrict the computational effort required.[62]

This process is repeated until the statistical error on the derived variables is acceptable. For thermoelectric performance, the conductivity and Seebeck coefficient should be calculated. Determination of the conductivity is done from the mobility and number of charge carriers via equation 1.8. The mobility can be determined by dividing the total distance travelled along the electric field direction by the simulation time, the electric field, and number of particles. The Seebeck coefficient can be extracted using equation 1.9 by using the average energy between the initial and final site for the hop in the Peltier coefficient.

1.3 Perovskite Solar Cells

While perovskites can be applied in many devices, the one that will be the focus of this thesis is the perovskite solar cell. A perovskite solar cell typically has a device structure as indicated in figure 1.3a. The perovskite absorber layer is sandwiched between transport layers on either side and electrodes on top of the transport layers. At least one of the contacts and TLs should be transparent to allow for light absorption in the perovskite, but if the solar cell is used as a top cell in a tandem structure, all contacts and TLs should be transparent.[64] The solar cell operates by absorbing light, exciting an electron from the valence to conduction band. This results in an electron in the conduction band and a hole in the valence band. Some kind of asymmetry is needed to then selectively move holes and electrons to the opposite contacts.[65–67]

First, perovskite solar cells typically have a work function difference between the electron and hole contacts. This work function difference results in an internal electric field in the solar cell, driving electrons and holes in opposite directions. Also doping the transport layers can yield a built-in potential, meaning it is often not clear what exactly constitutes the built-in voltage. Secondly, the transport layers, as illustrated in figure 1.3a, allow only one type of carrier to enter, reducing surface recombination at the contacts.[24] This allows the solar cell to operate even if the internal electrical field works against extraction.[67]

While solar cells of a similar structure can be made from a wide range of materials, perovskites have a few distinct advantages. Metal halide perovskites in general have very large absorption coefficients,[14] because of their (almost) direct bandgap.[15,68,69] Despite their modest charge carrier mobilities,[70–72] perovskites have high charge carrier lifetimes and long diffusion lengths (> 1 μm).[73–75] This makes them good candidates for absorber materials, as the absorber layer can be kept thin and losses low.

Furthermore, small exciton binding energies[15,16,76] and high dielectric constants[17,18] mean that excitons dissociate though thermal energy, forming free electrons and holes.[77] Because the bandgap can be tuned though substitution of halides,[78,79] the bandgap can be made to complement that of silicon for a tandem configuration,[80,81] improving efficiency to roughly 30% at the time of writing.[7]

There are still some limits on perovskite solar cells that can hinder their application. Recombination on the interface between the perovskite and transport layers typically limits performance.[34–38] Especially for wide band gap cells, there can be considerable losses there.[34,65,82,83] While the efficiency of perovskite solar cells has come a long way, one of the major hurdles for application remains their relatively limited stability.[84,85]

1.3.1 Drift-Diffusion Simulations

The way perovskite solar cells are often modelled is through 1-dimensional drift-diffusion simulations. This approach uses a coupled set of continuity equations with the Poisson equation. In steady-state, the continuity equations are[86]

$$\frac{\partial J_n}{\partial x} = -q(G - R) \tag{1.15}$$

$$\frac{\partial J_p}{\partial x} = q(G - R), \tag{1.16}$$

where the electron and hole currents J_n/p along spatial coordinate x are expressed in terms of free carrier generation G and recombination R. The electron and hole current can be expanded to contain a drift term and a diffusion term[86]

$$J_n = -qn\mu_n \frac{\partial V}{\partial x} + qD_n \frac{\partial n}{\partial x} \tag{1.17}$$

$$J_p = -qp\mu_p \frac{\partial V}{\partial x} - qD_p \frac{\partial p}{\partial x}, \tag{1.18}$$

where D_n/p are the electron and hole diffusion coefficient.[86]

The Poisson equation,

$$\frac{\partial}{\partial x}\Big(\varepsilon(x)\frac{\partial V(x)}{\partial x}\Big) = -q\big(p(x) - n(x) + C(x)\big), \tag{1.19}$$

where ε is the dielectric constant, V is the electrostatic potential, n/p are the electron and hole densities, and C is the sum of all additional charges, like ions or traps.[86]

One of the advantages of this type of drift-diffusion simulation is the flexibility of these equations. To simulate a perovskite solar cell, any desired generation and recombination process can be entered into the continuity equations. Effects of band alignment and effective density of states can be added through the electrostatic potential in the Poisson equation.[87] Moreover, mobile ions can be accounted for using an additional set of continuity equations. The resulting simulations can often quantitatively fit experimental data.[88–90]

1.4 Outline of This Thesis

In chapter 2 we look into a methodology for simulating perovskite solar cells. These solar cells feature a perovskite layer that generates electron hole pairs under illumination. The perovskite layer is sandwiched between an n-type and p-type transport layer that block opposite sign carriers from entering. One of the interesting properties of perovskites is that despite typically large defect densities, the bulk material shows long charge carrier lifetimes. This makes defects at the interface between the transport layers responsible for the bulk of the recombination. Because the transport layers are often organic, many material properties vary wildly over this interface, such as the dielectric constant, band energies, and effective density of states. This makes the description of these interfaces of primary importance in the simulation of perovskite solar cells.

To increase the accuracy of the recombination model on this interface, we extend the regular Shockley-Read-Hall model to allow for trapping of charges from either side of the interface. We introduce steady-state and transient rates for interfacial recombination and provide some handles for improving numerical stability. We find that current-voltage characteristics resulting from the improved interfacial trapping model can differ strongly from simpler implementations. This highlights the importance of a rigorous description of interfaces for the simulation of perovskite solar cells.

In chapter 3 we will use our description of interfacial recombination to investigate wide band gap perovskite solar cells. The most likely avenue for the application of perovskite solar cells seems to be a tandem configuration with traditional silicon solar cells. In this configuration, high-energy photons are absorbed in the wide band gap perovskite top cell, while low-energy photons are absorbed in a silicon solar cell with a narrower band gap. While technologically relevant, these wide band gap perovskite cells lag in efficiency compared to intermediate bandgap perovskite solar cells, especially in terms of open circuit voltage. We investigate a wide range of effects, but find that the open circuit voltage is very sensitive to band alignment, unsurprising perhaps. We find, however, that for optimal band alignment, the effective density of states difference between the transport layer determines the optimal band offset between the layers.

In chapter 4 we will investigate the phenomenon of conductivity decrease at high dopant loading in doped organic semiconductors. Based on a Gaussian disorder model, one would expect the conductivity of these materials to keep increasing with increasing doping density. Experimentally, it is often observed that the conductivity increases, peaks, and then decreases with increasing dopant loading. This effect is often attributed to the poor morphology of highly doped organic semiconductors. The effect is observed in a wide range of materials, however, so a more general phenomenon seems a likely cause. We show both analytically and using kinetic Monte Carlo simulation that this effect is likely caused by carrier-carrier interactions at high charge carrier density. These carrier-carrier interactions manifest themselves in a Coulomb pseudo-gap at room temperature, limiting the conductivity at high charge carrier density.

One of the primary reasons to dope organic materials to a very high degree, is to attain the optimal charge carrier density for organic thermoelectrics. These materials are used for extracting electrical energy from a temperature gradient. Their performance scales linearly with conductivity and with the Seebeck coefficient squared. Experimentally, however, an increased conductivity often coincides with a decreased Seebeck coefficient and vice versa. In chapter 5 we discuss the effect of carrier-carrier interactions on thermoelectric performance of doped organic semiconductors. We find that carrier-carrier interactions not only reduce conductivity as discussed in chapter 4, but also the Seebeck coefficient. This means that reducing carrier-carrier interactions could be a promising strategy for increasing thermoelectric performance in doped organic semiconductors.

Bibliography

[1] H. Shirakawa, E. J. Louis, A. G. MacDiarmid, C. K. Chiang, A. J. Heeger, *Journal of the Chemical Society Chemical Communications* **1977**, 578–580.

[2] T. A. Skotheim, *Handbook of conducting polymers*, CRC press, **1997**.

[3] G. Yu, J. Gao, J. C. Hummelen, F. Wudl, A. J. Heeger, *Science* **1995**, *270*, 1789–1791.

[4] J. H. Burroughes, D. D. Bradley, A. Brown, R. Marks, K. Mackay, R. H. Friend, P. L. Burns, A. B. Holmes, *nature* **1990**, *347*, 539–541.

[5] C. K. Mytafides, L. Tzounis, G. Karalis, P. Formanek, A. S. Paipetis, *ACS Applied Materials & Interfaces* **2021**, *13*, 11151–11165.

[6] G. Horowitz, *Advanced materials* **1998**, *10*, 365–377.

[7] Best Research-Cell Efficiency Chart, **2022**, `https://www.nrel.gov/pv/cell-efficiency.html` (visited on 04/06/2022).

[8] OLED Market with COVID-19 Impact Analysis by Product Type, **2021**, `https://www.marketsandmarkets.com/Market-Reports/oled-market-200.html` (visited on 04/06/2022).

[9] H. Bässler, *Philosophical Magazine B* **1984**, *50*, 347–362.

[10] H. Bässler, *Physica Status Solidi B (Basic Research);(Germany)* **1993**, *175*.

[11] V. I. Arkhipov, P. Heremans, E. V. Emelianova, G. J. Adriaenssens, H. Bässler, *J. Phys. Condens. Matter* **2002**, *14*, 9899–9911.

[12] M. C. J. M. Vissenberg, M. Matters, *Phys. Rev. B* **1998**, *57*, 12964–12967.

[13] Q. A. Akkerman, L. Manna, *ACS Energy Letters* **2020**, *5*, 604–610.

[14] E. T. Hoke, D. J. Slotcavage, E. R. Dohner, A. R. Bowring, H. I. Karunadasa, M. D. McGehee, *Chemical Science* **2015**, *6*, 613–617.

[15] F. Brivio, K. T. Butler, A. Walsh, M. Van Schilfgaarde, *Physical Review B* **2014**, *89*, 155204.

[16] J. M. Frost, K. T. Butler, F. Brivio, C. H. Hendon, M. Van Schilfgaarde, A. Walsh, *Nano letters* **2014**, *14*, 2584–2590.

[17] N. Onoda-Yamamuro, T. Matsuo, H. Suga, *Journal of Physics and Chemistry of Solids* **1992**, *53*, 935–939.

[18] J. N. Wilson, J. M. Frost, S. K. Wallace, A. Walsh, *APL Materials* **2019**, *7*, 010901.

[19] A. Kojima, K. Teshima, Y. Shirai, T. Miyasaka, *Journal of the American Chemical Society* **2009**, *131*, PMID: 19366264, 6050–6051.

[20] W. Yu, F. Li, L. Yu, M. R. Niazi, Y. Zou, D. Corzo, A. Basu, C. Ma, S. Dey, M. L. Tietze, et al., *Nature communications* **2018**, *9*, 1–10.

[21] K. Lin, J. Xing, L. N. Quan, F. De Arquer, X. Gong, J. Lu, L. Xie, W. Zhao, D. Zhang, C. Yan, et al., *Nature* **2018**, *562*, 245–248.

[22] J. W. Fergus, *Sensors and Actuators B: Chemical* **2007**, *123*, 1169–1179.

[23] I. M. Peters, H. Liu, T. Reindl, T. Buonassisi, *Joule* **2018**, *2*, 307–322.

[24] J. A. Nelson, *The physics of solar cells*, World Scientific Publishing Company, **2003**.

[25] C. Kittel, P. McEuen, *Kittel's Introduction to Solid State Physics*, John Wiley & Sons, **2018**.

[26] J.-L. Bredas, *Materials Horizons* **2014**, *1*, 17–19.

[27] H. Bässler, D. Kroh, F. Schauer, V. Nádaždy, A. Köhler, *Advanced Functional Materials* **2021**, *31*, 2007738.

[28] A. Miller, E. Abrahams, *Phys. Rev.* **1960**, *120*, 745–755.

[29] R. A. Marcus, N. Sutin, *Biochimica et Biophysica Acta (BBA)-Reviews on Bioenergetics* **1985**, *811*, 265–322.

[30] X. de Vries, P. Friederich, W. Wenzel, R. Coehoorn, P. A. Bobbert, *Phys. Rev. B* **2018**, *97*, 075203.

[31] P. Langevin, *Ann. Chim. Phys* **1903**, *28*, 122.

[32] C. Wehrenfennig, G. E. Eperon, M. B. Johnston, H. J. Snaith, L. M. Herz, *Advanced materials* **2014**, *26*, 1584–1589.

[33] W. Shockley, W. T. Read, *Phys. Rev.* **1952**, *87*, 835–842.

[34] S. Mahesh, J. M. Ball, R. D. J. Oliver, D. P. McMeekin, P. K. Nayak, M. B. Johnston, H. J. Snaith, *Energy Environ. Sci.* **2020**, *13*, 258–267.

[35] T. S. Sherkar, C. Momblona, L. Gil-Escrig, H. J. Bolink, L. J. A. Koster, *Advanced Energy Materials* **2017**, *7*, 1602432.

[36] L. Krückemeier, B. Krogmeier, Z. Liu, U. Rau, T. Kirchartz, *Advanced Energy Materials* **2021**, *11*, 2003489.

[37] M. Stolterfoht, C. M. Wolff, J. A. Márquez, S. Zhang, C. J. Hages, D. Rothhardt, S. Albrecht, P. L. Burn, P. Meredith, T. Unold, D. Neher, *Nature Energy* **2018**, *3*, 847–854.

[38] Q. Jiang, Y. Zhao, X. Zhang, X. Yang, Y. Chen, Z. Chu, Q. Ye, X. Li, Z. Yin, J. You, *Nature Photonics* **2019**, *13*, 460–466.

[39] L. M. Pazos-Outón, T. P. Xiao, E. Yablonovitch, *The journal of physical chemistry letters* **2018**, *9*, 1703–1711.

[40] W. Tress, *Advanced Energy Materials* **2017**, *7*, 1602358.

[41] A. D. Scaccabarozzi, A. Basu, F. Aniés, J. Liu, O. Zapata-Arteaga, R. Warren, Y. Firdaus, M. I. Nugraha, Y. Lin, M. Campoy-Quiles, et al., *Chemical Reviews* **2021**.

[42] I. Salzmann, G. Heimel, M. Oehzelt, S. Winkler, N. Koch, *Accounts of chemical research* **2016**, *49*, 370–378.

[43] I. Salzmann, G. Heimel, *Journal of Electron Spectroscopy and Related Phenomena* **2015**, *204*, 208–222.

[44] I. E. Jacobs, A. J. Moulé, *Advanced Materials* **2017**, *29*, 1703063.

[45] P. Würfel, *Physik der Solarzellen*, Springer, **2000**.

[46] J. M. Ziman, *Principles of the Theory of Solids*, Cambridge university press, **1972**.

[47] D.M. Rowe, *Thermoelectrics handbook*, Taylor & Francis, **2006**, p. 1008.

[48] C. J. Vineis, A. Shakouri, A. Majumdar, M. G. Kanatzidis, *Advanced materials* **2010**, *22*, 3970–3980.

[49] Y.-J. Zeng, D. Wu, X.-H. Cao, W.-X. Zhou, L.-M. Tang, K.-Q. Chen, *Advanced Functional Materials* **2020**, *30*, 1903873.

[50] W. F. Pasveer, J. Cottaar, C. Tanase, R. Coehoorn, P. A. Bobbert, P. W. M. Blom, D. M. de Leeuw, M. A. J. Michels, *Phys. Rev. Lett.* **2005**, *94*, 206601.

[51] V. I. Arkhipov, E. V. Emelianova, P. Heremans, H. Bässler, *Phys. Rev. B* **2005**, *72*, 235202.

[52] V. I. Arkhipov, P. Heremans, E. V. Emelianova, H. Bässler, *Phys. Rev. B* **2005**, *71*, 045214.

[53] M. Schwarze, C. Gaul, R. Scholz, F. Bussolotti, A. Hofacker, K. S. Schellhammer, B. Nell, B. D. Naab, Z. Bao, D. Spoltore, K. Vandewal, J. Widmer, S. Kera, N. Ueno, F. Ortmann, K. Leo, *Nat. Mater.* **2019**, *18*, 242–248.

[54] A. Abate, D. R. Staff, D. J. Hollman, H. J. Snaith, A. B. Walker, *Phys. Chem. Chem. Phys.* **2014**, *16*, 1132–1138.

[55] H. Fritzsche, *Solid State Communications* **1971**, *9*, 1813–1815.

[56] K. Xu, T.-P. Ruoko, M. Shokrani, D. Scheunemann, H. Abdalla, H. Sun, C.-Y. Yang, Y. Puttisong, N. B. Kolhe, J. S. M. Figueroa, et al., *Advanced Functional Materials* **2022**, 2112276.

[57] M. Koopmans, L. J. A. Koster, *Applied Physics Letters* **2021**, *119*, 143301.

[58] G. Zuo, X. Liu, M. Fahlman, M. Kemerink, *Advanced Functional Materials* **2018**, *28*, 1703280.

[59] G. Zuo, Z. Li, E. Wang, M. Kemerink, *Advanced Electronic Materials* **2018**, *4*, 1700501.

[60] J. Liu, B. van der Zee, R. Alessandri, S. Sami, J. Dong, M. I. Nugraha, A. J. Barker, S. Rousseva, L. Qiu, X. Qiu, et al., *Nature communications* **2020**, *11*, 1–9.

[61] J. Liu, L. Qiu, G. Portale, M. Koopmans, G. Ten Brink, J. C. Hummelen, L. J. A. Koster, *Advanced Materials* **2017**, *29*, 1701641.

[62] F. Liu, H. van Eersel, B. Xu, J. G. Wilbers, M. P. de Jong, W. G. van der Wiel, P. A. Bobbert, R. Coehoorn, *Physical Review B* **2017**, *96*, 205203.

[63] M. H. Kalos, P. A. Whitlock, *Monte carlo methods*, John Wiley & Sons, **2009**.

[64] Y. Jiang, I. Almansouri, S. Huang, T. Young, Y. Li, Y. Peng, Q. Hou, L. Spiccia, U. Bach, Y.-B. Cheng, et al., *Journal of Materials Chemistry C* **2016**, *4*, 5679–5689.

[65] S. Kavadiya, A. Onno, C. C. Boyd, X. Wang, A. Cetta, M. D. McGehee, Z. C. Holman, *Solar RRL* **2021**, *5*, 2100107.

[66] J. Diekmann, P. Caprioglio, M. H. Futscher, V. M. Le Corre, S. Reichert, F. Jaiser, M. Arvind, L. P. Toro, E. Gutierrez-Partida, F. Peña-Camargo, C. Deibel, B. Ehrler, T. Unold, T. Kirchartz, D. Neher, M. Stolterfoht, *Solar RRL* **2021**, *5*, 2100219.

[67] U. Würfel, A. Cuevas, P. Würfel, *IEEE Journal of Photovoltaics* **2015**, *5*, 461–469.

[68] V. Sarritzu, N. Sestu, D. Marongiu, X. Chang, Q. Wang, S. Masi, S. Colella, A. Rizzo, A. Gocalinska, E. Pelucchi, et al., *Advanced Optical Materials* **2018**, *6*, 1701254.

[69] T. Wang, B. Daiber, J. M. Frost, S. A. Mann, E. C. Garnett, A. Walsh, B. Ehrler, *Energy & Environmental Science* **2017**, *10*, 509–515.

[70] C. Q. Xia, J. Peng, S. Poncé, J. B. Patel, A. D. Wright, T. W. Crothers, M. Uller Rothmann, J. Borchert, R. L. Milot, H. Kraus, et al., *The journal of physical chemistry letters* **2021**, *12*, 3607–3617.

[71] B. Maynard, Q. Long, E. A. Schiff, M. Yang, K. Zhu, R. Kottokkaran, H. Abbas, V. L. Dalal, *Applied Physics Letters* **2016**, *108*, 173505.

[72] J. Lim, M. T. Hörantner, N. Sakai, J. M. Ball, S. Mahesh, N. K. Noel, Y.-H. Lin, J. B. Patel, D. P. McMeekin, M. B. Johnston, et al., *Energy & Environmental Science* **2019**, *12*, 169–176.

[73] A. A. Zhumekenov, M. I. Saidaminov, M. A. Haque, E. Alarousu, S. P. Sarmah, B. Murali, I. Dursun, X.-H. Miao, A. L. Abdelhady, T. Wu, et al., *ACS Energy Letters* **2016**, *1*, 32–37.

[74] S. D. Stranks, G. E. Eperon, G. Grancini, C. Menelaou, M. J. Alcocer, T. Leijtens, L. M. Herz, A. Petrozza, H. J. Snaith, *Science* **2013**, *342*, 341–344.

[75] G. Xing, N. Mathews, S. Sun, S. S. Lim, Y. M. Lam, M. Grätzel, S. Mhaisalkar, T. C. Sum, *Science* **2013**, *342*, 344–347.

[76] A. Miyata, A. Mitioglu, P. Plochocka, O. Portugall, J. T.-W. Wang, S. D. Stranks, H. J. Snaith, R. J. Nicholas, *Nature Physics* **2015**, *11*, 582–587.

[77] V. D'innocenzo, G. Grancini, M. J. Alcocer, A. R. S. Kandada, S. D. Stranks, M. M. Lee, G. Lanzani, H. J. Snaith, A. Petrozza, *Nature communications* **2014**, *5*, 1–6.

[78] L. Protesescu, S. Yakunin, M. I. Bodnarchuk, F. Krieg, R. Caputo, C. H. Hendon, R. X. Yang, A. Walsh, M. V. Kovalenko, *Nano letters* **2015**, *15*, 3692–3696.

[79] N. Kitazawa, Y. Watanabe, Y. Nakamura, *Journal of materials science* **2002**, *37*, 3585–3587.

[80] F. Sahli, J. Werner, B. A. Kamino, M. Bräuninger, R. Monnard, B. Paviet-Salomon, L. Barraud, L. Ding, J. J. Diaz Leon, D. Sacchetto, et al., *Nature materials* **2018**, *17*, 820–826.

[81] J. Werner, B. Niesen, C. Ballif, *Advanced Materials Interfaces* **2018**, *5*, 1700731.

[82] L. Gil-Escrig, C. Dreessen, F. Palazon, Z. Hawash, E. Moons, S. Albrecht, M. Sessolo, H. J. Bolink, *ACS Energy Letters* **2021**, *6*, PMID: 34568574, 827–836.

[83] X. Liu, Z. Wu, X. Fu, L. Tang, J. Li, J. Gong, X. Xiao, *Nano Energy* **2021**, *86*, 106114.

[84] D. Wang, M. Wright, N. K. Elumalai, A. Uddin, *Solar Energy Materials and Solar Cells* **2016**, *147*, 255–275.

[85] N. Li, X. Niu, Q. Chen, H. Zhou, *Chemical Society Reviews* **2020**, *49*, 8235–8286.

[86] Siegfried Selberherr, *Analysis and Simulation of Semiconductor Devices*, Springer, Vienna, **1984**.

[87] C. M. Snowden, *Introduction to semiconductor device modelling*, World Scientific, **1998**.

[88] V. M. Le Corre, E. A. Duijnstee, O. El Tambouli, J. M. Ball, H. J. Snaith, J. Lim, L. J. A. Koster, *ACS energy letters* **2021**, *6*, 1087–1094.

[89] D. Hu, Q. Yang, H. Chen, F. Wobben, V. M. Le Corre, R. Singh, T. Liu, R. Ma, H. Tang, L. J. A. Koster, et al., *Energy & Environmental Science* **2020**, *13*, 2134–2141.

[90] V. M. Le Corre, M. Stolterfoht, L. Perdigon Toro, M. Feuerstein, C. Wolff, L. Gil-Escrig, H. J. Bolink, D. Neher, L. J. A. Koster, *ACS Applied Energy Materials* **2019**, *2*, 6280–6287.

CHAPTER 2

Interfacial Trap-Assisted Recombination

The physics of solar cells is often modelled using a combination of two different techniques. A transfer matrix model is used for simulating the optics, from incoming light to absorption by the solar cell.[1] The resulting absorption profile is then used as input for a drift-diffusion model, which models the electrical stage, from electron hole pair creation to extraction by the electrodes.

This drift-diffusion model consists of a coupled set of continuity equations that relate the electron and hole currents J_n and J_p to the net recombination $G - R$ at position x. In steady-state this results in the continuity equations

$$\frac{\partial J_n(x)}{\partial x} = -\frac{\partial J_p(x)}{\partial x} = -q(G(x) - R(x)), \tag{2.1}$$

and a Poisson equation that relates the potential V to the charge density at position x

$$\frac{\partial}{\partial x}\left(\varepsilon(x)\frac{\partial V(x)}{\partial x}\right) = q(n(x) - p(x) + C(x)), \tag{2.2}$$

where ε is the dielectric constant, n and p are the electron and hole densities, and C is the density of additional charges, such as ions or traps.[2]

The continuity equations make sure that generation, recombination, and movement are balanced so that we do not create charge out of nothing. The

Poisson equation takes care of the electrostatic potential, which is one of the driving forces for moving all the charged particles in the solar cell. To find a solution that satisfies both the continuity equations and the Poisson equation, the Gummel iteration method is used.[2]

What physics should be present in the drift-diffusion model depends on what is being simulated. For perovskite solar cells, there are a few different relevant factors: 1) electrons and holes, for which generation recombination and movement is governed by the continuity equations, but also contribute to the Poisson equation via their charge; 2) other charged particles, such as dopants, or mobile ions. These contribute to the Poisson equation, but in case of mobile ions are allowed to move as well; 3) effects that represent the band diagram, such as band energy level and effective density of states. These effects again can be captured in the Poisson equation by locally modifying the potential for positive and negative particles separately;[3–5] 4) generation and recombination processes, which enter into the continuity equations. For perovskites, typically the absorption is calculated from a transfer matrix model and agrees quantitatively with experimental observation.[6] Direct, or band-to-band recombination is typically included in perovskite device models, but trap-assisted recombination is the performance limiting recombination process in perovskite solar cells[6–10] and will be the focus of this chapter.

2.1 Physical Model for Defect Assisted Recombination

The physical model for trap-assisted recombination was first introduced for use in inorganic semiconductors in 1952.[11,12] The model describes bulk defects that can capture from and emit to either the conduction or valence band, as indicated in figure 2.1 (2). This process is often called Shockley-Read-Hall (SRH) recombination, and can be derived by stating that the 4 processes that can occur from a trap must follow detailed balance. The 4 processes are electron trapping and detrapping and hole trapping and detrapping, as shown in figure 2.1 (2). For the trapping as introduced by Shockley and Read,[11,12] we have 4 processes

$$R_n = C_n \cdot n \cdot N_t \cdot (1 - f_t) \tag{2.3}$$

$$R_p = C_p \cdot p \cdot N_t \cdot f_t \tag{2.4}$$

$$G_n = C_n \cdot n_t \cdot N_t f_t \tag{2.5}$$

$$G_p = C_p \cdot p_t \cdot N_t (1 - f_t), \tag{2.6}$$

where Eq. 2.3 is equation 2.5 as published by Shockley and Read[11] and Eq. 2.4 are the capture rates for electrons and holes respectively and Eq. 2.5 and Eq. 2.6 are the emission rates for electrons and holes, N_t is the density of traps, n and p

are the electron and hole densities, n_t and p_t are electron and hole densities when the quasi Fermi level matches the trap energy, C_n and C_p are the electron and hole capture coefficients, and f_t is the fraction of filled traps. In steady-state, the net SRH recombination rate can then be expressed as

$$R_{\text{net}} = R_n - G_n = R_p - G_p, \tag{2.7}$$

by substituting f_t.

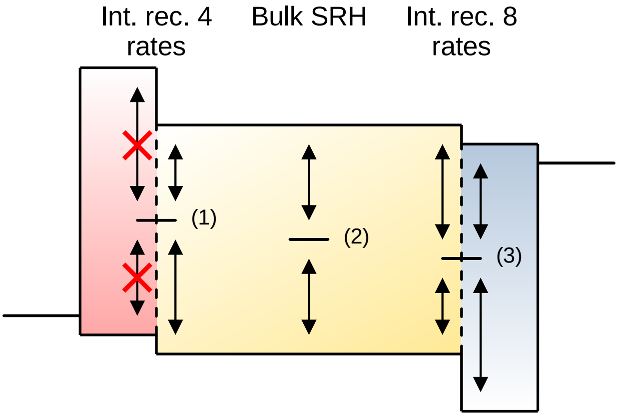

Figure 2.1: A schematic band diagram of a perovskite solar cell, where dashed lines indicate interfaces between perovskite and transport layers. In it, the difference between regular SRH (2) and interface trapping (1) and (3) is shown. Interface trapping can be implemented with 4 rates (1) like regular SRH recombination, or more accurately with 8 rates (3), where the number of rates is doubled, as every trapping and detrapping process is allowed to the left and right of the interface.

Figure 2.1 shows a schematic band diagram of a perovskite solar cell, where interfacial recombination is typically the primary recombination mechanism.[6–10] If a trap sits at an interface, capture and emission is possible from either side of the interface, as indicated in figure 2.1 (3).[13] This means that there are double the number of rates compared to regular SRH recombination, 8 in total.

These 8 rates are

$$R_{n^+} = C_{cn+} \cdot n^+ \cdot N_t \cdot (1 - f_t) = a^+ \cdot (1 - f_t) \tag{2.8}$$

$$
\begin{aligned}
R_{n^-} &= C_{cn-} \cdot n^- \cdot N_t \cdot (1 - f_t) = a^- \cdot (1 - f_t) && (2.9)\\
R_{p^+} &= C_{cp+} \cdot p^+ \cdot N_t \cdot f_t = b^+ \cdot f_t && (2.10)\\
R_{p^-} &= C_{cp-} \cdot p^- \cdot N_t \cdot f_t = b^- \cdot f_t && (2.11)\\
G_{n^+} &= C_{en+} \cdot n_t^+ \cdot N_t \cdot f_t = c^+ \cdot f_t && (2.12)\\
G_{n^-} &= C_{en-} \cdot n_t^- \cdot N_t \cdot f_t = c^- \cdot f_t && (2.13)\\
G_{p^+} &= C_{ep+} \cdot p_t^+ \cdot N_t \cdot (1 - f_t) = d^+ \cdot (1 - f_t) && (2.14)\\
G_{p^-} &= C_{ep-} \cdot p_t^- \cdot N_t \cdot (1 - f_t) = d^- \cdot (1 - f_t), && (2.15)
\end{aligned}
$$

where the left and right side of the interface are denoted by $-$ and $+$.

Assuming an equal C_n and C_p left and right of the interface, the ratio of rates from the left and right side of the interface depends on the difference in n, p, n_t, and p_t at the left and right side of the interface. Typical causes of n, p, n_t, and p_t offsets in perovskite solar cells are band-offsets and differences in effective density of states. These offsets will vary device to device, making it risky to simply discard half the rates, as indicated in figure 2.1 (1). Therefore, the required extension to the SRH framework for the 8 rates shown before will be discussed in this chapter.

To calculate the above generation and recombination rates, we need to obtain an expression for the trap filling. How this is done depends on whether the system can be considered in a steady-state or not. In section 2.2 we will derive the result for steady-state. We will follow up with the transient case in section 2.3.

2.2 Case I: Steady-State

In steady-state, the filled fraction of interface traps can be solved from the charge carrier densities and parameters defined above. Generation, and recombination rates for electrons and holes must be equal, which yields

$$
\begin{aligned}
R^{SRH} = R_{n^+} + R_{n^-} - G_{n^+} - G_{n^-} &= R_{p^+} + R_{p^-} - G_{p^+} - G_{p^-} && (2.16)\\
(a^+ + a^- + d^+ + d^-) \cdot (1 - f_t) &= (b^+ + b^- + c^+ + c^-) \cdot f_t. && (2.17)
\end{aligned}
$$

This means that for f_t we find

$$
f_t = \frac{a^+ + a^- + d^+ + d^-}{a^+ + a^- + b^+ + b^- + c^+ + c^- + d^+ + d^-} \tag{2.18}
$$

and for $1 - f_t$ we find

$$1 - f_t = \frac{b^+ + b^- + c^+ + c^-}{a^+ + a^- + b^+ + b^- + c^+ + c^- + d^+ + d^-}.$$

To get to discretized continuity equations, we now need to assign positions on the grid to $n_{(t)}^{+/-}$ and $p_{(t)}^{+/-}$. As the charge carrier densities are chosen to be on-grid variables, the interfaces are between-grid. The interfacial traps are chosen to only capture from and emit to the two grid points adjacent to the interface, noting that we derive the equations for a one dimensional grid.

By applying the restriction that no three consecutive points can be next to an interface, we write the net generation on grid point i, or Γ^i, from an interface traps by summing all contributions from grid points $i-1$, i, and $i+1$. By setting the interface trap density to a finite and equal value on the grid points left and right of the traps, and to zero on adjacent grid points, net generation from the traps can be written as

$$\begin{aligned}\Gamma_n^i &= G_{n_i} - R_{n_i} && (2.19)\\ &= c^i \cdot f_t - a^i \cdot (1 - f_t) && (2.20)\\ &= \frac{c^i \cdot \sum_{j=i-1}^{i+1}(a^j + d^j) - a^i \cdot \sum_{j=i-1}^{i+1}(b^j + c^j)}{\sum_{j=i-1}^{i+1}(a^j + b^j + c^j + d^j)}. && (2.21)\end{aligned}$$

For holes, we get

$$\begin{aligned}\Gamma_p^i &= G_{p_i} - R_{p_i} && (2.22)\\ &= d^i \cdot (1 - f_t) - b^i \cdot f_t && (2.23)\\ &= \frac{d^i \cdot \sum_{j=i-1}^{i+1}(b^j + c^j) - b^i \cdot \sum_{j=i-1}^{i+1}(a^j + d^j)}{\sum_{j=i-1}^{i+1}(a^j + b^j + c^j + d^j)}. && (2.24)\end{aligned}$$

2.3 Case II: Transient

In transient simulations, the recombination rates depend on the previous state, so no equilibrium rates can be solved for. The instantaneous net recombination rates for electrons and holes ($U_{n,p}$) are obtained by substituting $f_t(t)$, trap filling at time t in the expressions for net recombination that result from equation 2.8 to 2.15

$$U_n = (C_{n-}n^- + C_{n+}n^+)N_t(1 - f_t(t)) - (C_{n-}n_1^- + C_{n+}n_1^+)N_t f_t(t) \qquad (2.25)$$

$$U_p = (C_{p-}p^- + C_{p+}p^+)N_t f_t(t) - (C_{p-}p_1^- + C_{p+}p_1^+)N_t(1 - f_t(t)), \tag{2.26}$$

where f_t is calculated using the value from the previous time step and calculating the emission and absorption rates based on the new particle densities found in the current time step.

One should recognize that $f_t(t)$ can be expressed as a differential equation, as depicted in figure 2.2. This is done by solving the ordinary differential equation,

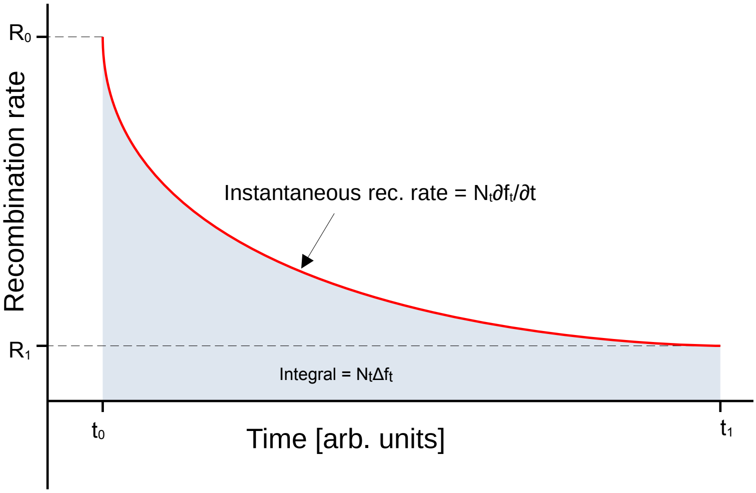

Figure 2.2: Recombination rate over time, where the integral from t_0 to t_1 is the total number of recombined charge carriers between t_0 and t_1.

$$\begin{aligned} \frac{\partial f_t(t)}{\partial t} =& C_n(n^- + n^+)(1 - f_t(t)) - C_n(n_1^- + n_1^+)f_t(t) \\ &+ C_p(p_1^- + p_1^+)(1 - f_t(t)) - C_p(p^- + p^+)f_t(t), \end{aligned} \tag{2.27}$$

where C_n and C_p are the capture coefficients for electrons and holes and $n(p)_1$ is the electron (hole) density when the quasi-Fermi level matches the trap energy.

We get a solution

$$\begin{aligned} f_t(t) =& \frac{C_n(n^- + n^+) + C_p(p_1^- + p_1^+)}{C_n(n^- + n^+ + n_1^- + n_1^+) + C_p(p_1^- + p_1^+ + p^- + p^+)} \\ &+ c_1 \exp\bigl(-(C_n(n^- + n^+ + n_1^- + n_1^+) + C_p(p_1^- + p_1^+ + p^- + p^+))t\bigr), \end{aligned} \tag{2.28}$$

where we can express c_1 in terms of the trap filling at the previous time step, $f_t(t_{\text{prev}})$, as

$$c_1 = f_t(t_{\text{prev}}) - \frac{C_n(n^- + n^+) + C_p(p_1^- + p_1^+)}{C_n(n^- + n^+ + n_1^- + n_1^+) + C_p(p_1^- + p_1^+ + p^- + p^+)}. \tag{2.29}$$

Now we can calculate a trap filling at a time t with the new electron and hole densities n, p and $f_t(t_{\text{prev}})$.

To calculate the total recombination in one time step, we now need to integrate the expression for $U_{n/p}$ from equation 2.25 and 2.26 with the expression for $f_t(t)$ from equation 2.28 substituted in. We should note here that for interface traps, we calculate the net recombination rate at one of the two grid points that contribute to the interfacial recombination. The trap filling $f_t(t)$ depends on all 8 rates, however, so in parts of the equation reflecting trap filling we need to sum over the grid points contributing to interfacial recombination. Using the shorthand notation from equations 2.8 to 2.15, we get

$$U_n^i = a^i - (a^i + c^i) f_t(t) \tag{2.30}$$

$$\begin{aligned} \int_0^{\Delta t} U_n^i dt =& a^i t - (a^i + c^i) \sum_{j=i-1}^{i+1} \frac{a^j + d^j}{a^j + b^j + c^j + d^j} t + \\ & \frac{(a^i + c^i) c_1 \exp\Bigl(-\sum_{j=i-1}^{i+1} (a^j + b^j + c^j + d^j) t\Bigr)}{\sum_{j=i-1}^{i+1} a^j + b^j + c^j + d^j} \end{aligned} \tag{2.31}$$

for the total recombination.

Now that we have an exact expression for the total recombination in the transient case, we have made sure that the trap occupancy cannot go above 1 or below 0, regardless of the size of the time step. To calculate the exact recombination rate U^i_{exact} that will enter into the continuity equation, we simply convert the integral, a density, back into a rate by dividing by the time step as

$$U^i_{\text{exact}} = \frac{\int_0^{\Delta t} U_n^i dt}{\Delta t}. \tag{2.32}$$

We now have a recombination rate that we can enter into the continuity equation for both the steady-state and transient regime. Because we also have an expression for the trap filling f_t, we can in principle solve both the continuity and Poisson equations. There is however still the issue of numerical stability. This is what we will address in the next section.

2.4 Improving Numerical Stability

Both recombination and trap filling are non-linear in their respective variables, the carrier densities and potential. This causes stability issues that can be partly resolved by linearizing the recombination rates and trap filling fraction. We will only do this for the steady-state case, starting with the recombination rate and then following up with the trap filling.

Since the amount of recombination may vary wildly when the charge carrier density changes, we linearize the recombination term in charge carrier density. To linearize we use a Taylor series, where we have to account for the fact that we have to add the partial derivatives of the charge carrier densities at grid points $i-1$, i, and $i+1$. This is because for interfacial recombination, the rate also depends on the carrier density at the other side of the interface. The contribution from one of these grid points will be zero as it is not an interface point and therefore N_t^i will be zero. Summing over the three points makes sure that the expression works both when the interface is between point $i-1$ and i, or i and $i+1$. For our Taylor expansion of net interface generation rate, Γ^n_{int} this gives us

$$\Gamma^i_n(\vec{n}) \approx \Gamma^i_n(\vec{n}_{old}) + \sum_{j=i-1}^{i+1} \frac{\partial \Gamma^i_n(\vec{n}_{old})}{\partial n_j}(n^j - n^j_{old}),$$

where $\vec{n}_{old}$ are the electron densities from the previous iteration, which are known and $\vec{n}$ are the electron densities to be calculated. The three partial derivatives are

$$\begin{aligned}
\frac{\partial \Gamma^i_n}{\partial n^{i-1}} &= \frac{c^i a'^{i-1} \sum_{j=i-1}^{i+1}(a^j + b^j + c^j + d^j)}{\left(\sum_{j=i-1}^{i+1}(a^j + b^j + c^j + d^j)\right)^2} \\
&\quad - \frac{a'^{i-1}\left(c^i \sum_{j=i-1}^{i+1}(a^j + d^j) - a^i \sum_{j=i-1}^{i+1}(b^j + c^j)\right)}{\left(\sum_{j=i-1}^{i+1}(a^j + b^j + c^j + d^j)\right)^2} \\
\frac{\partial \Gamma^i_n}{\partial n^{i}} &= \frac{a'^{i}\left(c^i - \sum_{j=i-1}^{i+1}(b^j + c^j)\right) \sum_{j=i-1}^{i+1}(a^j + b^j + c^j + d^j)}{\left(\sum_{j=i-1}^{i+1}(a^j + b^j + c^j + d^j)\right)^2}
\end{aligned} \tag{2.33}$$

$$
- \frac{a'^{i}\big(c^i \sum_{j=i-1}^{i+1}(a^j + d^j) - a^i \sum_{j=i-1}^{i+1}(b^j + c^j)\big)}{\big(\sum_{j=i-1}^{i+1}(a^j + b^j + c^j + d^j)\big)^2} \tag{2.34}
$$

$$
\begin{aligned}
\frac{\partial \Gamma_n^i}{\partial n^{i+1}} = {} & \frac{c^i a'^{i+1} \sum_{j=i-1}^{i+1}(a^j + b^j + c^j + d^j)}{\big(\sum_{j=i-1}^{i+1}(a^j + b^j + c^j + d^j)\big)^2} \\
& - \frac{a^{i+1}\big(c^i \sum_{j=i-1}^{i+1}(a^j + d^j) - a^i \sum_{j=i-1}^{i+1}(b^j + c^j)\big)}{\big(\sum_{j=i-1}^{i+1}(a^j + b^j + c^j + d^j)\big)^2}
\end{aligned} \tag{2.35}
$$

Inserting the Taylor approximation of recombination term Γ_n^i in the continuity equation, gives us

$$
\begin{aligned}
& \Big(\mu_{ni+1/2} B\Big(\frac{V_{i+1} - V_i}{V_t}\Big) h_{i-1} + \frac{\partial \Gamma_n^i(\vec{n}_{old})}{\partial n^{i+1}} \frac{1}{2} L^2 h_i h_{i-1}(h_i + h_{i-1})\Big) n_{i+1} \\
& - \Big[\mu_{ni+1/2} B\Big(\frac{V_i - V_{i+1}}{V_t}\Big) h_{i-1} + \mu_{ni-1/2} B\Big(\frac{V_i - V_{i-1}}{V_t}\Big) h_i \\
& - \frac{\partial \Gamma_n^i(\vec{n}_{old})}{\partial n^i} \frac{1}{2} L^2 h_i h_{i-1}(h_i + h_{i-1})\Big] n_i \\
& + \Big(\mu_{ni-1/2} B\Big(\frac{V_{i-1} - V_i}{V_t}\Big) h_i + \frac{\partial \Gamma_n^i(\vec{n}_{old})}{\partial n^{i-1}} \frac{1}{2} L^2 h_i h_{i-1}(h_i + h_{i-1})\Big) n_{i-1} \\
= {} & - \big(G_i + \Gamma_n^i(\vec{n}_{old}) \\
& - \sum_{j=i-1}^{i+1} \big(\frac{\partial \Gamma_n^i(\vec{n}_{old})}{\partial n_j} n_{old}^j\big)\big) \frac{1}{2} L^2 h_i h_{i-1}(h_i + h_{i-1}),
\end{aligned} \tag{2.36}
$$

where $h_i L$ is the position of gridpoint i in the device, as the continuity equation for electrons. Because of electron-hole symmetry, exchanging all n and p labels and in the shorthand notation the a and b, and c and d labels we can get the continuity equation for holes.

Interface traps also have to enter the Poisson equation as they are charged, either when filled or when empty, depending on the trap type. To make the system of equations stable, however, we need to linearize the interface traps density with respect to the potential. We can linearize the electrons, holes, and interface traps separately to δV_i, so here we will cover only interface traps to keep it simple. Other terms can be added independently. Since f_{ti} depends on both n and p, we can linearize the charges in the Poisson equation by expressing n and p in terms of the potential. Doing so gives us

$$
n = n_i \exp\Big(\frac{V_i + \delta V_i}{V_t}\Big) \exp\Big(-\frac{\phi_n}{V_t}\Big) \tag{2.37}
$$

$$p = n_i \exp\Big(-\frac{V_i + \delta V_i}{V_t}\Big) \exp\Big(+\frac{\phi_p}{V_t}\Big), \tag{2.38}$$

where V_t is the thermal voltage.

Now we can substitute n and p to get a first order Taylor expansion of trap occupancy f_{ti} around $\delta V = 0$ given by

$$f_{ti}(\vec{V} + \delta\vec{V}) \approx f_{ti}(\vec{V}) + \sum_{j=1}^{N} \frac{\partial f_{ti}(\vec{V})}{\partial V_j} \delta V_j.$$

Now we need to find the partial derivatives of f_{ti} with respect to the potential. To do this we substitute equation 2.37 and 2.38 in the expression for f_{ti} in steady-state, equation 2.18. We can then calculate the partial derivative to the potential, as we have an expression $f_{ti}(\vec{V})$. We get a partial derivative of the form

$$\begin{aligned} \frac{\partial}{\partial x}\Big(\frac{d\exp\big(\frac{a+x}{b}\big) + c}{d\exp\big(\frac{a+x}{b}\big) + g\exp\big(\frac{-a-x}{b}\big) + f}\Big) = \\ \frac{d\exp\big(\frac{a+x}{b}\big)}{b\big(d\exp\big(\frac{a+x}{b}\big) + g\exp\big(\frac{-a-x}{b}\big) + f\big)} \\ - \frac{\big(d\exp\big(\frac{a+x}{b}\big) + c\big)\big(d\exp\big(\frac{a+x}{b}\big) - g\exp\big(\frac{-a-x}{b}\big)\big)}{b\big(d\exp\big(\frac{a+x}{b}\big) + g\exp\big(\frac{-a-x}{b}\big) + f\big)^2}, \end{aligned} \tag{2.39}$$

where c and f are a collection of all terms that depend on n_1 and p_1 and are thus constant under changes of the potential.

Taking the partial derivatives and substituting back the charge carrier densities, while using the shorthand notation from Eq. 2.8 to 2.15 we get

$$\begin{aligned} \frac{\partial f_{ti}(n,p)}{\partial V_{i-1}} =& \frac{a^{i-1}}{V_t\big(\sum_{j=i-1}^{i+1}(a^j + b^j + c^j + d^j)\big)} \\ &- \frac{\sum_{j=i-1}^{i+1}(a^j + d^j)(a^{i-1} - b^{i-1})}{V_t\big(\sum_{j=i-1}^{i+1}(a^j + b^j + c^j + d^j)\big)^2} \\ \frac{\partial f_{ti}(n,p)}{\partial V_i} =& \frac{a^i}{V_t\big(\sum_{j=i-1}^{i+1}(a^j + b^j + c^j + d^j)\big)} \\ &- \frac{\sum_{j=i-1}^{i+1}(a^j + d^j)(a^i - b^i)}{V_t\big(\sum_{j=i-1}^{i+1}(a^j + b^j + c^j + d^j)\big)^2} \end{aligned}$$

$$\begin{aligned}\frac{\partial f_{ti}(n,p)}{\partial V_{i+1}} =& \frac{a^{i+1}}{V_t\left(\sum_{j=i-1}^{i+1}(a^j+b^j+c^j+d^j)\right)} \\ &- \frac{\sum_{j=i-1}^{i+1}(a^j+d^j)(a^{i+1}-b^{i+1})}{V_t\left(\sum_{j=i-1}^{i+1}(a^j+b^j+c^j+d^j)\right)^2}.\end{aligned} \tag{2.40}$$

We can now write the Poisson equation as

$$\begin{aligned}&\Big(\frac{h_{i-1}}{h_ih_{i-1}L} + (h_i+h_{i-1})L\frac{qN_t}{4\varepsilon}\frac{\partial f_{ti}(n,p)}{\partial V_{i+1}}\Big)\delta V_{i+1} \\ -&\Big(\frac{(h_{i-1}+h_i)}{h_ih_{i-1}L} - (h_i+h_{i-1})L\frac{qN_t}{4\varepsilon}\frac{\partial f_{ti}(n,p)}{\partial V_i}\Big)\delta V_i \\ +&\Big(\frac{h_i}{h_ih_{i-1}L} + (h_i+h_{i-1})L\frac{qN_t}{4\varepsilon}\frac{\partial f_{ti}(n,p)}{\partial V_{i+1}}\Big)\delta V_{i-1} \\ &= (h_i+h_{i-1})L\frac{q}{2\varepsilon}(n_i - p_i - (q_{tie}-f_{tio})\frac{N_t}{2}) \\ &\quad -\big(\frac{V_{i+1}h_{i-1} - h_{i-1}V_i - h_iV_i + h_iV_{i-1}}{h_ih_{i-1}L}\big).\end{aligned} \tag{2.41}$$

Now that we have stabilized expression for the equations to solve in our drift diffusion model, we will show the relevance of the interfacial recombination model and transient vs steady-state simulations.

2.5 Implications for Perovskite Solar Cells

Whether the description for interface recombination introduced in this chapter is required for a proper physical description of a device depends strongly on the simulated case. In perovskite solar cells, interfacial recombination between the active layer and transport layers is often the bottleneck for device performance.[6–10] This means that interfacial recombination in general is relevant, but if all device parameters are equal left and right of the interface, the 4-rate model will generate the same result as the 8-rate model depicted in figure 2.1. To illustrate this, we ran simulations comparing both models for a prototypical perovskite solar cell, as will be discussed in more detail in chapter 3. This is done using the interfacial recombination model described before, implemented in the open-source drift-diffusion simulation software SIMsalabim.[14] The solar cell parameters are outlined in appendix C.

Figure 2.3 shows the current-voltage (JV-)characteristic of this solar cell. When the effective density of states (N_c) is equal in the perovskite and the TL,

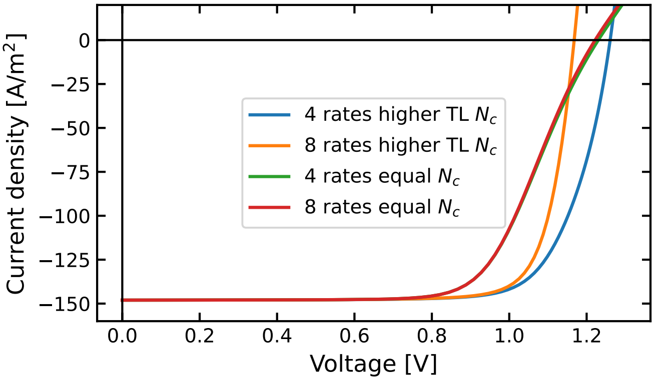

Figure 2.3: The effect of using recombination across an interface (8-rates, Fig 2.1 (3)) or on one side near the interface (4-rates, Fig 2.1 (1)). For the cases with higher transport layer (TL) N_c, the N_c in the TL is set to 10^{27} m^{-3}. In case of equal N_c in the TL and perovskite, both are set to 10^{25} m^{-3}.

it shows that there is hardly a difference between recombining near (4-rates) or across (8-rates) an interface. This is because all relevant parameters that can cause charge carrier density offsets across the interface are equal, so capture rates 2.3 to 2.6 give the same result as rates 2.8 to 2.15.

When N_c is increased in the TL, as is typical for organic TLs (see chapter 3), the JV-characteristic of the solar cell differs strongly between 4-rates or 8-rates. First, the fill-factor (FF) increases. The N_c increase in the TL means that charge carriers increase entropy by moving to the TL, increasing the conductivity, leading to a higher FF. This increase in carrier density in the TL is compensated by a decrease in density at the perovskite side.

Interestingly, whether the open-circuit voltage (V_{oc}) increases or decreases with a higher transport layer N_c depends on the way interfacial recombination is accounted for. When 4 rates are used, the traps are put on the perovskite side of the interface, where the carrier density is lower. This reduces the capture rate for majority carriers, increasing V_{oc}. As for 8 rates, charge carriers are also captured from the TL, where they have higher density, leading to an increase in majority capture rate and a reduced V_{oc}.

As can be seen in figure 2.3, the V_{oc} decreases, while the FF increases when using the 8-rate expression for interfacial recombination. If we include rates from this region of higher charge carrier density, we get a larger recombination rate, which shows up as a sharper kink in the JV-curve around the maximum power point. Increases in recombination naturally lead to a lower V_{oc}, but because of the sharper onset and equivalent transport properties in either cases, also an increased FF.

In transient simulations, a different type of trapping related effect shows up. While in steady state conditions, trap filling is always in equilibrium with the conduction and valence band occupation. This is often not true for transient simulations. Even a simple scan of a JV-curve, which is one of the most used characteristics for solar cells, is in fact, a transient experiment. In perovskite solar cells, ions but also traps contribute to JV-hysteresis when scan rates are in the seconds regime. We performed a dark JV-scan on the same typical perovskite solar cell as previously and discussed in chapter 3. By modifying the voltage in a stepwise way and taking a simulation point slightly after the step, we can eliminate the effect of displacement current and look at ionic and trap contributions.

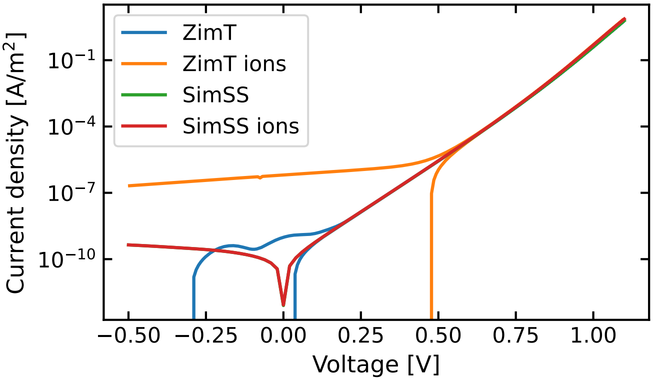

Figure 2.4: Current-voltage characteristic for transient (ZimT) and steady-state scan (SimSS) for cases without and with ions present in the device. The voltage is scanned from -0.5 V to 1.1 V and back over the course of 12 seconds.

Figure 2.4 shows the current-voltage (JV) characteristic resulting from transient and steady-state simulations of the same typical perovskite solar cell as before. A forward and reverse scan are performed in roughly 12 seconds, qualifying this as a 'slow' JV scan. A negative voltage is applied at first, leading to a negative current. The current stays negative even if a positive external voltage is applied because of hysteresis effects. The switch from negative to positive current can be seen to occur at higher applied voltage for simulations including ions than those only including traps.

During the reverse scan, the current stays positive despite the negative applied voltage. The effect is stronger for the case including ions than the case only including traps, where the current stays in the nA/m^2 range, versus the hundreds of nA/m^2's if ions are included. While smaller than the contribution from ions in this case, the relative contribution from traps depends on their distribution and the scan rate. The same trapping and detrapping rates can also be achieved with a higher trap density and lower capture coefficient, this would lead to an increased potential to store charge in traps, leading to increased hysteresis from traps.

For ions, it is known that this hysteresis can be on a long timescale,[15] but we show that even traps contribute to hysteresis in this regime. In all, figure 2.4 shows that for dark scans of perovskites, a steady-state model might not always be accurate. We therefore suggest simulating dark JV-scans using a transient approach that accurately reflects the experiment.

2.6 Conclusions

In this chapter, we have introduced an interfacial recombination model, including capture from and emission to either side of an interface. We found expressions for the recombination rate for steady state conditions and in the transient regime. To address stability issues, we linearized both the recombination rates and Poisson equation under steady-state conditions. We find that the effect of interfacial recombination with 8-rates, as introduced here, can differ from the 4-rate case for a typical perovskite solar cell configuration with organic TLs. V_{oc} differs by about 0.1 V under 1 sun illumination in our simulation. This illustrates the importance of an elaborate interfacial recombination model when investigating band alignment or N_c offsets between active layer and transport layer. Furthermore, we show that in the dark, even a relatively slow JV-scan can end up showing transient effects from either traps or ions in a typical perovskite solar cell. We therefore recommend verifying any steady-state result in the dark on perovskites versus a transient simulation.

Bibliography

[1] G. F. Burkhard, E. T. Hoke, M. D. McGehee, *Advanced Materials* **2010**, *22*, 3293–3297.

[2] Siegfried Selberherr, *Analysis and Simulation of Semiconductor Devices*, Springer, Vienna, **1984**.

[3] C. M. Snowden, *Introduction to semiconductor device modelling*, World Scientific, **1998**.

[4] M. Gruber, B. Stickler, G. Trimmel, F. Schürrer, K. Zojer, *Organic Electronics* **2010**, *11*, 1999–2011.

[5] O. W. Purbo, D. T. Cassidy, S. H. Chisholm, *Journal of applied physics* **1989**, *66*, 5078–5082.

[6] T. S. Sherkar, C. Momblona, L. Gil-Escrig, H. J. Bolink, L. J. A. Koster, *Advanced Energy Materials* **2017**, *7*, 1602432.

[7] S. Mahesh, J. M. Ball, R. D. J. Oliver, D. P. McMeekin, P. K. Nayak, M. B. Johnston, H. J. Snaith, *Energy Environ. Sci.* **2020**, *13*, 258–267.

[8] L. Krückemeier, B. Krogmeier, Z. Liu, U. Rau, T. Kirchartz, *Advanced Energy Materials* **2021**, *11*, 2003489.

[9] M. Stolterfoht, C. M. Wolff, J. A. Márquez, S. Zhang, C. J. Hages, D. Rothhardt, S. Albrecht, P. L. Burn, P. Meredith, T. Unold, D. Neher, *Nature Energy* **2018**, *3*, 847–854.

[10] Q. Jiang, Y. Zhao, X. Zhang, X. Yang, Y. Chen, Z. Chu, Q. Ye, X. Li, Z. Yin, J. You, *Nature Photonics* **2019**, *13*, 460–466.

[11] W. Shockley, W. T. Read, *Phys. Rev.* **1952**, *87*, 835–842.

[12] R. N. Hall, *Phys. Rev.* **1952**, *87*, 387–387.

[13] M. Burgelman, P. Nollet, S. Degrave, *Thin solid films* **2000**, *361*, 527–532.

[14] M. Koopmans, V. M. L. Corre, L. J. A. Koster, *Journal of Open Source Software* **2022**, *7*, 3727.

[15] S. Meloni, T. Moehl, W. Tress, M. Franckevičius, M. Saliba, Y. H. Lee, P. Gao, M. K. Nazeeruddin, S. M. Zakeeruddin, U. Rothlisberger, et al., *Nature communications* **2016**, *7*, 1–9.

CHAPTER 3

Voltage Deficit in Wide Band Gap Perovskite Solar Cells

Abstract

Wide-bandgap ($\gtrapprox$ 1.7 eV) perovskite solar cells are plagued by relatively low open-circuit voltages. This is problematic as they are key to achieving perovskite silicon tandems, that can boost the potential of silicon solar cells. Performance in perovskite solar cells is widely considered to be limited by recombination at the interface between perovskite and transport layer.

Here, we introduce a number of design rules to increase the open-circuit voltage of wide-bandgap perovskite solar cells. We present a numerical device model that includes a detailed description of the interfacial recombination processes. We investigate the combined effects of interface traps, ions, band alignment, and transport properties to identify critical parameters for improving the open-circuit voltage. We simulate a large number of devices by picking random combinations of parameters and look for trends. We show that interface recombination can be suppressed by reducing the minority carrier density close to the interface with the transport layers. We demonstrate that alignment of energy levels is only part of the story; the effective densities of states are of equal importance. Our results pave the way to achieving high open-circuit voltages, despite a significant density of interface defects.

3.1 Introduction

Perovskite solar cell (PSC) technology is maturing rapidly. Formamidinium lead iodide cells show an efficiency that is on par with silicon cells and are nearing the Shockley-Queisser limit for the open-circuit voltage.[1] The stability of these solar cells is starting to attract more attention, as degradation mechanisms are not yet fully understood.

One of the most likely applications for perovskite solar cells is in a tandem configuration with silicon solar cells. This perovskite-silicon tandem can currently achieve 29.8% module efficiency.[2] These tandem solar cells require perovskite subcells with a band gap of roughly 1.7 eV to complement the narrow band gap cell that is most often silicon. This is problematic, however, as most of the recent efficiency improvements in perovskite solar cells have been because of a narrowing of the band gap,[3] which make them less suitable for tandem application.

Currently, good perovskite solar cells with a band gap of around 1.7 eV typically have an open-circuit voltage (V_{oc}) of roughly 1.2 V,[4–7] with some reaching as high as 1.28 V.[8] While more realistic quantification exists,[9] the difference between the radiative limit for V_{oc} and measured V_{oc} is indicative of the room for improvement. For a 1.7 eV band gap, the radiative limit for V_{oc} is around 1.43 V, depending on the exact assumptions used to derive it.[10] This means that in typical cells, we have a few tenths of a Volt left to improve.

Wide band gap ($\gtrapprox$ 1.7 eV) perovskite cells suffered from phase segregation at first, where narrow band gap phases effectively acted as recombination centres. It has been shown however that halide segregation is responsible for a smaller part of the V_{oc} loss than electronic quality of the perovskite cells.[6] It is therefore of paramount importance to understand all the factors at play at the perovskite transport layer (TL) interface.

It is widely accepted that perovskite transport layer interfaces are the main culprit of V_{oc} losses because of the presence of trap assisted recombination.[6,11–14] In case of a large excess of one carrier type, as is typically the case at perovskite-TL interfaces, the Shockley-Read-Hall recombination rate is determined by the minority capture rate. This means that the minority carrier density, capture coefficient, and trap density become the determinant of the interfacial recombination rate.[15]

Surface passivation, typically by interlayers, can be employed to decrease the number of recombination centres at the perovskite transport layer interface.[12–14,16,17] Thin layers of passivating agents are deposited at the perovskite / transport-layer interface. Even though these layers might be insulating, by keeping them very thin, they can increase rather than decrease the fill-factor.

Interlayers can, however, decrease recombination even without passivating recombination centres by inducing band bending to repel minority carriers from the interface.[18]

To reduce the amount of charge carriers available for recombination at the interfaces, a few different strategies can be employed. First, a built-in voltage can contribute to extracting carriers to the right transport layer. Because of their n-i-p (or p-i-n) configuration, perovskite solar cells limit surface recombination at the metal contacts by repelling minority carriers with transport layers. This means that perovskite solar cells can even operate reasonably well with an electric field working against charge extraction in the perovskite.[19] An electric field aiding charge extraction is very beneficial to cell performance, however. This electric field can be achieved by doping the transport layers or by a difference in work functions between the two metal electrodes.[19,20] The last effect can be undercut however by the low dielectric constant or conductivity of typical transport layers, meaning most of the potential will drop over the transport layers instead of the perovskite.[21]

Additionally, imbalance between perovskite and transport layer (TL) properties can play a role in repelling or attracting minority carriers to the perovskite/TL interface. Typically, transport layers for PSCs are organic. Because of this, there is a large dielectric mismatch that can also cause extra recombination by accumulation of minority carriers near the interface.[22] While well aligned bands between perovskite and transport layer might seem preferable, a small extraction barrier can actually increase solar cell performance as it pushes minority carriers away from the interface.[23–25] Despite the efforts to reduce the number of interface traps, it is improbable that they can be completely prevented. It remains unclear how to optimize the electrical properties of the device stack, given that interfaces likely remain defective.

Here, we show design rules to optimize the open-circuit voltage of wide band gap perovskite solar cells. We implement a detailed description of interfacial recombination in SIMsalabim, an open-source device modelling software. A reference device is introduced that performs like a typical wide band gap perovskite solar cell. This reference device is then used to determine the effects of interface traps, band alignment, ions, and transport properties on the open-circuit voltage.

A large number of devices are simulated with random combinations of device parameters to look for trends in the open-circuit voltage. The total recombination rate in a cell determines the open-circuit voltage. Often, a reduction of the number of interface traps is attempted to reduce recombination, but this can be experimentally challenging. We find that reducing the minority carrier density in the perovskite at the transport layer interface suppresses recombination in equal measure. While band alignment is often exclusively considered, we find that the effective density of states in combination with band alignment determines the minority carrier density at the interface. We find that high open-circuit voltages are possible despite a significant density of interfacial defects.

3.2 Results

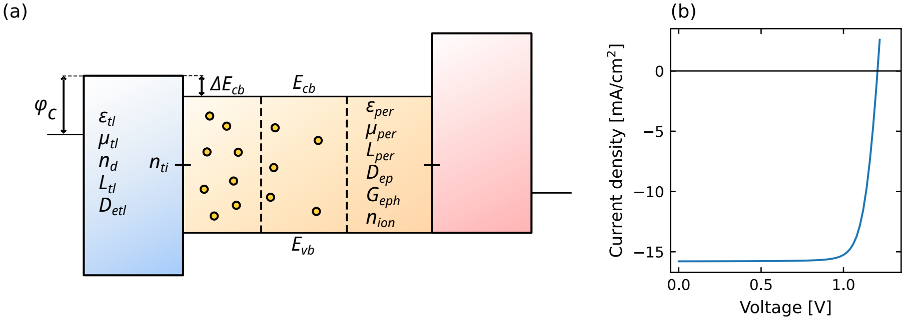

Figure 3.1: a) Schematic band diagram illustrating simulation parameters and where they take effect. Parameters are varied in the left transport layer (table C.3), while those in the right transport layer are chosen such that the left transport layer is limiting performance (table C.2). b) Current-voltage characteristic of our reference wide band gap perovskite solar cell. The device parameters used are in table C.1.

To investigate wide band gap perovskite solar cells, we will use SIMsalabim, an open-source simulation software for drift-diffusion simulations.[26] The physical model we use to represent these solar cells includes: mobile ions, interfacial recombination (at transport layer interfaces and grain boundaries), effective density of states (N_c), energetic alignment, dielectric contrast, absorption profiles, and dopants. Mobile ions are assumed to stay in the perovskite layer except in figures 3.2a and 3.4, where the mobile ions are allowed in the transport layers at random in half of the simulations. While in a regular perovskite solar cell reflection from the back electrode is quite relevant to the absorption profile, we neglect this effect for the wide band gap perovskites, which will be used mostly in a tandem configuration. The absorption profile is therefore assumed to be exponential, based on the absorption coefficient of a typical perovskite.[27]

Figure 3.1a shows a schematic band diagram of the device used in our simulations, with the most important parameters used indicated in the figure at the location where they take effect. In our simulations we include the effect of varying dielectric constant over the device, the effective density of states in the transport layer ($N_{\mathrm{c-tl}}$), band-alignment, transport layer (TL) doping, TL-mobility, TL-thickness, mobile ion density, ion placement in TLs, and interfacial trap density. In line plots in this section, the generation profile is exponential starting from the left side of the device in figure 3.1a. In the scatter plots, an absorption profile that is exponential starting from either electrode or a uniform absorption profile is picked at random. This is done to simulate the two edge cases for generation profiles to exclude any possible impact the detailed shape of the generation profile might have.

Because interfacial recombination is limiting to performance in most perovskite solar cells, it is imperative to model it accurately. To correctly describe the physics, we developed an advanced description of trap-assisted recombination for interface traps. We re-derive the Shockley-Read-Hall recombination expression for interface traps, which can capture from and emit to the conduction and valence band at either side of the interface. The derivation can be found in chapter 2. Furthermore, the interface charge of traps is considered depending on the type of trap. As was discussed in chapter 2 (Figure 2.3), a simpler expression for interface trapping, such as the original Shockley-Read-Hall expression, is insufficient. The large discontinuities of charge carriers densities at the interface that are dependent on input parameters and applied voltage mean that it is not clear in advance which rates should the recombination expression if only two trapping and detrapping rates are used. Taking rates from either side of the interface into account solves this problem. The difference is illustrated in figure 2.3 with an effective density of states offset, but the difference can be obtained through other parameters as well.

As discussed previously, a good wide band gap perovskite solar cell currently has an V_{oc} of roughly 1.2 V and a fill factor (FF) of 0.8.[4–7] The short circuit current (J_{sc}) sits at roughly 15-16 mA/cm^{-2},[4–7] but is not considered for optimization in this work. As a reference point for our investigation, we introduce a device that resembles such a typical wide band gap perovskite solar cell. Device parameters are chosen such that they are close to those of real devices and yield similar performance. Using the parameters shown in table C.1, we get the simulated JV-curve in figure 3.1b, which has a J_{sc} of 15.8 mA/cm^{-2}, a FF of 0.81, and an V_{oc} of 1.21 V.

Figure 3.2a shows the reference perovskite solar cell from figure 3.1b where properties of the left TL, left contact, perovskite, and TL/perovsite interface were varied. Properties for the right transport layer and electrode are kept constant, while those on the left side are varied over a wide range indicated in table C.3. The parameters in the right transport layer are chosen such that they are not limiting for device performance and are shown in table C.2. The results are

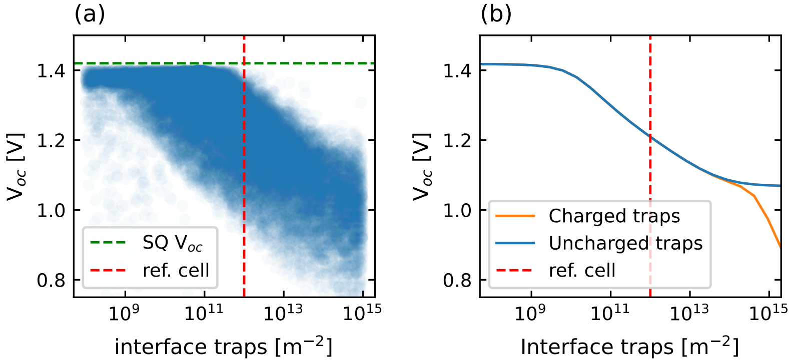

Figure 3.2: a) We vary relevant solar cell properties from our reference cell (red dashed line), except for those in the right TL and right contact. The parameter ranges are indicated in table C.3. b) The dependence of V_{oc} on interface trap density at for charged traps and uncharged traps. Charged traps are traps that are either negatively charged when willed with an electron (acceptor type) or positively charged when empty, or not filled with an electron (donor type). Uncharged traps are a limit of low trap density but high capture coefficients, which means that these traps do not contribute to space charge, but do act as recombination centres.

plotted versus the trap density at the left TL/perovskite interface.

Figure 3.2a shows that there is a broad trend showing that fewer traps generally mean higher V_{oc}. There is, however, a wide range of possible values for V_{oc} for any trap density. This is nicely illustrated when looking at the resulting V_{oc} values at the trap density for the reference device. We see that for the reference device introduced in figure 3.1b—that depending on other device parameters—the same trap density can yield a V_{oc} anywhere between 0.9 and 1.4 V.

In experiments, it is often difficult to isolate the changing of one parameter, such as interface trap density. This means that depending on other parameters that are changed along with trap density, a higher trap density could show a higher V_{oc}. Experimentally, simply reducing the number of traps regardless of other characteristics is therefore not an effective strategy for attaining a high V_{oc}.

Figure 3.2b shows that when all other parameters are kept constant, we do indeed get the expected result. Namely, starting from the trap density of the reference cell, higher trap density decreases V_{oc} and lower trap density decreases

V_{oc}. In figure 3.2b, three different interface trap types are considered, namely donor, acceptor, and neutral type traps. Due to the device symmetry, donor and acceptor traps yield the same result. We will therefore call these charged traps. Here, a neutral trap is an unphysical type of trap that is both neutral when empty and full. This trap type is included because it can differentiate the effect of traps contributing as recombination centres and traps contributing to space charge.

In Shockley-Read-Hall recombination, the trap density and capture coefficient only appear as a product, which is a recombination velocity as it has unit m/s.[15] If the charge of the traps does not play a role, the recombination velocity can uniquely determine recombination and therefore V_{oc} in our simulations. Since the simulations are performed in steady-state, we can then disentangle the effect from recombination and charge of the trap.

We see in figure 3.2b that at low trap densities, the charge of the trap does not play a role as the neutral type trap gives the same V_{oc} as the charged traps. At trap densities above 10^{14} m^2 however, we see that charged traps have significantly lower V_{oc} than uncharged traps. This shows that interface traps can be considered just as recombination centres without charge for low to medium interface trap densities. The levelling off of the V_{oc} at high trap density for neutral traps can be explained by minority carrier depletion at the interface; if there are a negligible number of minority carriers at the interface at V_{oc}, recombination does not increase further upon addition of more traps. This teaches us that the charge of interface traps is unlikely to be relevant for cells that have an V_{oc} of 1.2 V, the state of the art.

We continue our investigation by looking at the effect of the effective density of states (N_c) on V_{oc}. The N_c is determined by an integral over the product of the Fermi-Dirac distribution and the density of states (DOS) of the material in question. For typical inorganic materials the DOS is parabolic, which means that this integral returns a constant, the N_c, times a Boltzmann factor.[28]

This same simplification does not hold however for organic materials, that typically have a Gaussian DOS.[29] The Gaussian DOS causes an increase in N_c, increasing it above the total integral of the Gaussian DOS when the (quasi-)Fermi level gets close to the lowest unoccupied molecular orbital (LUMO) level. This is the case in a good solar cell near V_{oc}.

In figure 3.3a, it seems very intuitive that the organic layer should have a higher charge carrier density. In our simulations, this effect is captured by the N_c, which is orders of magnitude higher for organic materials. To keep the charge carriers from accumulating in the organic layer, the LUMO level can be increased to compensate the increased $N_{\mathrm{c-tl}}$.

Figure 3.2 showed that despite a significant number of traps, achieving a

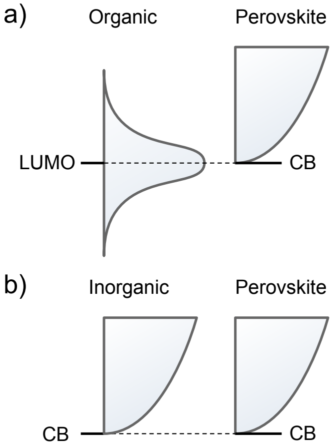

Figure 3.3: This figure shows schematically the difference between perfectly aligned bands for a) organic-TL/perovskite junctions, where the LUMO of the organic layer defines the centre of a Gaussian DOS and b) inorganic-TL/perovskite junctions, where both the inorganic-TL and the perovskite have a parabolic band defined by the minimum of the parabola.

good V_{oc} is possible. To investigate further what improvements can be made without reducing the number of traps, we will now select all solar cells from the dataset with trap densities of 3×10^{11} m^2 and upwards. This means that the trap density is close to that of the reference device introduced in figure 3.1 or above that. Figure 3.3 implies that to counteract higher N_c in the TL than the perovskite, the conduction band of the TL should be increased to counteract charge carrier accumulation. To test this premise, we take the same simulations as in figure 3.2, which include: mobile ion density, TL mobility, generation profile, TL/perovskite band offset, relative permittivity of the TL, TL thickness, TL doping density, electrode work function, interface trap density, and N_c of the TL. These simulations are then plotted against different parameters to show trends in V_{oc}.

The result is shown in figure 3.4 for the subset of devices with a trap density above 3×10^{11} m^2 as mentioned before. The points show all simulations, plotted against different variables in different sub-figures. In figures 3.4a and b, the data are plotted against the $N_{\mathrm{c-tl}}$ in the transport layer and the conduction band

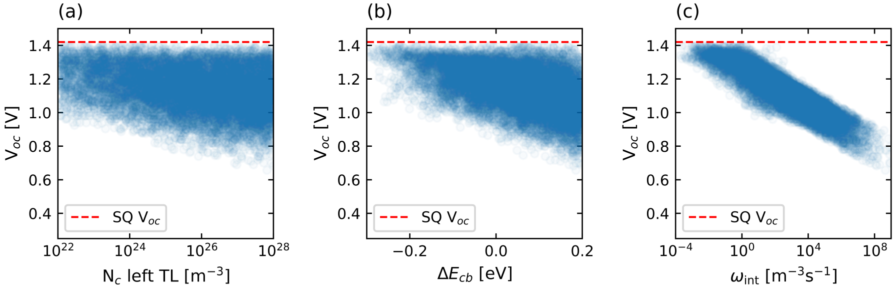

Figure 3.4: The dots show all simulations ran using parameters randomly drawn from the ranges indicated in table C.3. The Shockley-Queiser V_{oc} is plotted as a red dotted line. (a) All simulations plotted against the density of states in the transport layer. (b) All simulations plotted against the difference between the perovskite and transport layer conduction band. (c) All simulations plotted against parameter ω_{int}.

offset. While a trend is visible, neither band alignment nor the effective density of states provides a clear relation with V_{oc}. In figure 3.4c, the data are plotted against parameter

$$\omega_{\mathrm{int}} = C_{\mathrm{min}} N_{ti} \frac{N_{\mathrm{c-tl}}}{N_{\mathrm{c-per}}} \exp\left(\frac{\Delta E_c}{k_B T}\right), \tag{3.1}$$

where C_{min} is the minority carrier capture coefficient, N_{ti} is the interfacial trap density, and $N_{\mathrm{c-tl/per}}$ are the effective density of states of the transport layer and perovskite. This parameter approximates recombination at the interface by just the rate of minority carrier trapping $C_{\mathrm{min}} n_{\mathrm{min}} N_{ti}$, where n_{min} is the minority carrier density. As a gradient in N_c or band energy causes a step in the electrostatic potential at the interface, the minority carrier density changes accordingly. Typical transport layers are blocking for minority carriers however, so increased minority carrier density in the transport layer is not the cause for increased recombination.

Instead, the increased carrier density over the TL causes a larger potential drop in the TL, decreasing the potential drop over the perovskite layer. This large potential drop over the TL means there is less potential drop over the perovskite to keep minority carriers from the interface. This increase of minority carrier density near the interface increases recombination and reduces V_{oc}. With a given N_c offset between TL and active layer, this means that band alignment can be used to engineer a low carrier density near the interface, reducing recombination. While a high N_c, typical of organic transport layers, can still result in a high V_{oc}, this can happen if and only if the high N_c is compensated with a TL conduction band that lies higher than the perovskite conduction band.

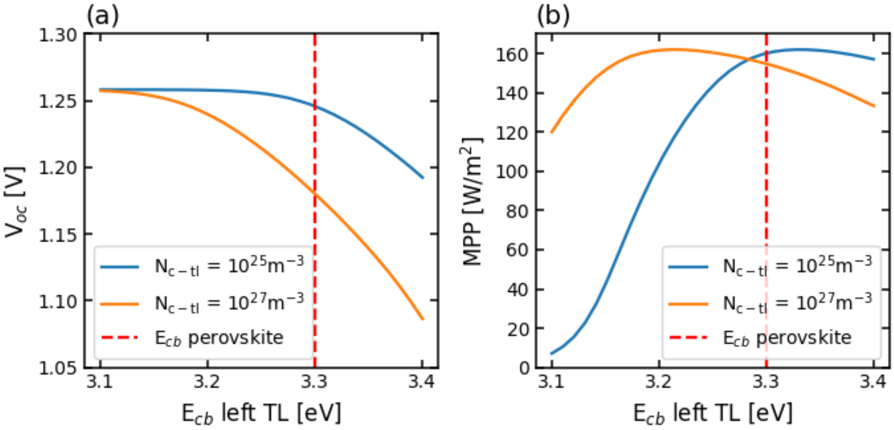

Figure 3.5: The effect of the conduction band energy (E_{cb}) on a) V_{oc} and b) the maximum power point (MPP) of our reference solar cell. $N_{\mathrm{c-tl}}$ is varied from being equal to that of the perovskite layer at 10^{25} m^{-3}, to higher by a factor of 100. The conduction band energy of the perovskite is shown as reference.

Figure 3.5 shows the effect of changing the conduction band level for different N_c in the reference device introduced in figure 3.1b. In figure 3.5a, shows that to attain maximum V_{oc}, the conduction band or LUMO of the transport layer should be equal to or higher than (depending on the N_c) the conduction band of the perovskite, which is set at 3.3 eV in the simulations. When the N_c of the perovskite equals that of the TL, optimal efficiency is obtained by aligning the TL and perovskite conduction bands. When the N_c of the TL increases, however, both the FF and V_{oc} increase when the conduction band of the TL is raised. This yields a MPP peak at a conduction band energy in the transport layer that is higher. This difference, ΔE_{cb}, is roughly 0.1 eV, for an N_c in the TL of 10^{27} m^{-3}, realistic for an organic layer with aligned bands. This shows that a higher N_c can be effectively counteracted by de-aligning the bands according to the parameter ω_{int} from equation 3.1, to reduce the carrier density in the transport layer.

3.3 Discussion

Suppose we start from a medium band gap device with optimal transport layers in terms of band alignment and N_c and then increase the band gap. This means that we will get alignment problems at one or both of the TL/perovskite interfaces that forces an increased carrier density in the transport layer, decreasing V_{oc}. To reduce interfacial recombination—and to enhance V_{oc}—one can focus on reducing the number of interface traps, their capture coefficients, or the minority carrier density near the transport layers.

Optimal band alignment in perovskite solar cells can be counter-intuitive. While it is known that we need different transport layers for wide band gap devices,[30] it is mostly suggested that aligned bands are best. This depends, however, on the effective density of states offset between perovskite and TL. Perfect energetic alignment of bands between perovskite and transport layer can yield worse performance than a transport layer that shows a small extraction barrier.[24] This effect is strongest for organic transport layers with a high density of states per unit volume and a Gaussian DOS.[29]

We show that the density of states offset between the perovskite layer and transport layer should also be considered when determining optimal band alignment. Since typical organic transport layers have a higher N_c than typical perovskite layers, it can be seen in figure 3.4 that an extraction barrier leads to higher V_{oc} at the same trap density. Interestingly, at realistic N_c of 10^{27} to 10^{28} m^{-3} coincides with a V_{oc} of 1.2 V or lower in our simulations.

Experimentally, it has been observed that lower disorder in the transport layer leads to a higher V_{oc}.[31–33] This is often attributed to better transport, but we show that the effect is more subtle than that; higher disorder means a wider Gaussian DOS, leading to more states closer to the Fermi-level yielding a higher N_c in the TL. This results in a reduced potential drop over the perovskite, leading to higher minority carrier density near the perovskite/TL interface and therefore a lower V_{oc}.

We show that the problem of reduces V_{oc} can be solved by reducing disorder, leading to a lower N_c, by increasing the band offset between ΔE_c, or reducing the density of traps at the interface as shown be equation 3.1. It should be highlighted that these effects are interchangeable in terms of V_{oc}, so the method that experimentally is the most feasible can be chosen for specific device configurations.

This agrees with what we illustrate in figure 3.3 and 3.5; More specifically, the width of this Gaussian is typically around 0.1 eV and reducing it from 0.136 eV to 0.090 eV increased V_{oc} by 0.09 V experimentally,[31] which is highly significant.

The dielectric constant might be expected to have a large influence on V_{oc} via a reduction of the built-in potential[34] or by trapping carriers near the interface.[22] We find however that while the dielectric mismatch can have a large effect on the FF via lowering of the built-in potential, its effect on V_{oc} is rather limited.

3.4 Conclusions

In conclusion, we introduce design rules for achieving optimal V_{oc} in perovskite solar cells. To this end, we provide a device model including a detailed description of interfacial recombination and use this to simulate a typical wide band gap perovskite solar cell. We then simulate a large set of solar cells including effects of ions, transport properties, band alignment, and traps. The total recombination rate in a device determines the open-circuit voltage, but is affected by different device parameters.

We introduce a parameter that combines the effect of interfacial trapping, N_c offset, and band alignment. The obvious strategy to reduce recombination and increase V_{oc}, is to reduce the number of interfacial traps, which is experimentally challenging. We show that recombination can be suppressed by reducing the minority carrier density near the interface through tuning of the band alignment and N_c offset at the interface. This means that band alignment is only half of the story and for achieving high V_{oc}, the N_c is of equal importance. Together, our results show that V_{oc} can get close to the Shockley-Queisser limit despite a significant number of interface traps.

Bibliography

[1] Z. Liu, L. Krückemeier, B. Krogmeier, B. Klingebiel, J. A. Márquez, S. Levcenko, S. Öz, S. Mathur, U. Rau, T. Unold, T. Kirchartz, *ACS Energy Letters* **2019**, *4*, 110–117.

[2] Best Research-Cell Efficiency Chart, **2022**, `https://www.nrel.gov/pv/cell-efficiency.html` (visited on 04/06/2022).

[3] L. Krückemeier, U. Rau, M. Stolterfoht, T. Kirchartz, *Advanced Energy Materials* **2020**, *10*, 1902573.

[4] S. Kavadiya, A. Onno, C. C. Boyd, X. Wang, A. Cetta, M. D. McGehee, Z. C. Holman, *Solar RRL* **2021**, *5*, 2100107.

[5] L. Gil-Escrig, C. Dreessen, F. Palazon, Z. Hawash, E. Moons, S. Albrecht, M. Sessolo, H. J. Bolink, *ACS Energy Letters* **2021**, *6*, PMID: 34568574, 827–836.

[6] S. Mahesh, J. M. Ball, R. D. J. Oliver, D. P. McMeekin, P. K. Nayak, M. B. Johnston, H. J. Snaith, *Energy Environ. Sci.* **2020**, *13*, 258–267.

[7] X. Liu, Z. Wu, X. Fu, L. Tang, J. Li, J. Gong, X. Xiao, *Nano Energy* **2021**, *86*, 106114.

[8] Z. Xu, X. Liu, S. Fu, J. Wang, J. Zhang, L. Huang, Z. Hu, Y. Zhu, *Applied Physics Letters* **2021**, *119*, 212101.

[9] L. Krückemeier, U. Rau, M. Stolterfoht, T. Kirchartz, *Advanced Energy Materials* **2020**, *10*, 1902573.

[10] W. Shockley, H. J. Queisser, *Journal of applied physics* **1961**, *32*, 510–519.

[11] T. S. Sherkar, C. Momblona, L. Gil-Escrig, H. J. Bolink, L. J. A. Koster, *Advanced Energy Materials* **2017**, *7*, 1602432.

[12] L. Krückemeier, B. Krogmeier, Z. Liu, U. Rau, T. Kirchartz, *Advanced Energy Materials* **2021**, *11*, 2003489.

[13] M. Stolterfoht, C. M. Wolff, J. A. Márquez, S. Zhang, C. J. Hages, D. Rothhardt, S. Albrecht, P. L. Burn, P. Meredith, T. Unold, D. Neher, *Nature Energy* **2018**, *3*, 847–854.

[14] Q. Jiang, Y. Zhao, X. Zhang, X. Yang, Y. Chen, Z. Chu, Q. Ye, X. Li, Z. Yin, J. You, *Nature Photonics* **2019**, *13*, 460–466.

[15] W. Shockley, W. T. Read, *Phys. Rev.* **1952**, *87*, 835–842.

[16] M. A. Mahmud, T. Duong, Y. Yin, H. T. Pham, D. Walter, J. Peng, Y. Wu, L. Li, H. Shen, N. Wu, N. Mozaffari, G. Andersson, K. R. Catchpole, K. J. Weber, T. P. White, *Advanced Functional Materials* **2020**, *30*, 1907962.

[17] M. Hadadian, J.-P. Correa-Baena, E. K. Goharshadi, A. Ummadisingu, J.-Y. Seo, J. Luo, S. Gholipour, S. M. Zakeeruddin, M. Saliba, A. Abate, M. Grätzel, A. Hagfeldt, *Advanced Materials* **2016**, *28*, 8681–8686.

[18] H. Wang, Y. Song, S. Dang, N. Jiang, J. Feng, W. Tian, Q. Dong, *Solar RRL* **2020**, *4*, 1900468.

[19] U. Würfel, A. Cuevas, P. Würfel, *IEEE Journal of Photovoltaics* **2015**, *5*, 461–469.

[20] J. Diekmann, P. Caprioglio, M. H. Futscher, V. M. Le Corre, S. Reichert, F. Jaiser, M. Arvind, L. P. Toro, E. Gutierrez-Partida, F. Peña-Camargo, C. Deibel, B. Ehrler, T. Unold, T. Kirchartz, D. Neher, M. Stolterfoht, *Solar RRL* **2021**, *5*, 2100219.

[21] N. E. Courtier, J. M. Cave, J. M. Foster, A. B. Walker, G. Richardson, *Energy Environ. Sci.* **2019**, *12*, 396–409.

[22] T. S. Sherkar, L. J. A. Koster, *ACS Applied Materials & Interfaces* **2015**, *7*, PMID: 25989847, 11881–11889.

[23] J. Dong, J. Shi, D. Li, Y. Luo, Q. Meng, *Applied Physics Letters* **2015**, *107*, 073507.

[24] C. Ding, Y. Zhang, F. Liu, Y. Kitabatake, S. Hayase, T. Toyoda, K. Yoshino, T. Minemoto, K. Katayama, Q. Shen, *Nano Energy* **2018**, *53*, 17–26.

[25] T. Yokoyama, Y. Nishitani, Y. Miyamoto, S. Kusumoto, R. Uchida, T. Matsui, K. Kawano, T. Sekiguchi, Y. Kaneko, *ACS Applied Materials & Interfaces* **2020**, *12*, PMID: 32427458, 27131–27139.

[26] M. Koopmans, V. M. L. Corre, L. J. A. Koster, *Journal of Open Source Software* **2022**, *7*, 3727.

[27] S. De Wolf, J. Holovsky, S.-J. Moon, P. Löper, B. Niesen, M. Ledinsky, F.-J. Haug, J.-H. Yum, C. Ballif, *The Journal of Physical Chemistry Letters* **2014**, *5*, PMID: 26270984, 1035–1039.

[28] C. Kittel, *Introduction to Solid State Physics*, 8th ed., Wiley, **2004**.

[29] H. Bässler, D. Kroh, F. Schauer, V. Nádaždy, A. Köhler, *Advanced Functional Materials* **2021**, *31*, 2007738.

[30] Y. Lin, B. Chen, F. Zhao, X. Zheng, Y. Deng, Y. Shao, Y. Fang, Y. Bai, C. Wang, J. Huang, *Advanced Materials* **2017**, *29*, 1700607.

[31] Y. Shao, Y. Yuan, J. Huang, *Nature Energy* **2016**, *1*, 15001.

[32] Y. Jiang, J. Wang, H. Zai, D. Ni, J. Wang, P. Xue, N. Li, B. Jia, H. Lu, Y. Zhang, et al., *Journal of the American Chemical Society* **2022**.

[33] G. Xu, R. Xue, S. J. Stuard, H. Ade, C. Zhang, J. Yao, Y. Li, Y. Li, *Advanced Materials* **2021**, *33*, 2006753.

[34] J.-Y. Huang, Y.-W. Yang, W.-H. Hsu, E.-W. Chang, M.-H. Chen, Y.-R. Wu, Influences of Dielectric Constant and Scan Rate to Hysteresis Effect in Perovskite Solar Cell: Simulation and Experimental Analyses, **2021**.

CHAPTER 4

Electrical Conductivity of Doped Organic Semiconductors Limited by Carrier-Carrier interactions

Abstract

High electrical conductivity is a prerequisite for advancing the performance of organic semiconductors for various applications and can be achieved through molecular doping. However, often the conductivity is enhanced only up to a certain optimum doping concentration, beyond which it decreases significantly. We combine analytical work and Monte Carlo simulations to demonstrate that carrier-carrier interactions can cause this conductivity decrease and reduce the maximum conductivity by orders of magnitude, possibly in a broad range of materials. Using Monte Carlo simulations we disentangle the effect of carrier-carrier interactions from carrier-dopant interactions. Coulomb potentials of ionized dopants are shown to decrease the conductivity, but barely influence the trend of conductivity versus doping concentration. We illustrate these findings using a doped fullerene derivative for which we can correctly estimate the carrier density at which the conductivity maximizes. We use grazing-incidence wide-angle X-ray scattering to show that the decrease of the conductivity cannot be explained by changes to the microstructure. We propose the reduction of carrier-carrier interactions as a strategy to unlock higher conductivity organic semiconductors.

4.1 Introduction

Electrical conductivity is a key parameter in many organic electronic devices. In organic light emitting diodes (OLEDs), organic solar cells (OSCs), and perovskite solar cells increasing conductivity by doping can reduce ohmic losses[1–3] and in thermoelectric generators the electrical conductivity is one of the key parameters.[4] Increasing the conductivity is most easily achieved by increasing the number of charge carriers by doping. Doping in organic semiconductors, however, is not a straightforward affair as the dopants need to react chemically with the host in order to yield free charges. The efficiency of this reaction varies and therefore the number of free charges per dopant molecule, or doping efficiency, also varies.[5]

Experimentally it is observed that the electrical conductivity of a large number of organic semiconductors shows a maximum: first the conductivity increases upon increasing doping density, but after the maximum the conductivity begins to decrease with increasing doping density. This behaviour is observed in both polymer and small molecule semiconductors doped with a wide variety of dopants[6–25] and can limit device performance in applications.[1–4] The carrier density at which the maximum in conductivity is observed ranges from 10^{18} to 10^{21} cm^{-3}.[6,14,18,20,22,26–29] The decrease in conductivity is often attributed to changes to the microstructure as a consequence of heavy doping. However, we have previously shown that even when using vapour doping, where there are no observable changes in the microstructure, the maximum in conductivity persists.[28]

Charge carrier transport in disordered organic semiconductors is usually described as a series of events where a charge carrier hops from one localized state to another.[30] The mobility of the charge carriers is proportional to the rate at which hopping events occur, which in turn is governed by the energetic and spatial distance of the hopping sites. The disordered nature of such disordered organic semiconductors manifests itself as a broad distribution of site energies and, when carrier density is low, a low intrinsic mobility of the charge carriers. Above a certain critical carrier concentration the inherently low conductivity can be increased by introducing more carriers to the system, as this facilitates the filling of the low-energy trap sites.[31–34] However, charge carriers are introduced by doping, which also introduces oppositely charged dopant ions as the number of (free and bound) charge carriers equals the number of reacted dopants. The release of charge carriers is facilitated by the energetic disorder. However, the dopant Coulomb potentials trap most mobile charge carriers to nearest or next nearest neighbour hopping sites.[35–37] The transport phenomena in doped disordered organic semiconductors are therefore typically explained on the basis of the interactions between dopant ions and mobile charge carriers.

Arkhipov et al.[38,39] introduced a model in which the Coulombic traps created by the dopant ions limit the charge carrier mobility at low-to-moderate doping concentrations while at high doping concentrations the overlap of the traps smoothens the potential landscape and increases the mobility.[38,39] This was experimentally confirmed for a large number of doped organic systems where the conductivity at low doping density appears to be limited by carrier-dopant interactions, while at higher dopant loading the dependence of conductivity on carrier-dopant interactions diminishes.[40] The low energy tail of density-of-states was proposed to broaden due to the increased energetic disorder induced by the dopant ions. The behaviour predicted by the Arkhipov model is observed in a number of kinetic Monte Carlo simulations[35,41] and it appears to be applicable for low to moderate doping densities. The experimentally observed conductivity maximum, however, would contradict this model: increasing the doping density would lead to an increasingly smooth potential landscape, resulting in an upward trend in conductivity.[38,39] This indicates it is unlikely that dopant-carrier interactions could cause this maximum in conductivity.

While dopant-carrier interactions are indeed recognized as an important factor, the effect of carrier-carrier interactions has received less attention. This is mainly because their repulsive interaction introduces no traps or barriers that could reduce charge carrier mobility[38] or because the carrier density is negligibly small.[41] Contrary to these findings, Liu et al. have shown by using kinetic Monte Carlo (KMC) simulations that carrier-carrier interactions in pristine, undoped organic semiconductors can limit the mobility at carrier densities above 10^{18} cm^{-3}.[42] Moreover, in disordered inorganic semiconductors, carrier-carrier interactions result in the development of a soft gap in the density-of-states at the Fermi level.[43,44] This is a result of the requirement that for a system in ground state, any electron transfer must increase the energy of the system. This so-called Coulomb gap was first derived by Efros and Shklovskii (ES)[43] and can act as a fingerprint for the relevance of carrier-carrier interactions.

Until now, it remains unclear what governs the transport in highly doped disordered organic semiconductors. At high carrier density, the charge carrier mobility could increase because of overlapping dopant potentials,[38,39] or it could decrease because of carrier-carrier interactions.[42] It is therefore important to consider both dopant-carrier and carrier-carrier interactions in order to establish a complete description of the charge transport process in highly doped organic semiconductors.

Here we address and elucidate the effect of morphology, dopant-carrier interactions, and carrier-carrier interactions on the conductivity of doped organic semiconductors. We first discuss the occurrence of a maximum in conductivity in doped organic semiconductors based on the literature and our previous work. To assess the role of morphology, we use GIWAXS on a doped fullerene derivative and find that it cannot explain the decrease in conductivity at high doping. We then use ES theory on carrier-carrier interactions to predict the carrier density at which the maximum of conductivity occurs. Finally, we show KMC simulations exhibiting a maximum in conductivity at a charge carrier density that corresponds to that observed experimentally. The maximum is observed both in the presence and absence of dopants. Overall, we show that carrier-carrier interactions lower the conductivity by orders of magnitude at high doping densities and therefore propose the suppression of carrier-carrier interactions as a key strategy for creating higher conductivity organic semiconductors.

4.2 Results

It has been observed in many host and dopant combinations that the conductivity maximizes and then decreases with increasing doping concentration.[6–25] This decrease at high doping concentrations is often attributed to changes in morphology.[24,45] We previously conducted conductivity measurements on thin films of the fullerene derivative PTEG-1 doped with molecular dopant n-DMBI (see Fig. 4.1a). Fig. 4.1b shows the conductivity for varying molar doping concentration of PTEG-1 doped with n-DMBI as reported.[18] As the fraction of dopant in the system was increased, the conductivity increased, peaked, and then decreased at high doping concentrations.

To check whether changes to the morphology are a likely cause of the conductivity decrease at high doping densities, we performed GIWAXS measurements on three PTEG-1 samples with different doping concentrations of n-DMBI. The measurements were performed on a pristine PTEG-1 sample, a 10 weight percent doped sample, and a 15 weight percent doped sample. These densities were chosen because previous measurements in Fig. 4.1b have shown that 10 weight percent doping yields the maximum conductivity, while at 15 weight percent doping the conductivity starts to decrease. If the maximum in conductivity is caused by a deteriorating microstructure upon adding too many dopants, there should be significant microstructural differences between the two doped samples.

Figures 4.1c and 4.1d show that at least for PTEG-1 doped with n-DMBI, this is unlikely to be the case. The morphology changed upon doping the pristine PTEG-1 system, but the morphology for 15% doping concentration was very similar to that of the 10% doping concentration sample. This means that although there are microstructural changes in the film upon doping, the changes between

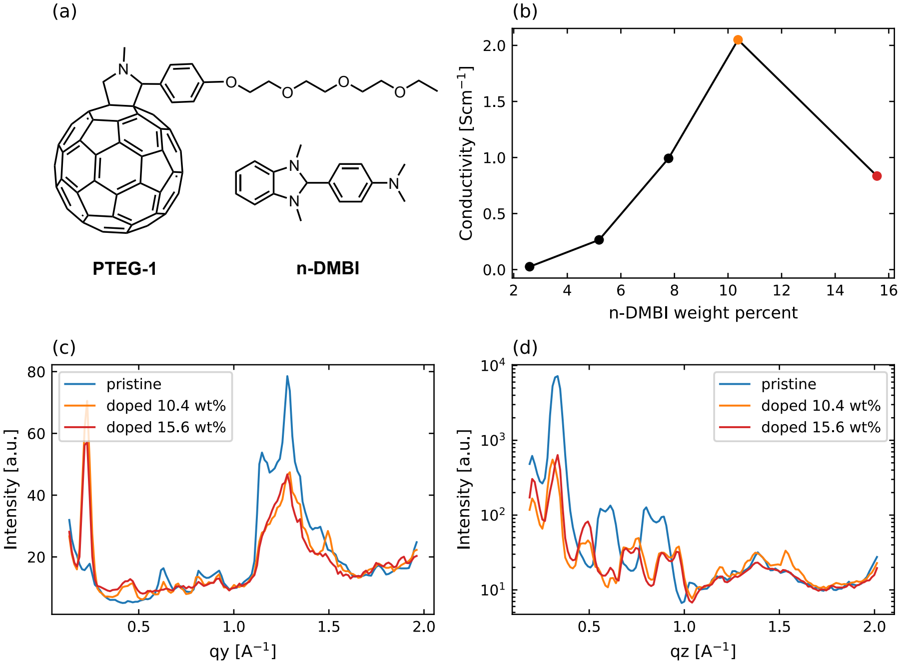

Figure 4.1: (a) The host, PTEG-1, and dopant, n-DMBI, used in the other sub-figures. (b) Conductivity of thin films of PTEG-1 doped with varying amounts of n-DMBI. (c,d) Line scans of GIWAXS measurements performed on PTEG-1 samples doped to varying weight percentages with n-DMBI.

different doping levels are small and cannot explain the decrease in conductivity for these samples. This indicates that in this system, a different mechanism is likely causing the decrease in conductivity at high doping density. Having shown that morphology is unlikely to cause the conductivity maximum in our system, we look at dopant-carrier interactions and the less discussed carrier-carrier interactions as alternative possible explanations for the conductivity maximum.

We first address the carrier-carrier interactions analytically, answering the question: at which doping density can we expect to see the effects of carrier-carrier interactions? Charge transport in an intrinsic organic semiconductor is often described as a series of hopping events between localized states that follow a Gaussian distribution in energy with a standard deviation σ of 75-100 meV.[30,46,47] The DOS in the absence of Coulomb interactions is given by[30]

$$g_0(\epsilon) = \frac{1}{a^3\sqrt{2\pi\sigma^2}} \exp\left(-\frac{\epsilon}{2\sigma^2}\right), \tag{4.1}$$

where a is the lattice spacing. To provide an estimate for the onset of carrier-carrier interactions, we turn to the ES theory of the Coulomb gap. The width Δ of the Coulomb gap is given by[48]

$$\Delta = \frac{q^3\sqrt{g_0^F}}{(4\pi\kappa\varepsilon_0)^{3/2}}, \tag{4.2}$$

where g_0^F is the DOS at the Fermi level in the absence of Coulomb carrier-carrier interactions, κ is the relative dielectric constant, ε_0 is the vacuum permittivity, and q is the unit charge. The problem is then reduced to finding g_0^F such that Δ is equal to the relevant energy scale. As the doping level increases, the Fermi level shifts and g_0^F will increase, and so will the Coulomb gap energy Δ. In disordered organic semiconductors, the two relevant energies are the thermal energy k_BT and the energetic disorder of the DOS, σ. If the predicted Coulomb gap is of the order of the thermal energy k_BT or larger, then we expect Coulomb carrier-carrier interactions to start to affect the conductivity. We expect carrier-carrier interactions to dominate when Δ becomes larger than the energetic disorder in the system. Assuming a relative dielectric constant $\kappa = 4$, Equations (4.2) and (4.1) imply that carrier-carrier interactions will become noticeable ($\Delta = k_BT$) at a carrier density $n_c \approx 2 \times 10^{18}$ cm^{-3}. Carrier-carrier interactions will dominate ($\Delta = \sigma$) and likely limit the electrical conductivity at a carrier density of 1×10^{19} cm^{-3}. In the next section, we will compare these predicted critical carrier densities with KMC simulations.

Now that we have analytically shown that carrier-carrier interactions are expected to affect disordered organic semiconductors with localized charge carriers,

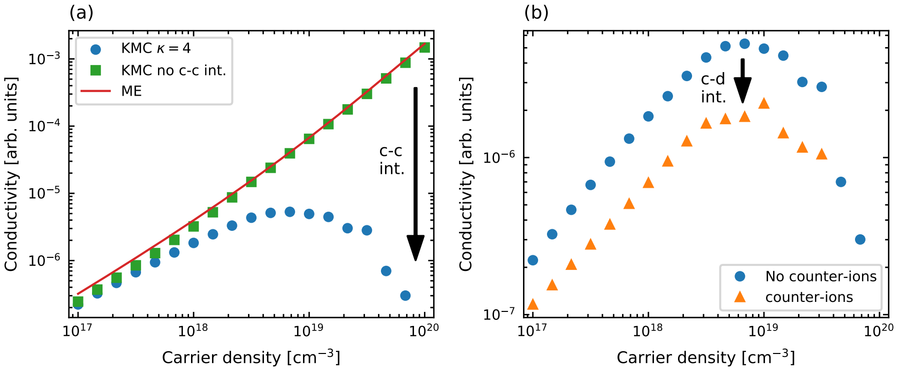

Figure 4.2: (a) KMC and ME simulations without counter-ions using the same parameters. KMC simulations (circles) at dielectric constants of 4 and at an arbitrarily large dielectric constant (squares) to eliminate carrier-carrier interactions. A dielectric constant of 1000 was used for this purpose. The arrow indicates the effect of carrier-carrier interactions, which becomes stronger as the carrier density increases. Master equation simulations (line) with the same input parameters as the KMC simulations are also shown. (b) KMC simulations with (triangles) and without (circles) Coulomb potentials of ionized dopants in equal number as free charge carriers.

we can investigate conductivity in these systems using KMC simulations. Using KMC simulations, the effects of carrier-carrier interactions and dopant-carrier interactions can be disentangled. The effects of dopant counter-ions resulting from dopant-carrier (d-c) interactions and carrier-carrier (c-c) interactions are investigated by selectively turning them on and off in the simulations. We treat three cases: (1) no c-c and no d-c interactions, (2) c-c but no d-c interactions, (3) and c-c and d-c interactions. The resulting conductivity is investigated alongside the DOS.

In KMC simulations it is notoriously hard to get rid of dependence of simulated trends on simulation parameters such as number of simulated hops, or the simulated box size. In fig. A.4 we show that if not enough hops are simulated in the KMC simulations, the trend can change drastically compared to the properly equilibrated result. The way we check for equilibrium is by checking the temperature of the charge carriers. When a simulation is initialized, the charge carriers start on sites that are the lowest in energy without accounting for carrier-carrier interactions. This means the carriers are in an excited configuration once we introduce carrier-carrier interactions, and we need to let the charge carriers hop until they reach equilibrium; otherwise we risk overestimating the conductivity. We confirmed equilibration by fitting the o-DOS to the DOS times the Fermi-Dirac function. When the temperature of the charge carriers is higher than that of the lattice, equilibrium has not yet been reached, but when the resulting temperature is within 15% of our settings, we consider the simulation equilibrated. Because of the difficulty reaching an equilibrated state, we also validate the KMC simulations against both SE theory on electron-electron interactions from the previous section and master equation (ME) simulations. Although the ME method does not include c-c or d-c interactions, at low charge carrier density the effect of c-c interactions is negligible compared to the effect of the intrinsic disorder. Therefore, two of the three sets of KMC simulations can be at least partly validated using ME simulations.

Fig. 4.2 shows the conductivity as a function of carrier density obtained from the KMC simulations and the ME simulations. Fig. 4.2a shows that the effect of carrier-carrier interactions is very strong: at a carrier density of 10^{19} cm^{-3} carrier-carrier interactions reduce the conductivity by roughly one order of magnitude, while increasing the carrier density to 10^{20} cm^{-3} results in a conductivity reduction by three orders of magnitude. In Fig. 4.2b dopant counter-ion potentials are added to the simulations. We see that although the simulations that include dopant counter-ions show lower conductivity, as expected from the Arkhipov model, the trend is the same and the maximum in conductivity remains at the same charge carrier density of $\sim 10^{19}$ cm^{-3}. This shows that carrier-carrier interactions can cause the conductivity to peak at experimentally relevant doping

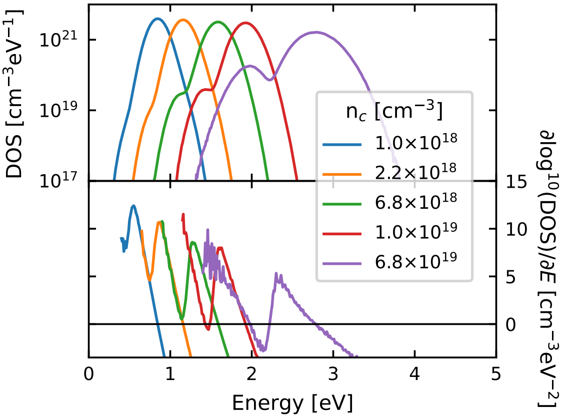

Figure 4.3: (Top) DOS as calculated using KMC simulations for increasing charge carrier densities (from left to right) in absence of counter-ions. Increasing carrier density changes the shape of the DOS from a single Gaussian to an apparent superposition of two Gaussians. (Bottom) First derivative of the DOS with respect to energy, showing the first appearance of a valley in the DOS between 6.8×10^{18} and 1.0×10^{19} cm^{-3}.

densities in doped organic semiconductors. As indicated by the arrows in Fig. 4.2, c-d interactions effectively shift the carrier density versus conductivity curve down to lower conductivity, meaning their effect is not strongly dependent on charge carrier density. The effect of c-c interactions only appears at higher densities, but dominates the high charge carrier density conductivity behaviour.

The DOS of the simulations without counter-ions are collated in Fig. 4.3 to better show the difference between the DOS at different charge carrier densities. It can be readily seen that the DOS becomes wider with increasing charge carrier density. Also, a shoulder appears at the lower energy side of the DOS and becomes prominent at a carrier density of around 2.2×10^{18} cm^{-3}. It should be noted that this shoulder is purely a manifestation of carrier-carrier interaction, as there are no counter-ions present in this simulation. Running the same simulation with dopant counter-ions yields roughly the same result, as can be seen in Fig. A.2. When the charge carrier density reaches 10^{19} cm^{-3} a local minimum, i.e. Coulomb pseudo-gap, in the DOS can be observed. This pseudo-gap appears regardless of the presence of ionized dopants (see Fig. A.1).

Finally, we investigate the role of dopants in more detail. In the KMC

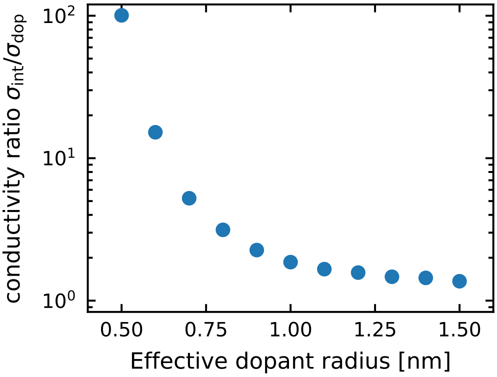

Figure 4.4: At a carrier density of 10^{17} cm^{-3} the conductivity ratio between simulations without dopant potentials (σ_{int}) and simulations with dopant potentials (σ_{dop}).

simulations, a dopant is placed on a lattice point, but the Coulomb potential of the ionized dopant is calculated with an effective dopant radius added (r_{dop}) to the lattice distance. The r_{dop} determines the maximum Coulomb interaction strength possible between a mobile charge carrier and a dopant as the minimal possible distance between them is the r_{dop}. In Fig. 4.2b an effective dopant radius of 1 nm was used. When the effective dopant radius is 1 nm, the maximum interaction energy is 0.36 eV. This value is chosen as it does not exceed the exciton binding energy of ~0.4 eV.[49] A stronger interaction would render the charge carrier effectively bound. The impact of the r_{dop} on the electrical conductivity is shown in Fig. 4.4, illustrating that the dopant ions do affect the conductivity depending on the r_{dop}. However, the impact of carrier-carrier interactions at high charge carrier density (see Fig. 4.2a) appears to be larger than that of the dopants even if a low r_{dop} is assumed.

4.3 Discussion

We find a conductivity maximum using KMC simulations that include carrier-carrier and carrier-dopant interactions (see Fig. 4.2). We find that the maximum conductivity is obtained at the same charge carrier density as in previous experimental conductivity measurements for PTEG-1 doped with n-DMBI (see

Fig. 4.1b). Our new experimental evidence (Fig. 4.1c and d) suggests that there are no significant microstructural changes upon doping while the KMC simulations reproduce the maximum without accounting for morphology. This leads us to a conclusion that morphology changes are an unlikely explanation for the conductivity maximum in our experiments. We also observe that the Coulomb potentials of the ionized dopants are not the cause for the maximum in conductivity (Fig. 4.2) as the maximum is present in the conductivity regardless of whether the dopant ions are implemented or not. This means we can exclude both typical explanations, i.e. morphology and dopants, for the maximum in conductivity.

A remaining explanation for the conductivity maximum is the carrier-carrier interactions. Experimentally, the maximum in conductivity is observed in various systems and the corresponding carrier density ranges from the order of 10^{18} to 10^{21} cm^{-3}.[6,14,18,20,22,26–29] Our analytical results using Eq. 4.2, that include both mobile charge carriers and dopants, predict that carrier-carrier interactions start to dominate when the Coulomb gap width is larger than the energetic disorder, which occurs at a carrier density in the order of 10^{19}cm^{-3}. These effects are fundemental to the interaction of charge carriers and are as generally applicable as the effect of Coulomb attraction between dopant and mobile charge carriers. Our KMC simulations show that even in the absence of dopant ions a maximum in conductivity is observed at the same carrier density of 10^{19}cm^{-3}. Based on the combination of methods used here, we propose that the conductivity maximum is primarily a result of the carrier-carrier interactions. Considering the wide applicability of the analytical work and the range of different materials that could be simulated using similar KMC simulation settings, this is likely to be the case in many different disordered organic materials.

It should be noted that the carrier density at which the conductivity maximum occurs is influenced by the dielectric constant as can be seen in Eq. 4.2. When the dielectric constant increases, the charges are more screened and therefore their interaction will be weaker. As a result, the conductivity maximum is expected to shift to higher charge carrier densities. The dielectric constants of disordered organic semiconductors vary considerably. For example, the dielectric constant of PTEG-1 is 5.7 while that of conjugated polymers is typically lower.[50] In our KMC simulations we choose a relative dielectric constant of 4. A second factor affecting the interaction of charge carriers is their localization. Both the analytical work and the KMC simulations assume highly localized charges, but in many molecular semiconductors charge carriers can be quite delocalized. This can therefore provide an explanation for why in some polymers the carrier density at the maximum conductivity is higher than that calculated in the KMC simulations (Fig. 4.2).[6,22,29] Improved screening of charges and increased delocalisation of charge carriers could both serve as strategies to reduce unwanted carrier-carrier interaction.

The negative effect of the carrier-carrier interactions on the conductivity can be linked to the development of a Coulomb pseudo-gap, which forms at high carrier densities regardless of the presence or absence of dopant counter-ions (Fig. 4.3). This indicates that this feature is a sole consequence of the carrier-carrier Coulomb interactions rather than a result of the dopant ions. At high carrier densities, this soft gap forms at the Fermi level as seen in Fig. 4.3 and, as a consequence, reduces the number of available hopping sites in the vicinity of the Fermi level. This means that the carriers are forced to hop to higher energy sites, which again reduces the rate of hopping as given by the Miller-Abrahams expression.[51] Such a modification of the DOS upon doping has been previously reported experimentally,[35] but the development of the low-energy shoulder was attributed to the impact of the dopant ions as described by Arkhipov.[39] However, we have observed that the broadening of DOS as a result of the dopant-dopant interactions in Fig. A.1 and as a result of carrier-carrier interactions in Fig. 4.3 is different than the DOS broadening as a result of carrier-dopant interactions as described in the Arkhipov model. Moreover, when the mobile charge carriers and dopants are included, the DOS is a superposition of two Gaussians rather than a Gaussian with an exponential tail, as expected by the Arkhipov model.

The reliability of the KMC simulations can be validated by considering that at low carrier density the ME and KMC simulations agree quantitatively (Fig. 4.2a). Moreover, the experimentally, analytically and numerically obtained critical carrier densities at which the conductivity reaches a maximum match very well. Also, the density of $\sim 10^{18}$ cm^{-3} at which the Coulomb pseudo-gap width equals $k_B T$ and is predicted to start influencing conductivity coincides with the carrier density found by Liu et al.[42]

In conclusion, we have shown that while the Coulomb potentials of the ionized dopants are not the cause for the maximum in conductivity, they still have a significant role in governing the conductivity of the system. As seen in Fig. 4.2b, the dopant ions lower the overall conductivity, meaning that attempts to shield the dopant potentials might advance the quest for higher conductivity materials. This observation is in agreement with experimental work where dopant ions were shielded by increasing the dopant radius.[6] However, the maximum achievable increase in conductivity upon removing the dopant ions from the system was limited to less than an order of magnitude when we assumed the depth of the Coulomb potential to be limited to the exciton binding energy. In contrast, decreasing the Coulomb interaction between mobile charge carriers (Fig. 4.2a) resulted in conductivity increase by more than three orders of magnitude. Considering this, reducing carrier-carrier interactions through reduced carrier localization or increased screening of charges could be the more effective one to designing higher conductivity materials.

4.4 Conclusions

We show using both Efros-Shklovskii theory and kinetic Monte Carlo simulations that a Coulomb pseudo-gap appears in the density of states at a charge carrier density of $\sim 10^{19}$ cm^{-3}. This coincides with the charge carrier density at which the maximum conductivity was previously reported for the fullerene derivative PTEG-1 doped to varying degrees with molecular dopant n-DMBI. This Coulomb pseudo-gap is a manifestation of carrier-carrier interactions and limits the conductivity regardless of the presence of dopant Coulomb potentials. We performed GIWAXS measurements on the doped PTEG-1 samples to show that the microstructure does not change significantly from the optimally doped samples to over-doped samples, where the conductivity is lower due to an excess of dopants as reported previously.

Due to the broad applicability of the analytical work and the KMC simulations, we expect carrier-carrier interactions to play an important role in a wide range of both n-type and p-type disordered organic semiconductors at charge carrier densities of $\sim 10^{19}$ cm^{-3} and above. We show that at high dopant loading eliminating carrier-carrier interactions can increase the conductivity by orders of magnitude, while reducing carrier-dopant interactions leads to a much smaller gain in conductivity. This means that reducing carrier-carrier interactions could be a key strategy to finding higher conductivity organic semiconductors.

Bibliography

[1] B. Lüssem, M. Riede, K. Leo, *Phys. Status Solidi A* **2013**, *210*, 9–43.

[2] I. Salzmann, G. Heimel, *J. Electron Spectros. Relat. Phenomena* **2015**, *204*, 208–222.

[3] V. M. Le Corre, M. Stolterfoht, L. Perdigón Toro, M. Feuerstein, C. Wolff, L. Gil-Escrig, H. J. Bolink, D. Neher, L. J. A. Koster, *ACS Appl. Energy Mater.* **2019**, *2*, 6280–6287.

[4] D.M. Rowe, *Thermoelectrics handbook*, Taylor & Francis, **2006**, p. 1008.

[5] I. Salzmann, G. Heimel, M. Oehzelt, S. Winkler, N. Koch, *Acc. Chem. Res.* **2016**, *49*, 370–378.

[6] T. J. Aubry, J. C. Axtell, V. M. Basile, K. J. Winchell, J. R. Lindemuth, T. M. Porter, J. Y. Liu, A. N. Alexandrova, C. P. Kubiak, S. H. Tolbert, A. M. Spokoyny, B. J. Schwartz, *Adv. Mater.* **2019**, *31*, 1–8.

[7] Q. Bao, X. Liu, S. Braun, F. Gao, M. Fahlman, *Adv. Mater. Interfaces* **2015**, *2*, 1–6.

[8] F. Deschler, D. Riedel, A. Deák, B. Ecker, E. Von Hauff, E. Da Como, *Synth. Met.* **2015**, *199*, 381–387.

[9] D. T. Duong, C. Wang, E. Antono, M. F. Toney, A. Salleo, *Org. Electron.* **2013**, *14*, 1330–1336.

[10] J. Euvrard, A. Revaux, P. A. Bayle, M. Bardet, D. Vuillaume, A. Kahn, *Org. Electron.* **2018**, *53*, 135–140.

[11] K. Harada, M. Sumino, C. Adachi, S. Tanaka, K. Miyazaki, *Appl. Phys. Lett.* **2010**, *96*, 3–6.

[12] D. Huang, H. Yao, Y. Cui, Y. Zou, F. Zhang, C. Wang, H. Shen, W. Jin, J. Zhu, Y. Diao, W. Xu, C. A. Di, D. Zhu, *J. Am. Chem. Soc.* **2017**, *139*, 13013–13023.

[13] S. Hwang, W. J. Potscavage, Y. S. Yang, I. S. Park, T. Matsushima, C. Adachi, *Phys. Chem. Chem. Phys.* **2016**, *18*, 29199–29207.

[14] D. Kiefer, A. Giovannitti, H. Sun, T. Biskup, A. Hofmann, M. Koopmans, C. Cendra, S. Weber, L. J. A. Koster, E. Olsson, J. Rivnay, S. Fabiano, I. McCulloch, C. Müller, *ACS Energy Lett.* **2018**, *3*, 278–285.

[15] C. Z. Li, C. C. Chueh, H. L. Yip, F. Ding, X. Li, A. K. Y. Jen, *Adv. Mater.* **2013**, *25*, 2457–2461.

[16] C. Z. Li, C. C. Chueh, F. Ding, H. L. Yip, P. W. Liang, X. Li, A. K. Jen, *Adv. Mater.* **2013**, *25*, 4425–4430.

[17] J. Li, C. W. Rochester, I. E. Jacobs, E. W. Aasen, S. Friedrich, P. Stroeve, A. J. Moulé, *Org. Electron.* **2016**, *33*, 23–31.

[18] J. Liu, L. Qiu, G. Portale, M. Koopmans, G. ten Brink, J. C. Hummelen, L. J. A. Koster, *Adv. Mater.* **2017**, *29*, DOI `10.1002/adma.201701641`.

[19] J. Liu, L. Qiu, G. Portale, S. Torabi, M. C. A. Stuart, X. Qiu, M. Koopmans, R. C. Chiechi, J. C. Hummelen, L. J. A. Koster, *Nano Energy* **2018**, *52*, 183–191.

[20] H. Méndez, G. Heimel, S. Winkler, J. Frisch, A. Opitz, K. Sauer, B. Wegner, M. Oehzelt, C. Röthel, S. Duhm, D. Többens, N. Koch, I. Salzmann, *Nat. Commun.* **2015**, *6*, DOI `10.1038/ncomms9560`.

[21] T. Menke, D. Ray, J. Meiss, K. Leo, M. Riede, *Appl. Phys. Lett.* **2012**, *100*, DOI `10.1063/1.3689778`.

[22] B. D. Paulsen, C. D. Frisbie, *J. Phys. Chem. C* **2012**, *116*, 3132–3141.

[23] H. Méndez, G. Heimel, A. Opitz, K. Sauer, P. Barkowski, M. Oehzelt, J. Soeda, T. Okamoto, J. Takeya, J.-B. Arlin, J.-Y. Balandier, Y. Geerts, N. Koch, I. Salzmann, *Angew. Chemie Int. Ed.* **2013**, *52*, 7751–7755.

[24] R. A. Schlitz, F. G. Brunetti, A. M. Glaudell, P. L. Miller, M. A. Brady, C. J. Takacs, C. J. Hawker, M. L. Chabinyc, *Adv. Mater.* **2014**, *26*, 2825–2830.

[25] D. T. Scholes, S. A. Hawks, P. Y. Yee, H. Wu, J. R. Lindemuth, S. H. Tolbert, B. J. Schwartz, *J. Phys. Chem. Lett.* **2015**, *6*, 4786–4793.

[26] J. Liu, G. Ye, B. van der Zee, J. Dong, X. Qiu, Y. Liu, G. Portale, R. C. Chiechi, L. J. A. Koster, *Adv. Mater.* **2018**, *30*, DOI `10.1002/adma.201804290`.

[27] J. Liu, B. van der Zee, R. Alessandri, S. Sami, J. Dong, M. I. Nugraha, A. J. Barker, S. Rousseva, L. Qiu, X. Qui, N. Klasen, R. C. Chiechi, D. Beran, M. Caironi, T. D. Anthopoulos, G. Portale, R. W. A. Havenith, S. J. Marrink, J. C. Hummelen, L. J. A. Koster, *Nat. Commun.*

[28] J. Liu, Y. Shi, J. Dong, M. I. Nugraha, X. Qiu, M. Su, R. C. Chiechi, D. Baran, G. Portale, X. Guo, L. J. A. Koster, *ACS Energy Lett.* **2019**, *4*, 1556–1564.

[29] D. Kiefer, R. Kroon, A. I. Hofmann, H. Sun, X. Liu, A. Giovannitti, D. Stegerer, A. Cano, J. Hynynen, L. Yu, Y. Zhang, D. Nai, T. F. Harrelson, M. Sommer, A. J. Moulé, M. Kemerink, S. R. Marder, I. McCulloch, M. Fahlman, S. Fabiano, C. Müller, *Nat. Mater.* **2019**, *18*, 149–155.

[30] H. Bässler, *Phys. Status Solidi* **1993**, *175*, 15–56.

[31] V. I. Arkhipov, P. Heremans, E. V. Emelianova, G. J. Adriaenssens, H. Bässler, *J. Phys. Condens. Matter* **2002**, *14*, 9899–9911.

[32] M. C. J. M. Vissenberg, M. Matters, *Phys. Rev. B* **1998**, *57*, 12964–12967.

[33] C. Tanase, E. J. Meijer, P. W. M. Blom, D. M. de Leeuw, *Phys. Rev. Lett.* **2003**, *91*, 216601.

[34] W. F. Pasveer, J. Cottaar, C. Tanase, R. Coehoorn, P. A. Bobbert, P. W. M. Blom, D. M. de Leeuw, M. A. J. Michels, *Phys. Rev. Lett.* **2005**, *94*, 206601.

[35] G. Zuo, H. Abdalla, M. Kemerink, *Phys. Rev. B* **2016**, *93*, 235203.

[36] A. Mityashin, Y. Olivier, T. Van Regemorter, C. Rolin, S. Verlaak, N. G. Martinelli, D. Beljonne, J. Cornil, J. Genoe, P. Heremans, *Adv. Mater.* **2012**, *24*, 1535–1539.

[37] M. L. Tietze, J. Benduhn, P. Pahner, B. Nell, M. Schwarze, H. Kleemann, M. Krammer, K. Zojer, K. Vandewal, K. Leo, *Nat. Commun.* **2018**, *9*, 1182.

[38] V. I. Arkhipov, E. V. Emelianova, P. Heremans, H. Bässler, *Phys. Rev. B* **2005**, *72*, 235202.

[39] V. I. Arkhipov, P. Heremans, E. V. Emelianova, H. Bässler, *Phys. Rev. B* **2005**, *71*, 045214.

[40] M. Schwarze, C. Gaul, R. Scholz, F. Bussolotti, A. Hofacker, K. S. Schellhammer, B. Nell, B. D. Naab, Z. Bao, D. Spoltore, K. Vandewal, J. Widmer, S. Kera, N. Ueno, F. Ortmann, K. Leo, *Nat. Mater.* **2019**, *18*, 242–248.

[41] A. Abate, D. R. Staff, D. J. Hollman, H. J. Snaith, A. B. Walker, *Phys. Chem. Chem. Phys.* **2014**, *16*, 1132–1138.

[42] F. Liu, H. van Eersel, B. Xu, J. G. E. Wilbers, M. P. de Jong, W. G. van der Wiel, P. A. Bobbert, R. Coehoorn, *Phys. Rev. B* **2017**, *96*, 205203.

[43] A. L. Efros, B. I. Shklovskii, *J. Phys. C Solid State Phys.* **1975**, *8*, L49.

[44] A. L. Efros, *J. Phys. C Solid State Phys.* **1976**, *9*, 2021–2030.

[45] K. Shi, F. Zhang, C. A. Di, T. W. Yan, Y. Zou, X. Zhou, D. Zhu, J. Y. Wang, J. Pei, *J. Am. Chem. Soc.* **2015**, *137*, 6979–6982.

[46] O. Tal, Y. Rosenwaks, Y. Preezant, N. Tessler, C. K. Chan, A. Kahn, *Phys. Rev. Lett.* **2005**, *95*, 256405.

[47] Y. Shen, K. Diest, M. H. Wong, B. R. Hsieh, D. H. Dunlap, G. G. Malliaras, *Phys. Rev. B* **2003**, *68*, 081204.

[48] B.I. Shklovskii; A.L. Efros, *Electronic Properties of Doped Semiconductors*, 1st ed., Springer-Verlag Berlin Heidelberg, **1984**, 60 & 237.

[49] S. Barth, H. Bässler, *Phys. Rev. Lett.* **1997**, *79*, 4445–4448.

[50] F. Jahani, S. Torabi, R. C. Chiechi, L. J. A. Koster, J. C. Hummelen, *Chem. Commun.* **2014**, *50*, 10645–10647.

[51] A. Miller, E. Abrahams, *Phys. Rev.* **1960**, *120*, 745–755.

CHAPTER 5

Carrier-Carrier Coulomb Interactions Reduce Power Factor in Organic Thermoelectrics

Abstract

Organic semiconductors are excellent candidates for low temperature thermoelectric generators. However, such thermoelectric applications require that the materials be doped and highly conductive. Here, we show how doping affects the Seebeck coefficient in organic semiconductors using kinetic Monte-Carlo simulations. Employing a hopping transport approach, we demonstrate that at high dopant loading, carrier-carrier interactions can reduce the Seebeck coefficient. This results in systems with intrinsic disorder, still following Heike's formula for thermopower at high dopant density. Reducing these carrier-carrier interactions results in an increased Seebeck coefficient and power factor. Specifically, a realistic reduction in carrier-carrier interactions can increase the power factor by more than a factor 15, increasing ZT above 1 for organic thermoelectrics.

5.1 Introduction

Organic thermoelectrics are starting to attract more attention because of their increasing performance and unique flexibility.[1–3] The performance of thermoelectric generators is characterised by the figure of merit $ZT = \sigma S^2 T/\kappa$, where σ is the electrical conductivity, S is the Seebeck coefficient, T is the temperature, and κ is the thermal conductivity.[4] In inorganic thermoelectrics it is possible to engineer κ, but in organic thermoelectric materials κ is generally so low that it is not considered for optimization.[5] Therefore, organic thermoelectric materials are generally characterised via their power factor (PF), which is $S^2\sigma$. The primary method of increasing the PF is through doping, as this increases σ.

While doping increases σ, it also strongly affects the energetic landscape because of strong Coulombic interactions between the introduced charges. Charge carriers are known to get trapped by Coulomb traps created by dopant ions.[6,7] The effect of these Coulomb traps is strongest at low charge carrier densities, because at higher densities the dopant Coulomb potentials start to overlap. This reduces the potential barrier for removing a charge carrier from a dopant.[6,7] Multiple ways have been shown to reduce the effect of these carrier-dopant (c-d) interactions. It is possible to physically increase the distance between the dopant ion and the host molecules to reduce Coulombic interaction by adding molecular spacers in-between the host and dopant.[8,9] Another way to influence the Coulomb attraction between host and dopant is by allowing charge to delocalise on the dopant, where larger molecules allow for more delocalisation and therefore lower Coulomb attraction between host and dopant.[8]

While c-d interactions become less relevant with increasing charge carrier density, the opposite is true for carrier-carrier interactions. We have recently shown, that under the assumption of hopping transport, the conductivity at typical electron densities for organic thermoelectrics is limited by c-c interactions.[10] Also, these c-c interactions rapidly increase in strength upon further increase of the charge carrier density.

Intrinsically, organic materials are generally considered to have a Gaussian distribution of hopping sites which resemble molecules or molecular segments, where the width of this Gaussian is determined by disorder in the material.[11] Up to medium charge carrier densities this model can describe charge transport very well.[12–15] Carrier-carrier interactions were also shown to widen the DOS, but the Seebeck coefficient and power factor were not investigated.[10] Widening of the DOS in systems containing dopant ions has both been measured,[16–18] and simulated.[10,19,20] Interestingly, the difference between only having c-c interactions or having both c-c and carrier-dopant (c-d) interaction in terms of the width of the DOS is small.[10]

The Seebeck coefficient is strongly, although not exclusively, affected by the DOS. The Seebeck coefficient can be calculated using[21]

$$S = -\frac{k}{q}\int_{-\infty}^{\infty} \frac{(E-E_F)}{kT}\frac{\sigma(E)}{\sigma}dE = -\frac{1}{qT}(E_{tr}-E_F), \tag{5.1}$$

where k is the Boltzmann constant, q is the unit charge, E is energy, E_F is the Fermi energy, and E_{tr} is the transport energy, which is the energy at which electronic conduction takes place on average. In appendix B, details on how we numerically obtain E_F and E_{tr} can be found. In disordered organic materials, E_{tr} is typically independent of charge carrier density, while E_F scales with charge carrier density. Their difference increases with increasing energetic disorder, leading to an increased S.[22] At a charge carrier density of 2×10^{18} cm^{-3}, lower than that in typical organic thermoelectrics,[23–27] c-c interactions dominate the density of states (DOS)[10] and therefore affect both E_F and E_{tr}, but the effect of c-c interactions on the S and power factor has yet to be investigated.

On the other hand, Heike's formula describes the Seebeck coefficient in the absence of interactions:[4] The Seebeck coefficient for a system of identical, non-interacting fermions distributed over equivalent sites is just the change of entropy of mixing upon the addition of a single charge carrier. In terms of the relative occupation of sites, c, one has[4]

$$S = \frac{k}{q}\ln\left(\frac{c}{1-c}\right). \tag{5.2}$$

Therefore, Heike's formula contains no information on disorder, chemical structure, or transport mechanism. As a result, it can be argued that if S coincides with Heike's formula, the molecular sites must be equivalent and show no disorder.[28]

In this contribution we will show how disorder, either intrinsic or as a result from dopant Coulomb potentials, increases the Seebeck coefficient compared to Heike's formula for thermopower (Eq. 5.2) through energetic filtering. As dopant density increases, the effect of dopant induced disorder is shown to decrease. We also show that c-c interactions decrease the Seebeck coefficient, such that at 10^{19} cm^{-3} the Seebeck coefficient coincides with Heike's formula. While c-c interactions keep charge carriers apart, mobile charge carriers are shown to shield dopants very strongly. Finally, we show that reducing c-c Coulomb interactions can improve the power factor by more than an order of magnitude, even with dielectric constants close to the currently achievable values.[29]

5.2 Results & Discussion

We study the effect of Coulomb correlation on the Seebeck coefficient and power factor using a Gaussian disorder model with added dopant counter ions. A kinetic Monte-Carlo algorithm is used to numerically obtain the results using a T of 300 K, a σ of 3 kT (77.6 meV), and a ε_r of 4 unless specified otherwise.[30] Dopant counter-ions are put in at random positions and share the Coulomb cut-off radius of one tenth of the simulation volume length, beyond which Coulomb interactions are not accounted for, with charge carriers. More details on the specifics of the simulations are in appendix B.

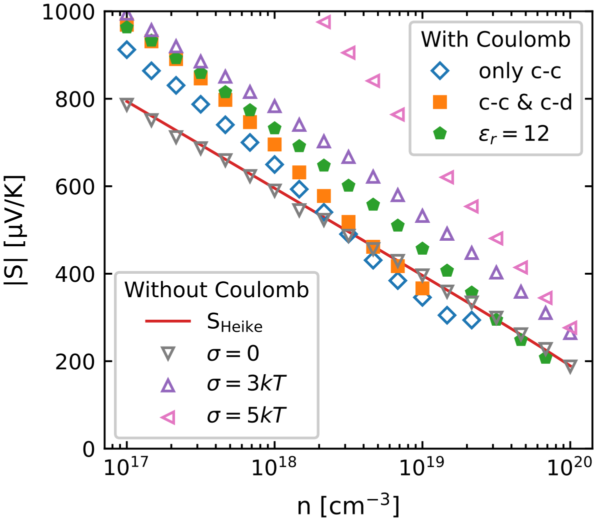

Figure 5.1: The Seebeck coefficient versus concentration of charge carriers. A number of dopant ions equal to the number of charge carriers are added (filled symbols). In the simulations with Coulomb interactions, only c-c, or both c-c and c-d, the dopants are left out to (open symbols) to show the maximum possible effect of reducing c-d interactions and the energetic disorder is 3 kT. In the simulations without Coulomb interactions, c-c and c-d interactions are effectively removed by taking ε_r equal to 1000. The Seebeck coefficient from Heike's formula is plotted as a reference (solid line). The standard error of the mean is smaller than the symbol size.

Figure 5.1 shows the simulated Seebeck coefficient versus the density of reacted dopants, which equals the number of free charge carriers. The effects of Coulomb interactions, both c-c and c-d, are modulated using the dielectric constant. First, we validate the applicability of Heike's formula by running KMC simulations without intrinsic disorder ($\sigma = 0$) and Coulomb interactions (neither c-c nor c-d). We observe in Fig. 5.1 that these simulations indeed show a Seebeck coefficient that exactly follows Heike's formula for thermopower, as all criterion for the validity of Heike's formula are met.

At a charge carrier density of 10^{17} cm^{-3}, the other simulations show a Seebeck coefficient higher than given by Heike's formula. This is to be expected, as all these KMC simulations have energetic disorder, either intrinsically or induced by dopant ions, which is known to increase the Seebeck coefficient as it effectively applies energetic filtering.[20,31] This makes low energy charge carriers less conductive compared to high energy charge carriers, increasing the Seebeck coefficient as per definition. The KMC simulations with Coulomb interactions and without dopant counter ions (blue diamonds) show a slightly lower S than the simulations with counter ions because of the absent additional disorder induced by dopants.

With increasing density, it can be observed that the simulations with and without dopant counter ions and a ε_r of 4 show a comparable S that is reduced to that of Eq. 5.2. The simulations without Coulomb interactions (emulated by setting ε_r to 1000) show that c-c interactions cause the reduction of the Seebeck coefficient. The high ε_r effectively eliminates c-c and c-d interactions, leaving only the intrinsic disorder affecting the Seebeck coefficient. While there is some gain to be made by reducing c-c interactions, even completely eliminating them only increases the Seebeck coefficient by about 200 μV/K at 10^{19} cm^{-3} at a disorder of 3 kT. The Seebeck coefficient and especially the slope of the Seebeck coefficient can be seen to increase quite strongly when changing the disorder from 3 kT to 5 kT. While this might seem favourable, the increased disorder decreases the conductivity by more than an order of magnitude at a charge carrier density of 10^{19} cm^{-3}, resulting in a reduced powerfactor.

The reduction of the Seebeck coefficient when c-c interactions start to dominate can be explained within the framework of Heike's formula: some sites are no longer available because the energy cost would be too high. The number of available sites decreases with increasing carrier density, meaning the derivative of entropy with respect to charge carrier density, the Seebeck coefficient, decreases. This is analogous to increasing c in Heike's formula. The finding that c-c interactions can push the Seebeck coefficient close to that of Heike's formula is interesting, since a Seebeck coefficient being close to Heike's formula is sometimes seen as evidence of a lack of intrinsic disorder,[28] which is still present in the KMC simulations in Fig. 5.1. The charge carrier density at which the Seebeck coefficient starts to get close to Heike's formula is very close to 10^{18} cm^{-3}, the density at which c-c interactions were found to become significant in organic materials.[10,32]

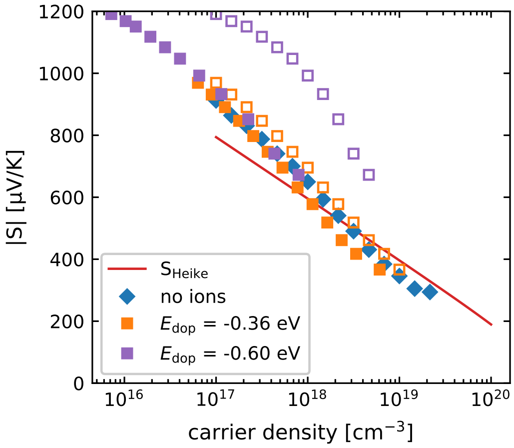

Figure 5.2: The Seebeck coefficient versus carrier density. Both free carrier density (solid symbols) and total carrier density (open symbols) are shown, where free carriers are those that are not on a dopant site or on a nearest neighbour site to a dopant. The standard error of the mean is smaller than the symbol size.

Figure 5.2 shows the Seebeck coefficient versus the carrier density. Both total carrier density (n) and free carrier density (n_{free}) are shown, where n equals the number of ionized dopants and free carriers are defined as not being on a dopant site or a nearest neighbour site to a dopant. This means that a free carrier can still be trapped on a site that has low energy because of energetic disorder.

We show three different datasets, one without dopant ions, two dopant ions with varying c-d interaction strength. The c-d interactions are modulated by changing the depth of the Coulomb potential of dopant ions (E_{dop}), where a lower E_{dop} reduces the Coulomb interaction by capturing charge carriers more strongly.

The open symbols show S versus n. These data show that increasing the c-d interaction strength increases S at a constant n by inducing more energetic disorder. The closed symbols show S versus n_{free}. Interestingly, all data collapse onto the same line when S is plotted versus n_{free}, showing that only free carriers contribute to S. Charge carriers that are on dopants do not contribute as their

Coulomb interaction is shielded by the dopant, effectively removing them from the system.

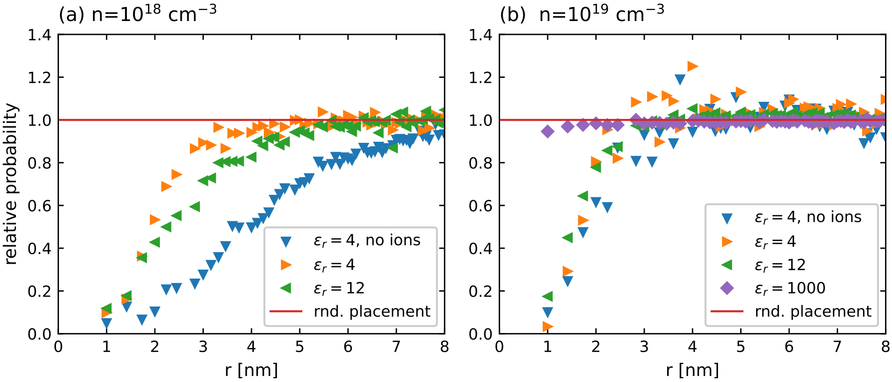

Figure 5.3: The probability of finding an electron at a certain distance from another electron normalised to the probability of finding an electron at that distance if the electrons were randomly placed for a carrier density of (a) 10^{18} cm^{-3} and (b) 10^{19} cm^{-3}.

To show the effect of c-c interactions in the KMC simulations, Fig. 5.3 shows the probability of finding an electron at a certain distance from another electron normalised to the probability if the electrons were randomly placed. Fig. 5.3a shows the relative probability at a charge carrier density of 10^{18} cm^{-3}. It can be observed that unscreened electrons ($\varepsilon_r = 4$, no ions) sit relatively far apart. When dopant counter ions are introduced ($\varepsilon_r = 4$), the charge carriers can be observed to sit much closer together. This because the randomly placed dopants effectively screen part of the charge carriers, resulting in a dipole potential that drops off in strength much more strongly with increasing r compared to a monopole from a charge carrier. Interestingly, reducing Coulomb interactions (c-c and c-d, $\varepsilon_r = 12$) increases the probability of finding carriers very close together, but reduces the probability of finding two charge carriers at intermediate distance. This is indicative of less charge carriers being stuck close to a dopant when Coulomb interactions decrease in strength. While carriers sit further apart, still the Seebeck coefficient increases slightly.

Fig. 5.3b shows the relative probability at a charge carrier density of 10^{19} cm^{-3}. When counter ions are present ($\varepsilon_r = 4$) the relative probability does not change strongly when compared to Fig. 5.3a. This shows that charge carriers are mostly close to carriers that are screened by a dopant, especially when Coulomb interactions are strong. Even without Coulomb interactions strength ($\varepsilon_r = 1000$) the charge carriers show slight correlation. This can occur even without Coulomb interaction, as only one electron is allowed per grid point.

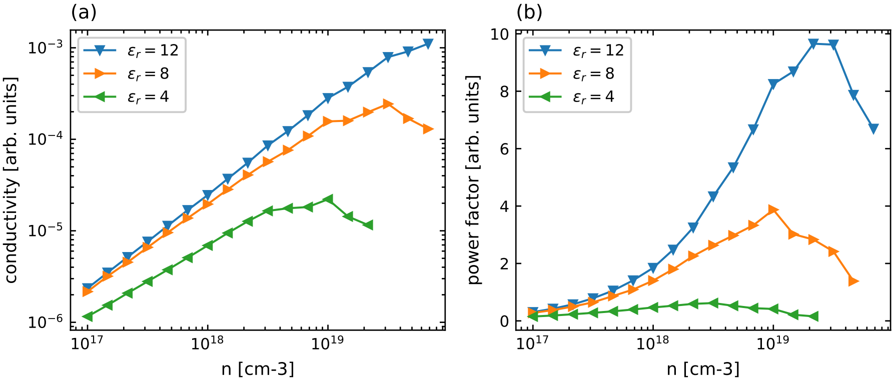

Figure 5.4: (a) Conductivity versus charge dopant density for varying degree of Coulomb interaction (modulated by ε_r). (b) The power factor versus carrier density for varying Coulomb interaction (c-c and c-d) strength, which was modulated by ε_r. The standard error of the mean is smaller than the symbol size.

Since the PF is of critical importance to thermoelectric materials and the conductivity is limited by c-c interactions,[10] the way to improve the PF would be by reducing c-c interactions. In Fig. 5.1 we observed that the Seebeck coefficient was reduced by c-c interactions, meaning it is possible to improve both the Seebeck coefficient and conductivity by reducing c-c interactions.

In Fig. 5.4a we show that the conductivity is limited by c-c interactions. As a result, the conductivity can be improved by reducing these interactions. We note, that the distribution of charge carriers in a field-effect-transistor configuration is highly non-uniform and the impact of c-c interaction may very well be different.[33] At low density, we observe that the conductivity is a result from a convolution of intrinsic disorder and c-d interactions. At a ε_r of 4 the conductivity is slightly lower than for ε_r of 8 and 12. This is because at ε_r of 4 c-d interactions are still strong compared to the energetic disorder, as the depth of the dopant potential is 0.36 eV, making the hop from the bottom of the potential to a site 1 nm away from it have an energy barrier of 180 meV while the intrinsic disorder is 0.078

eV. At ε_r of 8 the energy barrier for the shortest hop away from the dopant becomes 90 meV, which is similar to the energetic disorder, rendering the dopant potentials unimportant.

In Fig. 5.4b we show that the PF instead increases by more than a factor of 15 with decreasing Coulomb interactions (c-c and c-d). Considering the currently achievable values for ZT, this would bring the power factor far beyond the required ZT of 1 for application of organic thermoelectrics.[26] While it could be argued that the c-d interactions are mainly responsible for suppressing the conductivity, we have previously shown that at high dopant loading c-c interactions are a possible culprit.[10] As this work builds on a Gaussian disorder model and assumes hopping conductivity, the conclusions should not be applied outside their domain of validity. Within this domain of validity, however, we show that reducing c-c interactions might be a promising route towards increasing the PF in disordered organic materials, even for realistically achievable dielectric constants in the low double digits.[29]

5.3 Conclusions

We conclude that Heike's formula for thermopower is very closely reproduced by KMC simulations, confirming its validity in hopping systems. Intrinsic disorder increases the Seebeck coefficient when it dominates the DOS, which happens at low charge carrier density or with little Coulomb interaction. Dopants are shown to trap charge carriers, but the Seebeck coefficient is uniquely determined by the number of charge carriers not trapped by dopants. Carrier-carrier interactions reduce the Seebeck coefficient, which can be seen at high carrier density. This makes it possible for the Seebeck coefficient for disordered materials to coincide with the value calculated from Heike's formula at higher charge carrier densities. Reducing carrier-carrier interactions both increases the Seebeck coefficient and conductivity at high doping densities, resulting in an increased power factor.

Bibliography

[1] O. Bubnova, X. Crispin, *Energy Environ. Sci.* **2012**, *5*, 9345–9362.

[2] R. Kroon, D. A. Mengistie, D. Kiefer, J. Hynynen, J. D. Ryan, L. Yu, C. Müller, *Chem. Soc. Rev.* **2016**, *45*, 6147–6164.

[3] B. Russ, A. Glaudell, J. J. Urban, M. L. Chabinyc, R. A. Segalman, *Nat. Rev. Mater.* **2016**, *1*, 1–14.

[4] D.M. Rowe, *Thermoelectrics handbook*, Taylor & Francis, **2006**, p. 1008.

[5] Y.-J. Zeng, D. Wu, X.-H. Cao, W.-X. Zhou, L.-M. Tang, K.-Q. Chen, *Advanced Functional Materials* **2020**, *30*, 1903873.

[6] V. I. Arkhipov, E. V. Emelianova, P. Heremans, H. Bässler, *Phys. Rev. B* **2005**, *72*, 235202.

[7] V. I. Arkhipov, P. Heremans, E. V. Emelianova, H. Bässler, *Phys. Rev. B* **2005**, *71*, 045214.

[8] M. Schwarze, C. Gaul, R. Scholz, F. Bussolotti, A. Hofacker, K. S. Schellhammer, B. Nell, B. D. Naab, Z. Bao, D. Spoltore, K. Vandewal, J. Widmer, S. Kera, N. Ueno, F. Ortmann, K. Leo, *Nat. Mater.* **2019**, *18*, 242–248.

[9] J. Liu, G. Ye, H. G. O. Potgieser, M. Koopmans, S. Sami, M. I. Nugraha, D. R. Villalva, H. Sun, J. Dong, X. Yang, X. Qiu, C. Yao, G. Portale, S. Fabiano, T. D. Anthopoulos, D. Baran, R. W. A. Havenith, R. C. Chiechi, L. J. A. Koster, *Adv. Mater.* **2021**, *33*, 2006694.

[10] M. Koopmans, M. A. T. Leiviskä, J. Liu, J. Dong, L. Qiu, J. C. Hummelen, G. Portale, M. C. Heiber, L. J. A. Koster, *ACS Appl. Mater. Interfaces* **2020**, *12*, 56222–56230.

[11] H. Bässler, *physica status solidi (b)* **1993**, *175*, 15–56.

[12] V. I. Arkhipov, P. Heremans, E. V. Emelianova, G. J. Adriaenssens, H. Bässler, *J. Phys. Condens. Matter* **2002**, *14*, 9899–9911.

[13] M. C. J. M. Vissenberg, M. Matters, *Phys. Rev. B* **1998**, *57*, 12964–12967.

[14] C. Tanase, E. J. Meijer, P. W. M. Blom, D. M. de Leeuw, *Phys. Rev. Lett.* **2003**, *91*, 216601.

[15] W. F. Pasveer, J. Cottaar, C. Tanase, R. Coehoorn, P. A. Bobbert, P. W. M. Blom, D. M. de Leeuw, M. A. J. Michels, *Phys. Rev. Lett.* **2005**, *94*, 206601.

[16] X. Lin, G. E. Purdum, Y. Zhang, S. Barlow, S. R. Marder, Y.-L. Loo, A. Kahn, *Chemistry of Materials* **2016**, *28*, 2677–2684.

[17] J.-P. Yang, W.-Q. Wang, F. Bussolotti, L.-W. Cheng, Y.-Q. Li, S. Kera, J.-X. Tang, X.-H. Zeng, N. Ueno, *Applied Physics Letters* **2016**, *109*, 093302.

[18] C. Gaul, S. Hutsch, M. Schwarze, K. S. Schellhammer, F. Bussolotti, S. Kera, G. Cuniberti, K. Leo, F. Ortmann, *Nat. Mater.* **2018**, *17*, 439–444.

[19] A. Fediai, F. Symalla, P. Friederich, W. Wenzel, *Nat. Commun.* **2019**, *10*, 1–7.

[20] G. Zuo, H. Abdalla, M. Kemerink, *Phys. Rev. B* **2016**, *93*, 235203.

[21] H. Fritzsche, *Solid State Communications* **1971**, *9*, 1813–1815.

[22] A. V. Nenashev, J. O. Oelerich, S. D. Baranovskii, *Journal of Physics: Condensed Matter* **2015**, *27*, 093201.

[23] J. Liu, L. Qiu, G. Portale, M. Koopmans, G. t. Brink, J. C. Hummelen, L. J. A. Koster, *Adv. Mater.* **2017**, *29*, 1701641.

[24] D. Kiefer, A. Giovannitti, H. Sun, T. Biskup, A. Hofmann, M. Koopmans, C. Cendra, S. Weber, L. J. A. Koster, E. Olsson, J. Rivnay, S. Fabiano, I. McCulloch, C. Müller, *ACS Energy Lett.* **2018**, *3*, 278–285.

[25] J. Liu, G. Ye, B. van der Zee, J. Dong, X. Qiu, Y. Liu, G. Portale, R. C. Chiechi, L. J. A. Koster, *Adv. Mater.* **2018**, *30*, DOI `10.1002/adma.201804290`.

[26] J. Liu, B. van der Zee, R. Alessandri, S. Sami, J. Dong, M. I. Nugraha, A. J. Barker, S. Rousseva, L. Qiu, X. Qiu, N. Klasen, R. C. Chiechi, D. Baran, M. Caironi, T. D. Anthopoulos, G. Portale, R. W. A. Havenith, S. J. Marrink, J. C. Hummelen, L. J. A. Koster, *Nat. Commun.* **2020**, *11*, 1–9.

[27] D. Kiefer, R. Kroon, A. I. Hofmann, H. Sun, X. Liu, A. Giovannitti, D. Stegerer, A. Cano, J. Hynynen, L. Yu, Y. Zhang, D. Nai, T. F. Harrelson, M. Sommer, A. J. Moulé, M. Kemerink, S. R. Marder, I. McCulloch, M. Fahlman, S. Fabiano, C. Müller, *Nat. Mater.* **2019**, *18*, 149–155.

[28] D. Venkateshvaran, M. Nikolka, A. Sadhanala, V. Lemaur, M. Zelazny, M. Kepa, M. Hurhangee, A. J. Kronemeijer, V. Pecunia, I. Nasrallah, I. Romanov, K. Broch, I. McCulloch, D. Emin, Y. Olivier, J. Cornil, D. Beljonne, H. Sirringhaus, *Nature* **2014**, *515*, 384–388.

[29] S. Rousseva, H. d. Besten, F. S. van Kooij, E. L. Doting, N. Y. Doumon, E. Douvogianni, L. J. Anton Koster, J. C. Hummelen, *The Journal of Physical Chemistry C* **2020**, *124*, 8633–8638.

[30] M. C. Heiber, *J. Open Source Softw.* **2020**, *5*, 2307.

[31] G. Kim, K. P. Pipe, *Phys. Rev. B* **2012**, *86*, 085208.

[32] F. Liu, H. van Eersel, B. Xu, J. G. E. Wilbers, M. P. de Jong, W. G. van der Wiel, P. A. Bobbert, R. Coehoorn, *Phys. Rev. B* **2017**, *96*, 205203.

[33] A. Sharma, F. W. A. van Oost, M. Kemerink, P. A. Bobbert, *Phys. Rev. B* **2012**, *85*, 235302.

APPENDIX A

Electrical Conductivity of Doped Organic Semiconductors Limited by Carrier-Carrier Interactions

As seen in Figure A.1 at low carrier density the DOS can be described very well by just the intrinsic disorder as it does not change upon adding dopants and mobile charge carriers. At high charge carrier density however, the dopants have a broadening effect on the DOS. It seems to stay a Gaussian but increase in width. The mobile charge carriers can be seen to shield the dopants, because the DOS width decreases upon adding mobile charge carriers to a DOS formed by intrinsic disorder and dopant-ions. We can conclude that at high carrier density both dopants and mobile charge carriers should be taken into account when simulating disordered organic semiconductors.

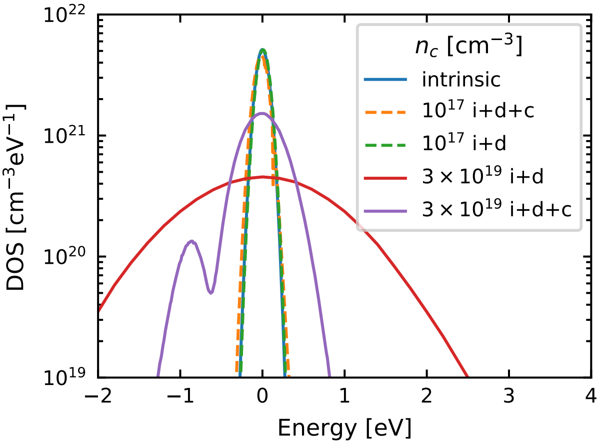

Figure A.1: DOS for intrinsic disorder (i), intrinsic disorder and dopants (i+d), and intrinsic disorder, dopants, and mobile charge carriers (i+d+c) at low carrier density (10^{17} cm^{-3}) and high carrier density (3×10^{19} cm^{-3}).

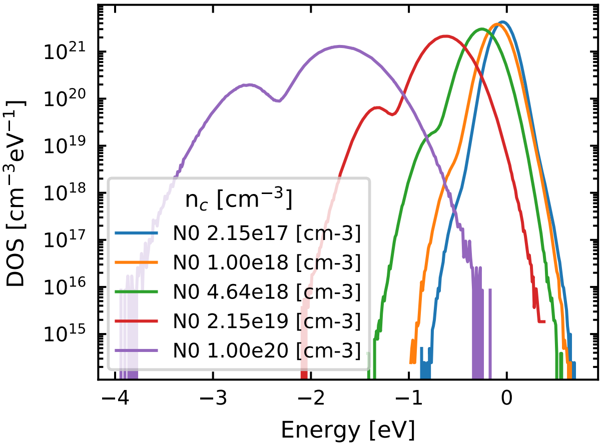

Figure A.2: DOS with dopant potentials for different charge carrier densities. Charge carrier densities are equal to the densities of dopant counterions.

In figure A.3 the DOS at the Fermi level (μ) is shown. At non-zero temperature the DOS as the Fermi level is expected to go to a finite value that is independent of the charge carrier density [1, 2]. At higher charge carrier densities the DOS at the Fermi level indeed becomes constant in figure A.3. All simulations were performed at room temperature, so we cannot investigate the temperature dependence of the DOS at the Fermi level.

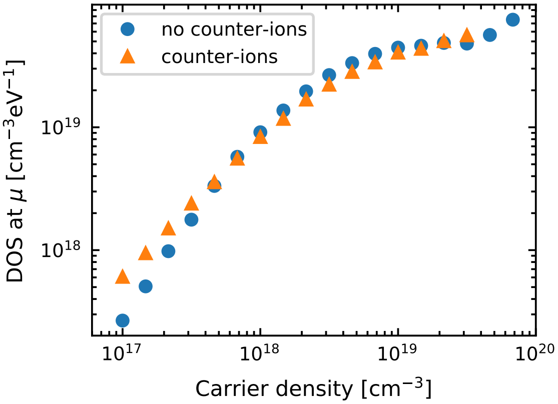

Figure A.3: The DOS at the Fermi level in simulations without dopant counter-ions as calculated using KMC simulations.

Figure A.4 shows two different ways of equilibrating a simulation volume of a cubic lattice with mobile charge carriers. Figure A.4a shows the difference between choosing a fixed and too low number of equilibration hops and a fixed simulation volume versus a fixed number of charge carriers and equilibrating until the temperature of the charge carriers is close enough to the set temperature in the KMC simulation. This shows that one should be careful in determining whether the charge carriers have properly equilibrated as the simulated conductivity trend depends strongly on the charge carriers reaching equilibrium and can seem plausible even when the charge carriers have not equilibrated. Keeping the number of carriers constant instead of the lattice size helps to make sure that equilibration takes roughly the same number of hops regardless of the charge carrier density. Figure A.4b shows that also the DOS resulting from the KMC simulation changes when the charge carriers equilibrate, showing a Coulomb pseudo-gap only once reaching equilibrium.

A.1 Methods

Numerical techniques We used Excimontec v1.0.0-rc.3,[3] an open source KMC simulation tool to simulate the hopping process in disordered organic semiconductors. The system was represented by a regular cubic grid with a lattice parameter,

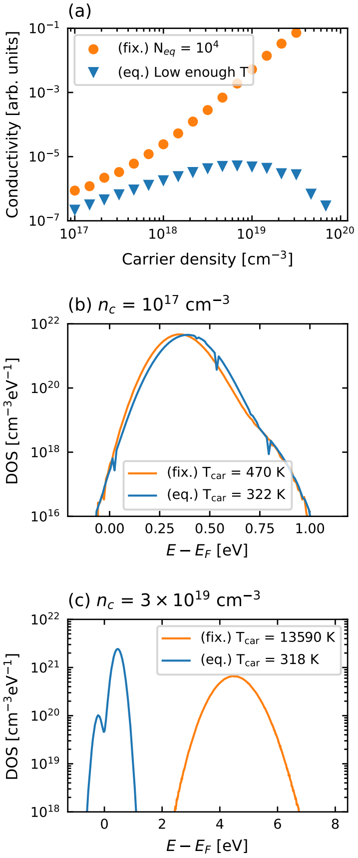

Figure A.4: An equilibrated simulation state is reached by inspecting the temperature extracted from a fit of the o-DOS to the Fermi-Dirac function times the DOS. If the temperature is close to the value set in the simulation parameters, the simulation has reached equilibrium. An unequilibrated state is calculated by setting a low and fixed number of hops (10^4) to equilibrate. (a) The simulated conductivity for a fixed number of equilibration events (N_{eq}) of 10^4 (fix.) and the conductivity for a simulation that is left to iterate until equilibrium is reached (eq.). (b) The DOS for simulations (fix.) and (eq.) at a charge carrier density (n_c) of 10^{17} cm^{-3} with on the x-axis the energy minus the Fermi energy for the different simulations. (c) The DOS for simulations (fix.) and (eq.) at a charge carrier density (n_c) of $3{\times}10^{19}$ cm^{-3} with on the x-axis the energy minus the Fermi energy for the different simulations.

a, of 1 nm containing a fixed amount of charge carriers at high carrier density, where the lattice points are hopping sites for charge carriers. The number of charge carriers is set at ∼10,000 and the grid size was scaled in order to set the desired charge carrier density. For low charge carrier density, the grid dimensions were limited to 150×150×150 for memory saving purposes and because the grid size has no influence on the calculated physical properties of the system at these low carrier densities. Periodic boundary conditions in three dimensions were assumed to counteract finite size effects in the simulations. Simulations were performed both on systems containing only mobile charge carriers and systems containing mobile charge carriers and immobile charged dopant ions, making the second system electrically neutral.

In the KMC simulations a dopant was placed on a lattice point, but the Coulomb potential of the ionized dopant was calculated with r_{dop} added to the lattice distance. This means that the site energy was calculated as

$$E_{\text{site}} = E_{\text{int}} + \sum_{0}^{\text{N}_{\text{dop}}} V_C(r_{\text{lat}} + r_{\text{dop}}), \tag{A.1}$$

where E_{int} is the contribution from the intrinsic Gaussian disorder of the organic semiconductor, N_{dop} is the number of dopants, r_{lat} is the distance on the lattice from the site to the dopant, r_{dop} is the effective dopant radius, and V_C is the Coulomb potential of a single dopant at distance r given by

$$V_C(r) = \begin{cases} -\dfrac{q}{4\pi\varepsilon\kappa r}, & \text{if } r - r_{\text{dop}} < r_{\text{cut}} \\ 0, & \text{otherwise,} \end{cases}$$

where r_{cut} is a cut-off radius which we take to be one tenth of the simulation volume length and therefore ∼2.2 times the cubic nearest neighbour distance of the mobile charge carriers.

Both mobile charge carriers and dopants, if applicable, were initially placed at random lattice positions. The mobile charge carriers were then redistributed according a rejection free KMC algorithm until steady state was reached. For the hop rates in the KMC algorithm, a Miller-Abrahams expression was used[4] and a temperature of 300 K and an inverse localization length of 10 nm^{-1} was used to calculate the hopping rates. The hop rates therefore only depend on the distance and energy difference between an initial and target site. The site energies of lattice sites contain a static component from intrinsic disorder which we took to be 77.6 meV, typical for a fullerene system, combined with the Coulomb potential of the dopant ions. Additionally, a dynamic component from the Coulomb interactions with mobile charge carriers surrounding the lattice site for which a dielectric constant of 4 was used.

For both static and dynamic Coulomb interactions an identical cut-off radius of $1/10^{th}$ of the simulation volume length was used. Because of the scaling of the simulation volume this means that for the higher density simulations the cut-off radii were $\sim$2.2 times the cubic nearest neighbour distance of the charge carriers. It has been shown that the average carrier separation roughly determines how large the Coulomb and cut-off radius should be.[5]

Different ways of defining the Coulomb potential of the ionized dopants were attempted, but the details did not change the outcome of the simulations. Upon completion of a hop, a selective recalculation procedure was used to calculate hopping rates for carriers near the initial and target sites up to a radius that equals the cut-off radius for the Coulomb interactions.

The simulation procedure then entailed putting the desired amount of mobile charge carriers and dopant ions in the simulation volume at random. An electric field of 10^7 V/m was then applied along a lattice direction of the simulation volume. Mobile charge carriers then hopped according to the described KMC algorithm for a certain number of hops to let the system cool down. After cooling, the simulation was continued until the statistical error on the output parameters was acceptable. To check the temperature of the simulation after the cooling period the o-DOS of the charge carrier was fit to the DOS times the Fermi-Dirac distribution. If the temperature of the fit Fermi-Dirac distribution is within 15% of the target temperature, we accept the simulation. If the temperature is too high we continue calculation until the desired temperature is reached. During the simulation period, the occupied density of states (o-DOS) is sampled once every 1000 hops and the density of states (DOS) is sampled once at the end of the simulation.

Doing KMC simulations on large enough simulation volumes with carrier-carrier interactions takes a huge computational effort. On the Peregrine computer cluster we used 1140 cores for roughly 20 days to get the data for Fig. 4.2b. The statistical error was lower than expected meaning that the core count can be lowered slightly, but efforts to reduce the computation time might lead to systematic errors.

Master equation (ME) simulations were used for validating KMC simulation results. In this GDM an uncorrelated Gaussian distribution of hopping sites was assumed to constitute the DOS. The GDM was used calculate to the dependence of conductivity on charge carrier density in the absence of Coulomb interactions. A simple cubic lattice was used as a grid for these simulations, where a is, as in the KMC simulations, 1 nm. To calculate the charge carrier mobility occupational probabilities of the lattice sites were used instead of physical charge carriers. At the start of the ME simulation every site was a assigned a random energy from a Gaussian distribution with a width of 77.6 meV. An electric field was applied along a lattice direction effectively tilting the energetic landscape. The effect or this electric field was then calculated by solving the steady-state Pauli master equation for all target sites j

$$\sum_j [W_{i\to j} n_i(1-n_j) - W_{j\to i} n_j(1-n_i)] = 0, \tag{A.2}$$

where i is the initial site, $W_{i\to j}$ is the transition rate from i to j, $W_{j\to i}$ is the rate of the reverse transition, n_i and n_j are the occupational probabilities of site i and j. For the transition rates $W_{i\to j}$ and $W_{j\to i}$ Miller-Abrahams hopping rates[4] were used with the same parameters as in the KMC simulations. The mobility was then calculated as

$$\mu = \frac{\sum_{ij} w_{i\to j} n_i(1-n_j)(\vec{r_j} - \vec{r_i}) \cdot \hat{F}}{n_c|\vec{F}|}, \tag{A.3}$$

where $\hat{F} = \vec{F}/|\vec{F}|$, is the unit vector in the direction of the electric field, $\vec{F}$ is the electric field vector, $\vec{r_j}$ and $\vec{r_i}$ are position vectors of the target and initial site of a hop with respect to some point, n_c is the charge carrier density per unit volume.

Experimental methods n-DMBI was supplied by Sigma Aldrich and a previously reported procedure was used to synthesize PTEG-1.[6] Borosilicate glass substrates were washed using, in order of use, detergent, acetone, and isopropanol. Afterwards the substrates were dried with a nitrogen gun and recieved a UV-ozone treatment for 20 minutes. Various amounts of n-DMBI solution (5 mg mL^{-1} in chloroform) were mixed with a PTEG-1 solution (5 mg mL^{-1} in chloroform) to fabricate doped PTEG-1 films. The film thickness (d) was measured using ellipsometry to be between 40 and 50 nm. To measure electrical conductivity, a geometry using parallel line-shape Au electrodes with a width (w) of 13 mm and a channel length (L) of 100-300 μm as top contact was employed. In a N_2 glove box, voltage-sourced two-point conductivity measurements were conducted. The electrical conductivity (σ) was calculated as $\sigma = (J/V \times L/(w \times d))$. For a reference measurement of commercial PEDOT:PSS (Clevios P VP Al 4083) the conductivity was measured to be 0.06 Sm^{-1}, well in line with the expected value between 0.02 and 0.2 Sm^{-1}.

Grazing incidence wide-angle X-ray scattering (GIWAXS) measurements were performed using a MINA X-ray scattering instrument built on a Cu rotating anode source (λ=1.5413 Å). 2D patterns were collected using a Vantec500 detector (1024x1024 pixel array with pixel size 136x136 microns) located 93 mm away from the sample. The PTEG-1 films were placed in reflection geometry at certain incident angles α_i with respect to the direct beam using a Huber goniometer. GIWAXS patterns were acquired using incident angles from of 0.14°. The direct beam centre position on the detector and the sample-to-detector distance were calibrated using the diffraction rings from standard silver behenate and Al_2O_3 powders. All the necessary corrections for the GIWAXS geometry were applied to the raw patterns using the GIXGUI Matlab toolbox. The reshaped GIWAXS patterns, taking into account the inaccessible part in reciprocal space (wedge-shaped corrected patterns), are presented as a function of the vertical and parallel scattering vectors q_z and q_r. The scattering vector coordinates for the GIWAXS geometry are given by:

$$q_x = \frac{2\pi}{\lambda}\big(\cos(2\theta_f)\cos(\alpha_f) - \cos(\alpha_i)\big) \tag{A.4}$$

$$q_y = \frac{2\pi}{\lambda}\big(\sin(2\theta_f)\cos(\alpha_f)\big) \tag{A.5}$$

$$q_z = \frac{2\pi}{\lambda}\big(\sin(\alpha_i) + \sin(\alpha_f)\big) \tag{A.6}$$

where $2\theta_f$ is the scattering angle in the horizontal direction and α_f is the exit angle in the vertical direction. The parallel component of the scattering vector is thus calculated as $q_r = \sqrt{q_x^2 + q_y^2}$.

APPENDIX B

Carrier-Carrier Coulomb Interactions Reduce Power Factor in Organic Thermoelectrics

B.1 KMC Simulation Details

For the KMC simulations, cubic grid containing roughly 10,000 charge carriers was used. The charge carrier density was set by scaling the grid dimensions, but capped at 150x150x150 for low charge carrier density. Periodic boundary conditions were employed to limit finite size effects. An electric field of 10^7 Vm^{-1} was applied along one of the lattice directions.

Miller-Abrahams hopping expressions were used to calculate the hopping rates using an inverse localization length of 10 nm^{-1}.[1] Hops were performed until the charge carrier temperature was within 15% of the target temperature of 300 K.

In our simulations, the transport energy is defined as:

$$E_{tr} = \frac{\sum_{m=1}^{N_{hops}} (E_{fm} - E_{im}) * r_{zm}}{\sum_{m=1}^{N_{hops}} r_{zm}},$$

where N_{hops} is the number of hops, E_i and E_f are the site energies of the initial and final hopping sites of hop number m, r_{zm} is the hopping distance along the field direction of hop number m. In other words, the transport energy is the average energy at which hops take place, weighted by the distance of a hop along the electric field direction.

The Fermi energy is obtained by fitting a Fermi-Dirac (FD) distribution multiplied by the density of states (DOS) to the occupied density of states (o-DOS). The fitting parameters in the FD distribution are the Fermi energy E_F and the charge carrier temperature T_{car}. When the simulations have converged, the lattice temperature T is approximately equal to T_{car}.

B.2 Calculation of the Relative Probability of Site Occupation

The relative probability of finding a charge carrier at a certain position with respect to another is found by an iterative procedure. For every charge carrier in the system, we iterate over all sites within a certain cut-off radius away from the charge carrier. Sites at the same distance are then grouped, such that we have a total number of sites at a certain distance from the charge carrier and what fraction of those are occupied. If we then divide that filled site fraction by the fraction of sites filled in the total lattice, we get the relative probability as in Fig. 5.3.

APPENDIX C

Voltage Deficit in Wide Band Gap Perovskite Solar Cells

C.1 Device Parameters

The device parameters for our reference device are shown in table C.1. The corresponding JV curve is shown in figure 1. For our parameter sweep, some parameters in the hole transport layer (right transport layer) are changed. These new parameters are shown in table C.2.

C.2 Methods

In the recent past we adapted our device model for to make it more suitable for simulations on perovskite solar cells [1, 2]. The model solves a discretized form of the 1-dimensional classic drift-diffusion equations,

$$J_n = -qn\mu_n \frac{\partial V}{\partial x} + qD_n \frac{\partial n}{\partial x} \tag{C.1}$$

for electrons and

$$J_p = -qp\mu_p \frac{\partial V}{\partial x} + qD_p \frac{\partial p}{\partial x} \tag{C.2}$$

Table C.1: Device parameters for our reference device. This device does not include doping in the transport layers.

Parameter	Value	Unit
Device length	400	nm
Perovskite dielectric constant	22	
Perovskite conduction band	3.3	eV
Perovskite valence band	5.0	eV
Perovskite density of states	10^{25}	m^{-3}
Perovskite mobility (electrons and holes)	10^{-4}	m^{-2}/Vs
Work function cathode	3.5	eV
Work function anode	4.8	eV
Transport layer thickness (ETL and HTL are equal)	35	nm
N_{cv} transport layers	10^{26}	m^{-3}
mobility transport layers	10^{-7}	m^{-2}/Vs
Transport layer dielectric constant (ETL and HTL)	4	1
ETL conduction band	3.3	eV
HTL valence band	5.0	eV
Mobile ion density	10^{21}	m^{-3}
Interface trap density perovskite/TL interface	10^{12}	m^{-2}
Interface trap density grain boundaries	3×10^{10}	m^{-2}
Interface trap level (interface and grain boundaries)	4.15	eV

Table C.2: Parameters for the right transport layer (HTL) in the parameter sweep.

Parameter	Value	Unit
Perovskite conduction band	3.3	eV
Density of states right transport layer	10^{25}	m^{-3}
Transport layer dielectric constant (ETL and HTL)	4	1
Interface trap density perovskite/TL interface	0	m^{-2}

for holes respectively, where J_n and J_p are the electron and hole current densities, q is the unit charge, n and p are the electron and hole densities, μ_n and μ_p are the electron and hole mobilities, V is the electrostatic potential, and D_n and D_p are the electron and hole diffusion constants following from the Einstein relations [3]. The unknowns in these equations are the electrostatic potential, and the electron and hole densities. The electrostatic potential can be solved from Poisson's equation,

$$\frac{\partial^2}{\partial x^2}V(x) = -\frac{q}{\varepsilon(x)}\big(p(x) - n(x) + N_D^+(x) - N_A^-(x) + \sigma_{tr}^{bulk} + \sigma_{tr}^{int} + I^+ - I^-\big) \tag{C.3}$$

where ε is the permittivity, N_D^+ and N_A^- are the ionized p-type and n-type doping density, and I^+ and I^- are the positive and negative, possibly mobile, ion densities, and σ_{tr}^{bulk} and σ_{tr}^{int} are the bulk and interface trap charge density. A Schottky contact at the contacts is assumed at the boundaries of the simulations volume, resulting in a boundary condition for the Poisson equation of the form

$$q\big(V(L) - V(0)\big) = W_c - W_a - V_{app}, \tag{C.4}$$

where $V(L)$ and $V(0)$ are the electrostatic potentials at the cathode and anode respectively, W_c and W_a are the work functions of the cathode and anode, and V_{app} is the applied voltage between the cathode and anode.

Charge carrier generation, recombination, and extraction is governed by the continuity equations

$$G = \frac{\partial n}{\partial t} - \frac{1}{q}\frac{\partial J_n}{\partial x} \tag{C.5}$$

$$G = \frac{\partial p}{\partial t} + \frac{1}{q}\frac{\partial J_p}{\partial x} \tag{C.6}$$

where G is the generation, or recombination if G is negative, per unit time. What is left is to define expressions for generation and recombination. Two different recombination mechanisms are included. The band-to-band recombination rate is determined by

$$R_b = k_b\big(np - n_i^2\big), \tag{C.7}$$

where k_b is the band-to-band recombination constant, and n_i is the intrinsic carrier density. Trap assisted recombination, or Shockley-Read-Hall recombination is governed by

$$R_{SRH} = \frac{C_n C_p\big(N_{trap} + P_{trap}\big)}{C_n\big(n + n_o\big) + C_p\big(p + p_o\big)}\big(np - n_i^2\big), \tag{C.8}$$

where R_{SRH} is the Shockley-Read-Hall recombination rate, C_n and C_p are the electron and hole capture coefficients of traps, N_{trap} and P_{trap} are the electron and hole trap densities, and n_o and p_o are defined as

$$n_o = N_c \exp\left(- \frac{E_c - E_{trap}}{k_B T} \right) \tag{C.9}$$

$$p_o = N_c \exp\left(\frac{E_v - E_{trap}}{k_B T} \right) \tag{C.10}$$

where N_c is the density of states, E_c and E_v are the conduction and valence band energies, E_{trap} is the trap energy, k_B is Boltzmann's constant, and T is the temperature. In our device model, traps can be present at the perovskite-transport layer interface, at the grain boundaries of the perovskite, and in the bulk. For interface trapping, the rate equations can be found in chapter 2.

The generation of carriers is determined by light absorption in the perovskite, which varied between uniform, exponential from the n-side of the device and exponential from the p-side of the device. Because of the low exciton binding energy in perovskite, light absorption is assumed to always result in free carriers [4].

Table C.3: Parameters that are randomly chosen are shown on the left. A value was randomly picked between the lower and upper limit on either a linear or logarithmic scale, as indicated in the last column.

parameter	lower limit	upper limit	scale
thickness trapsport layer [m]	50	50	lin
doping transport layer [m^{-3}]	10^{17}	10^{23}	log
mobility transport layer [m^2/Vs]	10^{-9}	10^{-5}	log
perovskite/TL band offset [eV]	-0.2	0.3	lin
contact/TL band offset [eV]	0	0.4	lin
relative permittivity TL	3	30	lin
effective density of states TL [m^{-3}]	10^{22}	10^{28}	log
surf. trap dens. perovskite/TL int. [m^{-2}]	10^{12}	10^{14}	log
mobile ion density [m^{-3}]	10^{16}	10^{22}	log
are ions allowed in TL (yes/no)	0	1	n.a.

In figure 3.4, a large range of parameters is scanned to obtain the different data points. In table C.3, these parameter ranges are shown.

Curriculum vitae

Education

2015-2017	Master of Applied Physics *(cum laude)* University of Groningen
2010-2015	Bachelor of Applied Physics University of Groningen

Honours & Awards

2021	Best Talk Award E-MRS Symposium C
2021	Open Research Award University of Groningen

List of Publications

1. **Koopmans, M.** and Koster, L.J.A., 2022, Voltage Deficit in Wide Bandgap Perovskite Solar Cells: The Role of Traps, Band Energies, and Effective Density of States. Sol. RRL p.2200560.

2. **Koopmans, M.**, Le Corre, V.M. and Koster, L.J.A., 2022. SIMsalabim: An open-source drift-diffusion simulator for semiconductor devices. Journal of Open Source Software, 7(70), p.3727.

3. **Koopmans, M.** and Koster, L.J.A., 2021. Carrier–carrier Coulomb interactions reduce power factor in organic thermoelectrics. Applied Physics Letters, 119(14), p.143301.

4. Le Corre, V.M., Sherkar, T.S., **Koopmans, M.** and Koster, L.J.A., 2021. Identification of the dominant recombination process for perovskite solar cells based on machine learning. Cell Reports Physical Science, 2(2), p.100346.

5. Liu, J., Ye, G., Potgieser, H.G., **Koopmans, M.**, Sami, S., Nugraha, M.I., Villalva, D.R., Sun, H., Dong, J., Yang, X. and Qiu, X., 2021. Amphipathic Side Chain of a Conjugated Polymer Optimizes Dopant Location toward Efficient N-Type Organic Thermoelectrics. Advanced Materials, 33(4), p.2006694.

6. **Koopmans, M.**, Leiviskä, M.A., Liu, J., Dong, J., Qiu, L., Hummelen, J.C., Portale, G., Heiber, M.C. and Koster, L.J.A., 2020. Electrical conductivity of doped organic semiconductors limited by carrier–carrier interactions. ACS applied materials & interfaces, 12(50), pp.56222-56230.

7. Kiefer, D., Giovannitti, A., Sun, H., Biskup, T., Hofmann, A., **Koopmans, M.**, Cendra, C., Weber, S., Koster, L.J.A., Olsson, E. and Rivnay, J., 2018. Enhanced n-doping efficiency of a naphthalenediimide-based copolymer through polar side chains for organic thermoelectrics. ACS energy letters, 3(2), pp.278-285.

8. Liu, J., Qiu, L., Portale, G., Torabi, S., Stuart, M.C., Qiu, X., **Koopmans, M.**, Chiechi, R.C., Hummelen, J.C. and Koster, L.J.A., 2018. Side-chain effects on N-type organic thermoelectrics: a case study of fullerene derivatives. Nano Energy, 52, pp.183-191.

9. Liu, J., Qiu, L., Portale, G., **Koopmans, M.**, Ten Brink, G., Hummelen, J.C. and Koster, L.J.A., 2017. N-Type Organic Thermoelectrics: Improved Power Factor by Tailoring Host–Dopant Miscibility. Advanced Materials, 29(36), p.1701641.

10. Qiu, L., Liu, J., Alessandri, R., Qiu, X., **Koopmans, M.**, Havenith, R.W., Marrink, S.J., Chiechi, R.C., Koster, L.J.A. and Hummelen, J.C., 2017. Enhancing doping efficiency by improving host-dopant miscibility for fullerene-based n-type thermoelectrics. Journal of Materials Chemistry A, 5(40), pp.21234-21241.

Summary

Perovskite solar cells are starting to rival silicon solar cells in terms of power conversion efficiency. One of the most likely applications for perovskite solar cells is however not beating silicon, but joining silicon. The perovskite-silicon tandem is nearing 30% certified efficiency, and has room to grow still. One of the most used methods to model electric internals of a solar cell is that of drift-diffusion simulation. One of the aspects that makes perovskite solar cells tricky to model is the wide variation of material properties throughout the solar cells stack. Interfacial trap assisted recombination between perovskite and charge transport layers is often the performance bottleneck in performance for perovskite solar cells, making the physical description of the interface of paramount importance.

This type of recombination depends most strongly on the minority carrier and trap density near the interface. Because of unaligned bands or effective density of states differences between perovskite and transport layer, the mobile carrier density can have large discontinuities at the interface. The classical expression for bulk Shockley-Read-Hall recombination considers the generation and recombination from a trap to and from the valence and conduction band at some point in space. For interfacial trapping, however, it is more accurate to consider trapping and detrapping from either side of the interface, as charge densities might differ strongly on either side. In chapter 2 we introduce a derivation, discretization, and linearization of trap assisted recombination at an interface. We obtain a linearized result in steady-state to stabilize the system of continuity and Poisson equations that now contain larger off-diagonal terms. An expression for transient simulations is obtained to allow simulation of trapping and detrapping in transient photovoltage and transient photocurrent experiments. The interfacial recombination implementation shows significant differences compared to classical implementations at an interface in simulated solar cell performance, especially in terms of open-circuit voltage.

In chapter 3 the newly developed interfacial recombination implementation is used to investigate the voltage deficit in wide band gap perovskite solar cells. Wide band gap cells are required for perovskite silicon tandems, but lag behind their lower band gap counterparts in performance metrics, especially the open circuit voltage. To investigate the voltage deficit, a large number of simulations are performed to look for trends that hold despite changing of other solar cell parameters. The open circuit voltage is found to be proportional to the product of trap density and minority carrier density in the perovskite near the interface with the transport layer. The minority carrier density in turn depends on the potential drop over the perovskite layer, where a large electric field aiding extraction keeps the minority carrier density low near the interface. To maximize the electric field that aids extraction, the offset in effective density of states and band alignment between perovskite and transport layer should be tuned in a coordinated manner. For perovskite solar cells with organic transport layers specifically, this means that the transport layer effective density of states is likely much larger than that in the perovskite layer. This requires de-aligning the perovskite and transport layer bands to prevent a charge carrier build up in the transport layer. This insight allows device makers to attain a high open circuit voltage in wide band gap perovskite solar cells despite a large number of defects at the interface.

Chapters 4 and 5 focus on transport phenomena in doped organic semiconductors. These materials are not only used as transport layers in perovskites solar cells, but also in organic thermoelectrics. Organic thermoelectrics are used to partially convert heat to electrical energy. They are mostly interesting for supplying energy for low power wearable or remote sensors, as their energy need and operating temperature are typically modest. In these materials, high conductivities are required to attain optimal performance for a given host material. Doping is often used to increase conductivity by increasing the charge carrier density. The problem is that often, conductivity no longer increases with doping levels at the high charge carrier densities required for organic thermoelectrics.

In chapter 4, experiments, analytical estimations, and kinetic Monte Carlo simulations are performed to investigate this problem. Experimentally, we rule out morphological changes as the root cause for this issue in a doped fullerene system. Analytically, it is found that carrier-carrier interactions can be expected to limit performance in at the charge carrier densities found in the organic materials studied. Using kinetic Monte Carlo simulations, carrier-carrier interactions shown to manifest in a Coulomb pseudo-gap at room temperature at high doping levels.

In chapter 5, the focus is on relevant physics of doped organic semiconductors for thermoelectric application. It is found that the Seebeck coefficient in these materials depends solely on the number of free charge carriers, or the number of carriers not stuck on a dopant. Moreover, it is found that both the Seebeck coefficient and the conductivity of highly doped organic semiconductors are reduced by carrier-carrier interactions. This means that reducing carrier-carrier could be a key strategy to advance organic thermoelectrics.

Samenvatting

Perovskiete zonnecellen rivaliseren silicium zonnecellen in termen van efficiëntie. Een van de waarschijnlijkste toepassingen is echter niet het vervangen van silicium, maar het samengaan met silicium. Perovskiet-silicium tandem zonnecellen halen tegenwoordig bijna 30% in gecertificeerde efficiëntie en de efficiëntie groeit nog steeds door. Een van de meest gebruikte methoden om de elektrische eigenschappen te modelleren is drift-diffusie simulatie. De grote variatie aan materiaaleigenschappen op verschillende plekken in de zonnecel maakt perovskiete zonnecellen echter lastig te modelleren. Ladingsvallen op het grensvlak tussen perovskiet en transportlaag zijn doorgaans het knelpunt voor de prestaties van de zonnecellen. Dit maakt een goede beschrijving van het grensvlak tussen perovskiet en transportlaag, en de daar voorkomende recombinatie essentieel.

De recombinatie op het grensvlak hangt vooral af van de hoeveelheid ladingsvallen en minderheidsladingsdragers bij het grensvlag. Door niet uitgelijnde banden of een verschil in de effectieve toestandsdichtheid, kan de ladingsdragersdichtheid grote discontinuïteiten vertonen aan wederzijde van het grensvlak. De klassieke uitdrukking voor Shockley-Read-Hall recombinatie in de bulk, beschouwd generatie en recombinatie van een val richting zowel de valentie als de conductie band op hetzelfde punt in de ruimte. Voor recombinatie over het grensvlak is het echter nauwkeuriger om recombinatie en generatie naar beide kanten van het grensvlak toe te staan, omdat de ladingsdragersdichtheid aan beide kanten sterk kan verschillen. In hoofdstuk 2 introduceren we daarom een afleiding, discretisatie, en linearisatie van ladingsval-geassisteerde recombinatie op het grensvlak. We lineariseren de resultaten voor stationaire toestand om het systeem van continuïteits- en Poisson vergelijkingen te stabiliseren. Een tijdsafhankelijke uitdrukking wordt verkregen om simulatie van de tijdsafhankelijke fotostroom en het tijdsafhankelijke fotovoltage mogelijk te maken. De implementatie van recombinatie op het grensvlak vertoont significante verschillen met implementatie van de klassieke vergelijkingen op een grensvlak, vooral in de open-klem spanning.

In hoofdstuk 3, wordt de eerder geïntroduceerde implementatie van recombinatie op het grensvlak gebruikt om het deficit in open-klem spanning in perovskiete zonnecellen met een brede bandkloof te onderzoeken. Zonnecellen met een brede bandkloof zijn benodigd voor perovskiet-silicium tandems, maar lopen achter op reguliere perovskiete zonnecellen, vooral in termen van open-klem spanning. Om het deficit in open-klem spanning te onderzoeken worden een grote hoeveelheid simulaties gedaan om algemene trends in open-klem spanning te vinden. De open-klem spanning blijkt proportioneel te zijn met de dichtheid van ladingsvallen en minderheidsladingsdragers bij het grensvlak aan de kant van het perovskiet. De dichtheid van minderheidsladingsdragers hangt af van het elektrisch veld in het perovskiet, waar een groot elektrische veld dat helpt bij extractie zorgt voor een lage dichtheid van minderheidsladingsdragers. Om dit elektrische veld te maximaliseren is het van belang om de uitlijning van de banden en het verschil van de effectieve toestandsdichtheid samen in beschouwing te nemen. Het elektrische veld hangt namelijk af van de som van de individuele effecten op het elektrostatische potentiaal. Specifiek voor perovskiete zonnecellen met organische transportlagen betekent dit dat de effectieve toestandsdichtheid in de transportlaag substantieel hoger is dan in het perovskiet. Hierdoor is het nodig om in plaats van uitgelijnde banden, een extractie barrière te introduceren om te zorgen dat de ladingsdragersdichtheid in de transportlaag niet te hoog wordt. Dit inzicht stelt makers van zonnecellen in staat om een hoge open-klem spanning te verkrijgen ondanks een grote hoeveelheid defecten op het grensvlak tussen het perovskiet en de transportlaag.

In hoofdstukken 4 en 5 ligt de focus op transportverschijnselen in gedoteerde organische halfgeleiders. Deze materialen worden niet alleen gebruikt als transportlagen voor perovskiete zonnecellen, maar ook in organische thermoelektronica. Organische thermoelektronica worden gebruikt om warmte deels om te zetten in elektrische energie. Voor de hand liggende toepassingen zijn energievoorziening voor draagbare of sensoren in afgelegen gebieden, omdat de energievraag daar typisch bescheiden is en de operationele temperaturen relatief laag. In organische thermoelektronica is een goede geleidbaarheid nodig voor optimale prestaties voor een gegeven materiaal. Daarom wordt vaak dotering gebruikt, omdat dit zowel de ladingsdragersdichtheid als de mobiliteit verhoogd in organische materialen. Het probleem is echter dat bij hoge dotering, de geleidbaarheid niet meer toeneemt, maar afneemt met toenemende dotering.

In hoofdstuk 4 worden experimenten, analytische afschattingen, en kinetische Monte Carlo simulaties gebruikt om dit probleem te onderzoeken. Experimenteel wordt er laten zien dat morfologische verandering als gevolg van hoge dotering zeer waarschijnlijk niet de oorzaak is voor het onderzochte systeem. Analytische resultaten wijzen uit dat elektron-elektron interacties zich manifesteren in een Coulomb pseudo-kloof bij kamertemperatuur in hoog gedoteerde systemen.

In hoofdstuk 5 ligt de focus op de relevante fysica van gedoteerde organische halfgeleiders voor thermoelektronische toepassingen. Gevonden wordt dat de Seebeck coëfficiënt in deze materialen uitsluitend afhankelijk is van de hoeveelheid vrije ladingsdragers, dat wil zeggen, ladingsdragers die niet vast zitten op een tegen ion. Daarnaast worden zowel de Seebeck coefficient als de geleidbaarheid gereduceerd door elektron-elektron interacties bij hoge dotering. Dit betekent dat het reduceren van elektron-elektron interacties een belangrijke strategie kan zijn voor het verkrijgen van een nieuwe generatie organische materialen voor thermoelektronica.

Acknowledgments

Doing research and writing a PhD thesis is hard work. To make this effort rewarding, an interesting topic and nice people to share it with are a prerequisite. I think I have covered the research in more depth than most are likely to read. However, I did not yet thank all the people who had an equal contribution to make this undertaking worthwhile.

First of course, **Jan Anton**. During my study, I was quite confident that I would not end up doing a PhD. After starting the master project in your group, however, I really started to like the work and the atmosphere in the group. From when I started as a master student, to the end of my PhD, your door was always open for discussion. Figuratively, of course because you were not alone in your annoyance with the noise level of the meetings down the hall. It was actually the door of our office that was always open. This, together with the couch, facilitated most informal meetings, where we would discuss important matters. Topics like Linux, boats, and food, but the conversation would typically gravitate towards physics to the end. This all of course while switching naar het Nederlands en back again, depending on who joined or left the conversation. I always really enjoyed these ad-hok discussions that would sometimes result in new projects, new hypotheses, or us both being very confused.

Though a simulation PhD can be a lonely endeavour, it never really felt this way. I have always felt that we were tackling the problems in my projects together, where you were an unrelenting source of motivation and ideas. This was not all of course, in most of my projects there would be at least one of your clever pieces of code playing a part. One of the projects I liked most is the SIMsalabim project, where we would sometimes resort to pair-programming to tackle the most intricate details of the code. These sessions were some of the most tiring and rewarding of my whole project. Thank you for four amazing years in the group.

During my time in the group, I have spent a lot of time in the coffee/lunch room. While you, **Maria**, urged us not do any experiments in the microwave, it did feel like a lab. It was the place where I interacted experimental people who actually knew how to make and measure perovskites, which was always very nice. Otherwise, our interaction was mostly during one of the group socials, where we had to make sure to somehow fit my idea for the group outing in the university budget rules. I have enjoyed our interaction and wish you all the best.

Vincent, though it feels like a long time ago now, you were already in the group when I joined. A lot of my practical knowledge of perovskite solar cell simulations and SIMsalabim came from you. I very much enjoyed the collaboration we had on some of the simulation projects. We also had a lot of fun outside of work during one of the many borrels or games of squash. This really made my time in the group a lot more enjoyable, thanks.

Of course part of what made the group atmosphere nice were the wonderful people that I worked with. **Vincent, Azi, Nutifafa, Jian, Unnati, Xuwen, Tim**, thanks for all the discussions at the whiteboard and being nice colleagues in general.

While our subgroup was relatively small, I got to know some of the people form Maria's group very well. **Bart**, **Artem**, **Herman**, and **Simon**, It has been a pleasure having lunch, coffee or the ocasional beer. I hope we will keep doing this in the future.

While I did not enter the labs, except for the occasional computer cleaning with the nitrogen gun, I was involved more on the IT administration side of things. This is where **Arjen**, **Theo**, and I found the nice division of labour. Any problem on a pc running Linux would be my problem, but any windows related issue would be handled by the technicians. Thanks for this and all the lively discussions of university politics.

One of the nicest aspects of doing a PhD is the combination of research and supervision of student projects. I have had a lot of fun teaching you the basics of numerical simulations and learning from you when you were up to speed, thanks **Miina, Friso**, **Hugo**, and **Vishesh**.

Dan wil ik graag mijn paranimfen bedanken. **Tim**, ik was blij toen je je bij de groep aansloot. Naast dat je een gezellige toevoeging bent, ben je ook een simulatie promovendus. Ik hoop dat Frank Brokken dit niet leest, maar de compiler is ook niet altijd je beste vriend. Het delen van programmeerproblemen maakt het werk een stuk aangenamer.

Camiel, vanaf het begin van onze studie tot het eind van mijn PhD hebben we gesnowboard, dingen gebouwd, gestudeerd, samengewoond, en dingen kapot geanalyseerd. Ik het altijd van de avonturen genoten en hoop dat er nog vele mogen volgen.

Het delen van de voor en tegenslagen van een promotietraject is altijd fijn, zeker met mensen die ook met één been in de stof staan. Nou is het meer dan alleen de stof die we deelden. Zo vlogen de koffiepauzes, maar ook vrijdag-avonden voorbij als wij weer op pad waren. Dat werd gewaardeerd **Matthijs**.

Het werken in bij de photophysics en optoelectronics groep was, zeker in het begin, niet lost te zien van de mensen waar ik in de studie veel mee optrok, **Camiel**, **Bauke**, **Hilbert**, **Rick**, **Wopke**, **Sven**. Bauke en Hilbert, in mijn tijd in de groep waren jullie ook deel van de onderzoeksgroep en hebben met jullie heb ik nog de nodige avonturen beleeft op één van de vele promotie feesten die er voor corona in de groep waren. Dat waren goede tijden in POE, dat we dat we dat in de toekomst nog eens dunnetjes over mogen doen onder het genot van een biertje, of toch maar een bakje thee.

En dan mijn vrienden van de ploeg, **Rick**, **Harm**, **Teun**, **Bram**, **Wouter**, en **Sven**. Een promotie doen is niet altijd gezellig. Met jullie is het wel altijd gezellig. Ik hoop dat er nog vele kerstdiners, wintersporten, en weekenden mogen volgen.

Daarnaast nog de mensen met wie ik rond het begin van mijn promotie een heftige tijd hebben doorgemaakt, **Yannick**, **Wouter**, en **Gijs**. Ik zal de reis naar Lapland en de oliebollen expres niet snel vergeten. Yannick, ik ben haast blij dat ik onze vreselijk interessante gesprekken steeds weer vergeet, want dan kunnen we elke keer weer van voor af aan beginnen.

Anita en **Mark**, het maakt niet zo veel uit in wat voor situatie we ons begeven. Zowel een wintersport, festival, als lockdown is met jullie een feest. Dit heeft me altijd veel energie gegeven en dat zal het in de toekomst ook zeker blijven doen.

Een van de gevaren van hard werken is dat je in een sleur terecht komt. Als er iemand is die dat kan helpen doorbreken, dan ben jij dat **Helma**. Het is altijd weer genieten als er weer een nieuw muziekje gevonden is, of je weer een sterk verhaal rijker bent. Ik kijk uit naar onze volgende sessie.

In je promotietraject moet je je overwinningen vieren. Als er iemand sterk is in het vinden van redenen voor een feestje dan ben jij dat **mam**. Een paper ingestuurd, geaccepteerd, en gepubliceerd zijn drie keer reden om iets te vieren. Ik heb er het volste vertrouwen in dat dit ook in de toekomst zo blijft, ik kijk ernaar uit.

Bij het schrijven van jouw thesis heb ik me vooral bezig gehouden met het in balans brengen van je werk werk en privé. Met name door het zwaarder maken van je privéleven, zoals je zelf al enigszins verdekt opstelde. Jouw invloed op mijn thesis is van hele andere aard. Jaren voordat ik begon waren we al bezig met het afschatten van lengtes van bruggen en moleculen op vakantie. Dit was niet alleen leuk, maar heeft me ook zeker gevormd als fysicus. Thanks voor alles **pa**.

Als laatste natuurlijk mijn lieve vriendin **Nienke**. De laatste vier jaar hebben we alle hoogte- en dieptepunten samen gedeeld. Hierdoor heb ik soms het gevoel dat jij mij beter snapt dan ik zelf doe. Dank voor je onvoorwaardelijke liefde en steun. Zonder jou waren de grote, maar ook zeker de kleine momentjes de laatste jaren niet hetzelfde geweest.